UNIVERSITY OF TRENTO

DOCTORAL THESIS

Mapping the mouse connectome with voxel resolution

Coletta, Ludovico

Advisor: ALESSANDRO GOZZI

A thesis submitted in fulfilment of the requirements

for the degree of Doctor of Philosophy in the:

Doctoral School in Cognitive and Brain Sciences, University of Trento

Center for Neuroscience and Cognitive Systems,

Istituto Italiano di Tecnologia

15 March 2022

Abstract and declaration

Declaration

This dissertation is the result of my own work unless specifically indicated in the text as the outcome of a collaboration, or cited and acknowledged as material from another source. It has not been previously submitted, in part or whole, to any university of institution for any degree, diploma, or other qualification.

Signed: 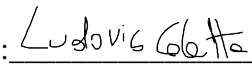

Date: 15.03.2022

Coletta, Ludovico

University of Trento, Doctoral School in Cognitive and Brain Sciences

Istituto Italiano di Tecnologia, Center for Neuroscience and Cognitive Systems

Doctor of Philosophy

Mapping the mouse connectome with voxel resolution

LUDOVICO COLETTA

Fine-grained descriptions of brain connectivity are required to understand how neural information is processed and relayed across spatial scales. Prior investigations of the mouse brain connectome have employed discrete anatomical parcellations, limiting spatial resolution and potentially concealing network attributes critical to connectome organization.

In this work, we provide a voxel-level description of the network and hierarchical structure of the directed mouse connectome, unconstrained by regional partitioning. We found that hub regions and core network components of the voxel-wise mouse connectome exhibit a rich topography encompassing key cortical and subcortical relay regions. We also typified regional substrates based on their directional topology into sink or source regions, and reported a previously unappreciated role of modulatory nuclei as critical effectors of inter-modular and network communicability. Finally, we demonstrated a close spatial correspondence between the mesoscale topography of the mouse connectome and its functional macroscale organization, showing that, like in primates and humans, the mouse cortical connectome is organized along two major topographical axes that can be linked to hierarchical patterns of laminar connectivity, and shape the topography of fMRI dynamic states, respectively.

This investigation was paralleled by further studies aimed to more closely relate structural connectome features to the corresponding large scale functional networks of the mouse brain. We first focused on the mouse default mode network (DMN), describing its axonal substrates with sublaminar precision and cell-type specificity. We found that regions of the mouse DMN are predominantly located within the isocortex and exhibit preferential connectivity. Dedicated tract tracing experiments carried out by the Allen Brain Institute revealed that layer 2/3 DMN neurons projected mostly in the DMN, whereas layer 5 neurons project both in and out. Further analyses revealed the presence of separate in-DMN and out-DMN-projecting cell types with distinct genetic profiles.

Lastly, we carried out a fine-grained comparison of functional topography and dynamic organization of large-scale fMRI networks in wakeful and anesthetized mice, relating the corresponding functional networks to the underlying architecture of structural connectivity. Recapitulating prior observations in conscious primates, we found that the awake mouse brain is subjected to a profound topological reconfiguration such to maximize cross-talk between cortical and subcortical neural systems, departing from the underlying structure of the axonal connectome.

Taken together, these results advance our understanding of the foundational wiring principles of the mammalian connectome, and create opportunities for identifying targets of interventions to modulate brain function and its network structure in a physiologically-accessible species.

Acknowledgements

When I joined the Functional Neuroimaging Lab, I was mentally prepared to go through some hard times, as Rovereto meant leaving my family, friends, and loved ones to enter a new country all by myself. What I was not ready for, however, was to find an extraordinary set of people who in no time became like a second family.

To start, I would like to thank my advisor Alessandro Gozzi. You have been like a father-in-science to me, carving a coding and data freak into an almost mature scientist. I hope that your pirate attitude toward apparently unsolvable problems will stay with me for the rest of my days. Thank you.

To the rest of the past and present lab members: Alberto, Alessia, Adam, Caterina, Neha, Filomena, Elizabeth, Andrew, and Silvia. Thank you for teaching me what team work really means, and for sharing many joyful moments outside the lab.

To my oversight committee, Jorge Jovicich and Stefano Panzeri, thank you for your critical input during this process, every meeting was a chance to grow professionally and scientifically.

To the administrations of IIT and the doctoral school, many thanks for your kind support and patience while dealing with all the weird requests I had. Leah Mercanti, Rosella Polli, Sara Maistrelli, and Paola Battistoni, thank you all, you made my life much easier.

To Ben: thanks for creating such an incredible community. You will be Rovereto's mayor one day, we all know this.

To Marco, Chris, Bastien, Davide Potrich, and Davide Saretta: how could I forget playing basketball in August in the middle of the afternoon?

To Nath: I had the opportunity to attend only one conference during my PhD. Besides the science, I am glad it made me meet you.

To Demetrio and Giulia: you are the best "Rovereto starting kit" one could ever wish.

To David and Alexandria: Your wittiness made the PhD experience something special. Thanks

To Alexia and Christian: thanks for your company and for introducing me to climbing.

To Shahry: you entered my life as the weird-Iranian-guy-sitting-in-front-of-me, ended up being among the closest friends here in Rovereto. Thanks.

To Elena: thanks for your company during the first lock down. You saved me from (definitely) losing my mind.

To Carola, Dani, Lorenzo, and Fede: as one Co-Activation Pattern described by our beloved Dani, we shared the ups and downs of our life. I am glad I belonged to the same cluster.

Special mention to my “brothers-in-wind”, Dani and Fede: I could have never imagined that our “Due Lune” would have brought us so far. Thank you guys.

To mum and dad: your sacrifices allowed me to study for such a long time. I wish I had the proper words to thank you both.

To Cristina: I saw your apartment before actually meeting you, and while leaving, I had the feeling you were the kind of a person one meets once in a lifetime. As time goes by, I am realizing that the intuition was indeed correct. Thanks.

Publications

- Coletta, L., Pagani, M., Whitesell, J.D., Harris, J.A., Bernhardt, B., & Gozzi, A. (2020). Network structure of the mouse brain connectome with voxel resolution. *Science Advances*, *6 (51).*

- Whitesell, J. D., Liska, A., Coletta, L., Hirokawa, K. E., Bohn, P., Williford, A., ... & Harris, J. A. (2021). Regional, Layer, and Cell-Type-Specific Connectivity of the Mouse Default Mode Network. *Neuron*, *109*(3), 545-559.

- Gutierrez-Barragan*, D., Singh, N. A*., Alvino, F., Coletta, L., Rocchi, F., De Guzman, E. A., ... & Gozzi, A. (2022). Unique spatiotemporal fMRI dynamics in the awake mouse brain*, Current Biology.*

- Rocchi, F*., Canella, C.*, Noei, S.*, Gutierrez-Barragan, D., Coletta, L., Galbusera, A., ... & Gozzi, A. (2022). Paradoxical fMRI overconnectivity upon chemogenetic silencing of the prefrontal cortex. *Accepted for publication in Nature Communications*

- Fasoli, D., Coletta, L., Gutierrez-Barragan, D., Gozzi, A., Panzeri, S. (2021). On the fundamental principles that govern the temporal evolution of the functional states in the resting mouse: A connectome-based computational approach. *Manuscript in preparation*

- Neniskyte, U., Vadisiute, A., Coletta, L., Jevdokimenko, K., Dabkeviciene, D., Gozzi, A., ... & Gross, C. (2021). Phosphatidylserine scrambling is required for developmental synaptic pruning. *Under revision in Neuron*.

- Grandjean, J., Canella, C., Anckaerts, C., Ayrancı, G., Bougacha, S., Bienert, T., Buehlmann, D., Coletta, L., ... & Gozzi, A. (2020). Common functional networks in the mouse brain revealed by multi-centre resting-state fMRI analysis. Neuroimage, 205, 116278.

Table of Contents

List of Figures & Tables

Nomenclature and Acronyms

ABA	*Allen Brain Atlas*
ABI	*Allen Brain Institute*
BOLD	*Blood-Oxygen-Level-Dependent*
CAPs	*Co-Activation Patterns*
DMN	*Default Mode Network*
FC	*Functional Connectivity*
ISH	*In situ hybridization*
LCN	*Latero Cortical Network*
LPN	*Latero Posterior Network*
MRI	*Magnetic Resonance Imaging*
dMRI	*Diffusion MRI*
fMRI	*Functional MRI*
rsfMRI	*Resting state fMRI*
PA	*Proximal Attachment*
PFC	*Prefrontal Cortex*
SC	*Structural Connectivity*
SG	*Source Growth*
SGPA	*Source-Growth-Proximal-Attachment*
T1w	*T1-weighted*
T2w	*T2-weighted*

Chapter 1 General Introduction

1.1 Brain Connectomics

The term "connectome" refers to the complete description of the wiring diagram of the brain (Sporns *et al.*, 2005). This word is now largely used to describe datasets or resources providing whole-brain, comprehensive descriptions of the axonal or "structural" (white-matter) connectivity of a given individual or organism (SC, van den Heuvel *et al.*, 2016). Owing to the growing number of connectomes of different species reconstructed in the recent years, a great effort has been put into the search of both species-invariant and species-specific wiring principles, with the hypothesis that cross-species commonalities may be a reliable indicator of evolutionary preserved architectural features of the brain, whereas differences may reflect specific adaptations in cognition and behavior across evolution (van den Heuvel, Bullmore, *et al.*, 2016). Besides the interest in comparative biology, connectome research (i.e. "connectomics") can be instrumental in probing the elusive relationship between brain structure and function (Suárez *et al.*, 2020). While empirical and theoretical work suggests that SC poses strong constraints on the possible repertoire of neuronal configurations detectable with functional brain mapping (Cabral *et al.*, 2017; Khambhati *et al.*, 2018; Suárez *et al.*, 2020), the exact nature of this relationship remains obscure.

Disentangling the exact relationship between functional and structural brain organization has so far proven to be difficult for a number of experimental and conceptual limitations. First and foremost,

most connectomic research to date has been carried out in human, where SC is measured by means of Magnet Resonance Imaging (MRI). This approach, however, only provides a very coarse, large-scale estimate of SC, and does not provide information about the directionality of the connections (van den Heuvel, Bullmore, *et al.*, 2016; Suárez *et al.*, 2020). These issues may lead to largely approximated descriptions (or even misrepresentations of SC in human (Kale *et al.*, 2018), hence limiting the inferences that can be made from these datasets. Moreover, comprehensive descriptions of the specific relationship between brain function and structure can only be obtained via the integrating connectomics investigations across multiple levels of spatial resolution, i.e. from cellular (micro-) to areal level (macroscale) (Khambhati *et al.*, 2018).

While in humans ethical and methodological constraints prevent the systematic analysis of SC beyond the macroscale, both micro- and the meso-scale connectomes are experimentally accessible in model organism such as primates, rodents and the larval zebrafish (Oh *et al.*, 2014; Kunst *et al.*, 2019; Lin *et al.*, 2019). Owing to efforts of the Allen Brain Institute (ABI), structural connectivity of the mouse brain has been mapped at the cellular level via the use of viral tracers, representing one of the best characterized mammalian connectome ever described to date (Oh *et al.*, 2014; Harris *et al.*, 2019; Knox *et al.*, 2019). At the same time, recent advances in functional Magnetic Resonance Imaging (fMRI) have also made it possible to describe macroscale *functional* network organization in a plethora of mammalian organisms, including multiple primate species (Milham *et al.*, 2018), rats and mice (Sforazzini *et al.*, 2014; Gozzi & Schwarz, 2016). The combined use of these brain mapping approaches may help unveil how anatomical structure sculpts the transition from local synaptic circuits to form macroscale functional networks, an area of investigation of critical importance towards the goal of understanding of the principles of brain function and dysfunction.

Recent progress in cross-species fMRI has also shown remarkable correspondences in the macroscale functional organization of rodent and primate brain, supporting the use of rodent species to investigate the foundational wiring principles of the mammalian brain (Lu *et al.*, 2012; Liska *et al.*, 2015; Gozzi & Schwarz, 2016; Bertero *et al.*, 2018; Tsai *et al.*, 2020). Thereby, the combined use of structural and functional connectome mapping in rodents represents a valuable platform where state-of-the-art manipulation techniques and computational models may converge, offering the opportunity to advance our understanding of brain function in health and disease (Gozzi & Schwarz, 2016).

In this introductory chapter I will provide a brief critical overview of the main computational approaches, key findings, open questions (e.g. structure-function mapping), and recent technical advancement in the field of cross-species connectomics. Owing to prevalent use graph theoretical approaches to investigate network properties of the human brain (see for example the Human Connectome Project, Van Essen *et al.*, 2012), in the next section, I will first introduce this analytical framework and some of the most relevant findings in this field of research. I will then briefly introduce the methodological limitations inherent to the analysis of human connectome data, with the purpose of discussing the technical advantages and the biological insights gained with the advent of whole brain non-human connectome research.

1.2 Graph-based properties of human connectomes

A theoretical and analytical approach that has gained a lot of interest in human connectome analysis is grounded in graph theory, a mathematical discipline that deals with the study of graphs, i.e. discrete representations of a finite set of objects (nodes), the interaction between them (edges), and the resulting network arising from the interaction (van den Heuvel & Sporns, 2013). Graph theory

has proved fruitful for connectomics; its abstractness allows to model SC (in this case representing the edges of the network) between synapse, neurons, and whole brain regions (nodes), thus making possible the discovery of invariant network properties across species and scales (van den Heuvel, Bullmore, *et al.*, 2016; Betzel & Bassett, 2017)

Graph theory has been fruitfully used to map central nodes – so called "hubs" – in brain networks (see Figure 1 for basic network attributes). The most intuitive approach for hub definition relies on the characterization of the number of connections per node – a graph metric called "degree" (Rubinov & Sporns, 2010; van den Heuvel & Sporns, 2013). When the degree distribution follows a power law, the network is said to be scale free (or scale invariant, meaning that its structure does not change with its size), and under such circumstances the network contains hubs, i.e. very few nodes with a disproportionally high degree (Rubinov & Sporns, 2010; van den Heuvel & Sporns, 2013). Interestingly, it has been consistently shown that the degree distribution of the human connectome follows a heavy-tailed distribution, and hub-like regions have been mapped in integrative areas of the brain, such as the prefrontal cortex, the insula, and the parietal cortex (van den Heuvel & Sporns, 2013). Of note, the notion of hub does not appear to be purely statistical, as central nodes have been found to have higher metabolic requirements (Bullmore & Sporns, 2012). Moreover, van den Heuvel *et al.*, 2012 showed that hubs are characterized by a high number of connections and tend to be densely interconnected constituting an exclusive "rich club" or "structural core". These authors also showed that rich club connections span long distances and participate in a large proportion of network shortcuts, leading to the hypothesis – under the assumption that the brain relies on the shortest path for communication – that this special set of nodes and connections acts as backbone for global brain communication. It should be noted, however, that the degree metric relies on the use of "binary matrices", which encode only the existence of a given edge, and as such implicitly assuming that all

connections are equally important. This simplification collides with biology, since SC strength and/or density between two synapses/neurons/brain regions may vary across the brain (Oh *et al.*, 2014). For this reason, the computation of its weighted counterpart – node strength – has become increasingly frequent (Rubinov & Sporns, 2010), even though it should be noted that the two measures are not simply analogues of one another. Indeed, it may be possible to find nodes with many weak connections but low total strength (high degree, low strength), and nodes with a single but strong connection (low degree, high strength).

Centrality measures are often complemented by metrics sensitive to the network segregation, such as clustering coefficient and the modularity index, two indices that measure the degree of segregation at the local (i.e. nodal) and global level (Rubinov & Sporns, 2010; van den Heuvel & Sporns, 2019). The former metric measures the tendency of network nodes to form "locally connected triangles", whereas the latter is an indicator of the network propensity to form clusters/communities of densely interconnected nodes. A high modularity value is interpreted as an index of information segregation, a principle that in case of the (human) connectome may be interpreted as a proxy for specialized neural processing and the existence of distinct functional systems (van den Heuvel & Sporns, 2019). Building on the concept of modularity, it is possible to quantify for each node the diversity of its inter-modular connections, a graph metric called "participation coefficient" (Rubinov & Sporns, 2010; Bertolero *et al.*, 2017), and nodes that have a disproportionally high participation coefficient are called "connector hubs" (see Figure 1), with the assumption that they facilitate between-modules communication (Rubinov & Sporns, 2010; van den Heuvel & Sporns, 2013). Recent investigations (Meunier *et al.*, 2010; Betzel *et al.*, 2017) have shown that the human connectome has indeed a prominent modular structure. Importantly, structural modules appeared to be associated with specific functional networks, corroborating the

hypothesis that human connectome supports specialized neural processing via interaction between specialized modular units. Connector hubs play therefore an important integrative role, and are as such embedded in integrative brain regions – overlapping to some extent with high degree hubs – as well as in the somatomotor systems (Gordon *et al.*, 2018; Wang *et al.*, 2018).

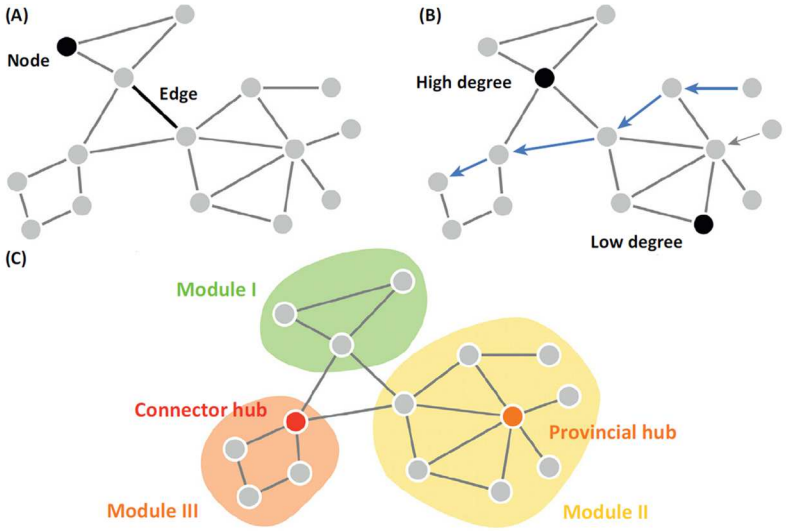

Figure 1. Basic network attributes. (A) Graph theory allows to study the brain as finite set of elements (called nodes, ranging from synapses to whole brain regions), the pairwise interaction between them (called edges, modeling structural connectivity or functional interactions), and the resulting network arising from all the pairwise interactions. (B) Nodes differ with respect to their number of connections (a metric called *degree*); high degree nodes are also called *hubs. (*C) Brain networks tend to segregate into sparsely interconnected functional units called communities/modules; connector hubs link different communities within the network (van den Heuvel & Sporns, 2013).

Besides the obvious interest in analyzing the degree of information segregation in the brain, a significant research effort has been invested in mapping its integration capacity, with the assumption that the brain needs to combine the specialized information coming from distributed systems in a rapid and efficient manner (Rubinov & Sporns, 2010; van den Heuvel & Sporns, 2019). In graph theory terms, the ease of communication relies on the concept of *path*, here intended as the sequence of

nodes and links that must be traversed for two nodes to communicate. In the case of structural networks, paths represent potential routes of information flow (Rubinov & Sporns, 2010; Avena-Koenigsberger *et al.*, 2018). One of the most common used metric of integration is the *characteristic path length*, computed as the mean of all shortest paths in the network, which in combination with the clustering coefficient, it is used to compute the so-called *small word index* (Rubinov & Sporns, 2010; Bassett & Bullmore, 2017). Small world networks are characterized by a high clustering coefficient, i.e. the propensity to form local clusters, and by a small characteristic path length, meaning that the topological distance between any two given nodes is on average low, therefore facilitating communication. It has been consistently shown that the human connectome is a small world network (Rubinov & Sporns, 2010; Bassett & Bullmore, 2017), i.e. a network that combines segregation and integration in the most optimal manner. It should be noted, however, that the concept of small world applied to brain networks has also been accompanied by technical controversy, especially with respect to widespread use of binary connectivity matrices to map relevant network parameters such as characteristic path length (Rubinov & Sporns, 2010; Bassett & Bullmore, 2017; Avena-Koenigsberger *et al.*, 2018). As discussed above for degree-based metrics, binary connectivity matrices encode only the existence of a given edge, implicitly assuming that all connections are equally important. This simplification is indeed problematic, since SC strength and/or density between two synapses/neurons/brain regions may vary across the brain (Oh *et al.*, 2014). Weighted counterparts for the computation of the characteristic path length have been introduced (Bassett & Bullmore, 2017), but these are the object of debate as well, owing to the difficulty of relating connection weights to topological distances (see (Betzel & Bassett, 2018) for a possible solution). The second controversial aspect related to the notion of characteristic path length concerns the biological plausibility of the communication model it assumes. Indeed, in order to

propagate the communication along the most efficient pathway (routing), each node is thought to possess global knowledge about network topology, an assumption that appears to collide with biology (see Avena-Koenigsberger *et al.*, 2018 for a critical discussion and possible alternatives).

An interesting property of small world networks is their optimal resilience against random node/edge deletion, meaning that network topology is not significantly changed after random network attacks (Wang & Chen, 2003). Conversely, these properties make these networks particularly vulnerable to targeted hub removal (Wang & Chen, 2003). This latter characteristics – together with the initial evidence that many psychiatric and neurologic conditions are indeed characterized by structural abnormalities in hub regions (van den Heuvel & Sporns, 2013, 2019) – has fueled research into *pathoconnectomics* (Rubinov & Bullmore, 2013), i.e. the investigation of the contribution of (structural) connectivity defects to human brain pathology and dysfunction (Griffa *et al.*, 2013; de Lange *et al.*, 2019) . This nascent field is now moving beyond the phenomenological characterization of single psychiatric disorders, looking for a theoretical framework to link connectome aberrancies across clinical conditions, and computational approaches able to disentangle their complexity. A notable example of this is given by the recent study from Gollo *et al.*, (2018), who showed that hub nodes located in the prefrontal cortex are the first to break down when the connectome is randomly rewired.

In keeping with this, van den Heuvel & Sporns (2019) proposed a new theoretical framework to study pattern of connectivity across individuals, whereby psychiatric disorders are the result of a sub-optimal design of global topological features. Specifically, in this novel perspective, minimization of wiring costs is one of the main driving forces of connectome organization, resulting in the formation of densely connected communities. According to these authors, a second fundamental wiring principle is global integration, an attribute maintained by the formation of costly – in terms of

metabolism – long-range connections. The search of an equilibrium point between these two non-compatible driving forces is hypothesized to shape resource allocation, and the resulting network topology. Interestingly, the authors linked the multiplicity of possible optimal trade off points to the empirical variability observed in healthy human connectomes. Within this theoretical framework, psychiatric disorders would thus be the consequence of sub-optimal resource allocation, defining a novel connectome landscape in which it is possible to order and link connectome aberrancies across disorders, with the potential of disentangling their complexity.

Most connectomics research to date has been carried out in humans via non-invasive assessments of macroscale SC obtained from diffusion weighted MRI (dMRI), a MRI-based technique sensitive to the orientation of random diffusion of water molecules in the tissues (Maier-Hein *et al.*, 2017; Jeurissen *et al.*, 2019). Based on the observation that myelin hinders the cross-fiber movement of the water, dMRI allows to infer white matter fiber orientation by measuring diffusion along several non-collinear directions, (Maier-Hein *et al.*, 2017; Jeurissen *et al.*, 2019). Fiber tracking algorithms are then used to reconstruct the white matter bundles connecting distant regions of the brain (Maier-Hein *et al.*, 2017; Jeurissen *et al.*, 2019). Although promising in revealing the relationship between structural and functional organization of the human brain and its alterations in brain pathology, a number of key technical shortcomings are associated with dMRI/fiber tracking (Maier-Hein *et al.*, 2017; Jeurissen *et al.*, 2019). First, this approach is only sensitive to the largest white matter tracts, and as such it cannot measure meso- and microscale properties of the brain. Second, due to the theoretical and mathematical assumptions behind the diffusion model, it does not allow to infer the directionality of the connections, thus preventing the discovery of potential connectional asymmetries. This theoretical problem appears to be of non-negligible impact, as it may potentially lead to inaccurate hub estimation (Kale *et al.*, 2018).

To overcome limitations of dMRI-based human SC mapping and better understand the connectional organization of the mammalian brain across scales and species, a large amount of resources has been invested into the mapping of animal connectomes, an approach that permits to sample brain connectivity with much higher spatial resolutions, owing to the use of invasive viral tracers, while full retaining the directional nature of axonal connections (van den Heuvel, Bullmore, *et al.*, 2016; Harris *et al.*, 2019; Kunst *et al.*, 2019; Lin *et al.*, 2019). Not surprisingly, the initial comparison of dMRI-based and "ground truth" mammalian connectomes has corroborated the notion that diffusion tensor imaging provides only a rough estimate of large-scale connectivity. For example, Shen *et al.*, (2019) recently compared several graph theoretical properties of the macaque connectome, revealing that, due to the high number of false positive connections, dMRI leads to inaccurate hub estimation.

Similar to Kale *et al.*, (2018), the authors found the dMRI is however sufficient to detect the coarse core-periphery division of SC networks. In keeping with this, by using tracing data obtained in the mouse, Calabrese *et al.*, (2015) reported that a correspondence between dMRI and neuronal tracing data exists only at the coarsest anatomical level, whereas the two modalities consistently diverge at finer spatial resolution, suggesting a view in which dMRI and neuronal tracing are fundamentally distinct modalities that are sensitive to distinct properties of SC networks. This observation suggests that multiscale investigations of SC in model organisms can optimally complement dMRI-based studies by providing access to levels of inquiry that are currently off limits in human connectome research.

1.3 The mouse brain meso-scale connectome

Weighted and directed SC networks have recently been mapped for several vertebrate and invertebrate species including the macaque, the rat, the pigeon, the cat, the marmoset**,** the Drosphila, the nematode C. Elegans, and the larval zebrafish (van den Heuvel, Bullmore, *et al.*, 2016; Hildebrand *et al.*, 2017; Lin *et al.*, 2019). However, due to its brain whole coverage, single-site acquisition, high-resolution light-microscopy imaging, and voxel resolution, the mouse connectome is considered to represent the gold standard for mammalian organisms so far (Rubinov, 2016).

Owing to efforts of the Allen Brain Institute, the structural connectivity of the mouse brain has been mapped at the cellular level via the use of anterograde viral tracers (Oh *et al.*, 2014), based on 469 viral microinjection experiments performed in the right hemisphere of adult C57BL/6J male mice. For each experiment (see Figure 2 for set of representative injections experiments), 2D images were derived from imaging EGFP-labeled axonal projections at high resolution (0.35 µm) across 140 coronal sections using serial two-photon tomography, automatically segmented to extract the fluorescent signal, and registered to the 3D Allen Mouse Brain Atlas (ABA, isotropic spatial resolution of 100 μm^3). After segmentation and registration, each experiment maps SC from the injection site to the rest of the ca. 500,000 voxels of the mouse brain. Oh *et al.*, (2014) extracted SC strength between 213 regions of the ABA via constrained multivariate regression analysis, obtaining structural connectivity matrices for the ipsi- (i.e. within the right hemisphere) and contra-lateral (i.e. between the right and the left hemisphere) structural connectivity. The use of a constrained multivariate regression procedure resulted in a sparse connectome, where only 6.9% of the ipsi- and 5.4% of the contralateral connections were retained for further analysis. Of note, the definition of SC strength was based on the notion of projection volume, defined as the sum of the segmented pixel counts (and scaled to a mm^3 volume), a read-out that was found to less variable and more stable than

projection fluorescence intensity. According to the authors, each entry of the weighted and directed structural connectivity matrix describes the amount of segmented signal activated in the target region by infecting one voxel in the source region, a SC notion labeled as normalized connectivity strength (NCS). Scaling by the size of the source or target regions offers alternative connectivity strength definitions (Oh *et al.*, 2014).

Oh *et al.*, (2014) reported that the strength of the weights spans a 10^5 - fold range across the brain, with ipsilateral connectivity being significantly stronger than contralateral connectivity. These result underscore the inadequacy of binary network measures in capturing the most salient architectural features of the brain, and are consistent with the hypothesis that long range connections (e.g. contralateral connections) are costly, and as such, relatively scarce. Importantly, the topological analysis performed by the authors revealed that the mouse brain presents network features compatible with scale-free and small-world architectures. In keeping with this, hierarchical clustering performed on patterns of cortico-thalamic connectivity revealed the presence of six distinct clusters: visual, auditory, somatosensory, motor, limbic, and prefrontal.

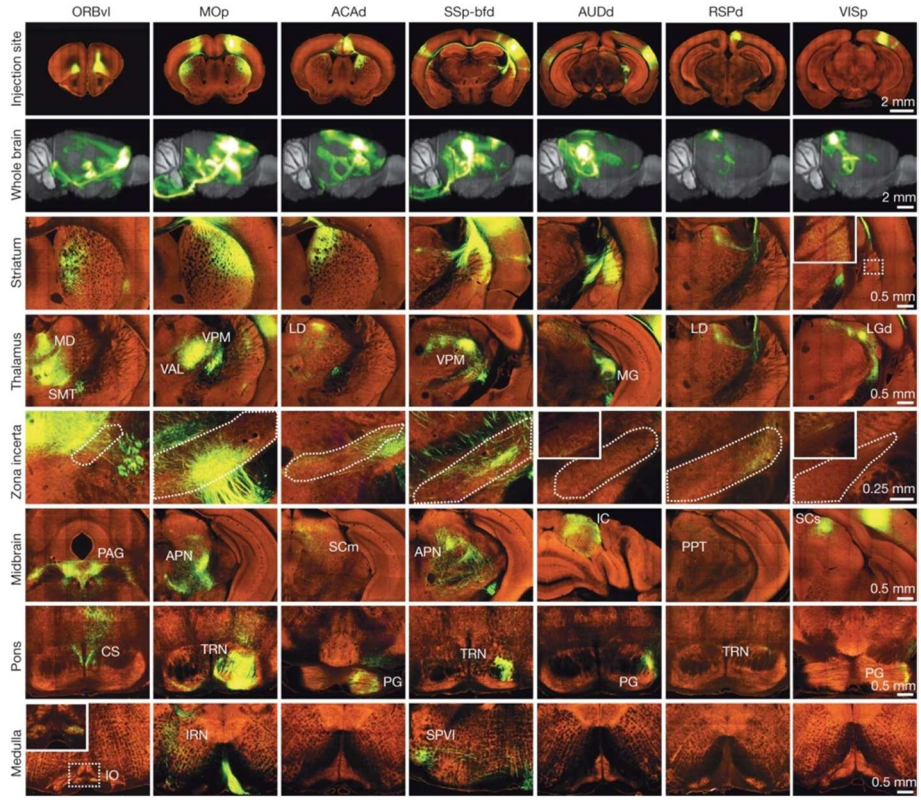

Figure 2. Representative injection experiments of the mouse brain connectome. Whole brain (second row, sagittal view) and structure specific (row 3 to 8, coronal view) projection patterns for seven representative injection experiments across the mouse isocortex (top row, coronal view, Oh *et al.*, 2014).

Recently, the mouse connectome described by Oh *et al.*, (2014) has been recomputed to produce a SC map with voxel-resolution (Knox *et al.*, 2019) . Specifically, under the assumption that SC varies smoothly across the major ABA anatomical divisions – also called parental structures, such as olfactory areas, isocortex, cortical subplate, hippocampal formation, striatum, pallidum, hypothalamus, pons, midbrain, medulla, cerebellum, and thalamus – Knox and colleagues modeled the connectivity of each voxel as the weighted average of the projections patterns of nearby injections. The authors showed that a regional model built from the voxel scale model outperforms the multivariate regression previously employed by Oh *et al.*, (2014) in predicting held-out experiments. At the same time, further work from the ABI employed new and de-novo acquired

dataset to obtain a layer specific description of the mouse brain connectome encompassing more than 1,000 injections experiments and 13 genetically modified animal lines selectively targeting distinct layer-specific projection neuron classes (Harris *et al.*, 2019). Besides elucidating the differential contribution of each cortical layer to the overall intracortical connectivity patterns, this work provides the first description of the hierarchical relationships between cortical areas in the mouse brain, showing that prefrontal and somatomotor brain regions rank at the top and the bottom of hierarchy, respectively. However, at the global cortical level the authors did not find a pronounced hierarchical organization, suggesting a more complex organization of the intracortical connections than previously thought.

1.4 Network properties of the mouse connectome

Recent work has provided a first in-depth characterization of the graph theoretical properties of the mouse connectome (Rubinov *et al.*, 2015). Using a novel parcellation scheme, Rubinov *et al.*, (2015) demonstrated a small world organization of the mouse brain connectome. A hierarchical modular decomposition led to the identification of four different communities, encompassing a somatosensory-motor, a brainstem-cerebellar, an auditory-visual module and an olfactory-hypothalamic-hippocampal module, respectively. Interestingly, eight nodes located in the prefrontal cortex, striatum, thalamus, and midbrain were found to have a significantly higher participation coefficient compared to rest of the network, and as such could not be reliably assigned to any of the four modules. Moreover, the core-periphery bipartition of the connectome revealed the presence of seven high strength nodes, all localized in the auditory-visual module. Owing to a custom fiber tracking algorithm, the authors were also able to reconstruct white matter tracts, to estimate the wiring costs of the axonal projections – defined as the product of axonal length and axonal bandwidth

– and to compute a measure of distance that could incorporate the curvature of the brain. The mouse connectome showed significantly lower wiring costs than a randomly rewired network but higher wiring costs than a spatial lattice (i.e. a network with a regular geometrical structure, also called grid graph, mimicking a wiring cost minimized network) with a matched number of nodes and edges. The authors also reported that the relationship between SC weights and distance was best fit by a power law distribution, and the participation coefficient was found to positively correlate with both wiring costs and the weight-distance power law exponents, meaning that nodes with a high participation coefficient are characterized by high wiring costs and their connections weights decayed slower as a function of distance. This latter aspect is of relevance: the authors were indeed able to simulate all the above-mentioned connectome features only when nodes with a high participation coefficient were also allowed to span longer distances. A model that exclusively sought for global wiring costs minimization could only reproduce the community structure of the network, suggesting the segregation – but not integration – in the mouse brain may be driven by the pressure in cost minimization.

Two other studies tried to uncover the mechanisms underlying the wiring of the mouse connectome by using network simulations. Henriksen *et al.*, (2016) proposed a generative model where a node generates a new connection with a probability proportional to the number of its outgoing connections (source growth, SG), whereas the target node is chosen with a probability that decreases as to the distance between source and target increases (proximal attachment, PA). The authors showed that a network grown with this model – termed "Source-Growth-Proximal-Attachment" (SGPA) – can closely approximate the empirical distribution of both outgoing and incoming connections and the joint clustering coefficient degree distribution in the mouse connectome, outperforming a model where target selection was based on in-degree, and source

selection was based on spatial proximity. Of note, the SGPA model outperformed random, scale-free, and small world networks with matched number of nodes and connection density in modeling the joint clustering coefficient degree distribution, thus highlighting the uniqueness and special character of mammalian brain networks (Figure 3).

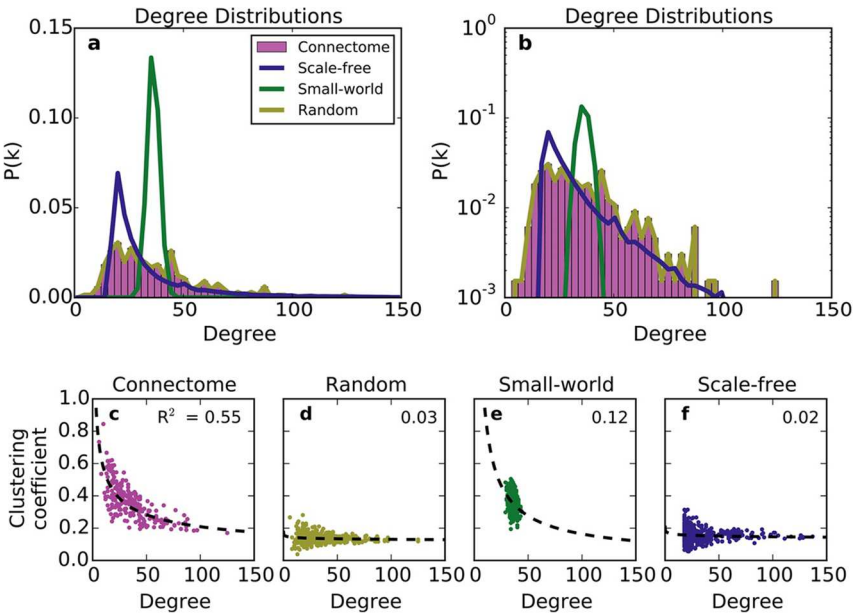

Figure 3. Canonical network models do not adequately capture the uniqueness of the mouse connectome. Standard graphs models provide a moderate fit when modeling both the degree distribution (a-b) and the joint clustering coefficient-degree distribution of the mouse connectome, highlighting unique network properties of the mouse brain (c-f, Henriksen *et al.*, 2016).

Henriksen *et al.*, (2016) proposed that the SGPA model could be a mechanism rooted in brain development and driven by the action of neurotrophins, a family of proteins that promotes the survival of innervating neurons and promotes the growth and branching of their axons. The scarcity of neurotrophins is supposed to cause competitive interactions between growing neuronal populations, with the available amount of proteins preferentially allocated to populations that are maintaining important functional – and hence potentially more connected – pathways. Rubinov (2016) tried instead to disentangle the intricate relationship existing between hubs, rich-club, and

the hierarchical modular organization of the mouse connectome, under the hypothesis that hierarchies and rich club are the byproducts (spandrels) of hubs and modules (basic hallmarks). Of note, the author did not use a generative model, i.e. he did not start with an empty network whose edges were drawn according to a priori specified rule, but he rather sampled from a set of networks that were constrained to possess some specific features, and were otherwise totally randomized. Notably, his result showed that the presence of strength hubs and a pronounced modular structure result in a network characterized by the presence of a rich club and module hierarchies. As in Rubinov *et al.*, (2015), wiring cost minimization alone was found to be insufficient in reproducing the empirically observed connectome architecture.

More recently, Fulcher & Fornito (2016) combined network and transcriptome analyses with the aim of identifying a genetic signature of the rich-club. The authors found that rich-club nodes exhibit a higher transcriptional coupling than the rest of the network, implying that hub nodes are characterized by higher genetic similarity than non-hub nodes. Interestingly, transcriptional coupling in the rich-club connectome of the mouse brain was found to be driven by genes regulating oxidative metabolism, contrasting with the more general association between SC and genes involved in the regulation of neuronal and synaptic pathways. This result is in line with human studies, where high central nodes have been found to have higher metabolic requirements (Bullmore & Sporns, 2012).

1.5 Comparative connectomics

The availability of connectomes in multiple species characterized by increasing degree of complexity has made it possible to probe a number of long-standing questions related to the evolutionary organization of SC across species. Specifically, comparative connectomics (i.e. the comparison of connectional features across species) has enabled the identification of species

invariant wiring principles that describe the architectural organization of the brain. For instance, the mouse connectome is characterized by an optimal trade-off between integration and segregation, it has a rich-club consisting of hub nodes whose connections are particularly strong and span long distances, and it is characterized by a prominent hierarchical organization. A similar set of general network properties have been also been observed in the rat, the macaque, the human as well as in invertebrate connectomes (van den Heuvel, Bullmore, *et al.*, 2016).

More recently, the focus of comparative connectomics, has shifted towards the comparison of specific network attributes across species. For example, Betzel & Bassett (2018) questioned the role of long-range connections as topological shortcuts that allow information integration in a rapid and efficient manner, and showed that in the drosophila, mouse, macaque, and human brain, long range connections provide little contribution to weighted shortest path. Moreover, removing short-range connections had a much greater impact on small-world related statistics than removing long range connections, suggesting that the efficient exchange of information across areas may be guaranteed by short-range connection. Within this framework, long-range connections would therefore enhance the dissimilarity in the connectivity profiles between brain areas. Notably, the authors also showed that for a given brain region, long-range connections tend to connect to other brain regions with a similar connectivity profile (a sign of degeneracy), thus potentially ensuring similar input/outputs in the case of damages to this special set of connections. In a subsequent study, the same authors probed the degree of segregation – *assortative mixing* in graph theoretical terms – of connectome communities in the drosophila, mouse, macaque, and human brain, questioning the consolidated view according to which the brain is composed of well segregated domains with minimized cross-talk (Betzel *et al.*, 2018). According to the authors, this classification should be attributed to the special class of algorithms traditionally used for recovering the community structure of connectomes, which

seeks and forces an assortative network structure but cannot account for other type of interactions. By using a recently developed family of algorithms, the authors showed that communities are indeed assortative, but less than previously reported, revealing a between-community core-periphery structure (not to be confounded with the core periphery structure at the nodal level). These results suggest than communities are less segregated and more integrated than previously thought, a result that was consistently replicated across all the species tested.

Even though species invariant topological features have been repeatedly reported, it should be mentioned that important differences in the overall structural brain organization do exist across different species. For example, in small mammals such as the mouse, 11% of the total brain volume is represented by white matter, a proportion that increases up to 27% in the macaque and to 41% in human (van den Heuvel, Bullmore, *et al.*, 2016). This non-linear relationship between brain and body size has been described via allometric scaling, and is thought to subtend topological differences across species, which in turn may reflect specific adaptations in cognition and behavior across species (van den Heuvel, Bullmore, *et al.*, 2016).

A recent study by Goulas *et al.*, (2019) tried to incorporate such macro-anatomical features into network analyses of brain connectomes across species . The authors compared physical, cytological, and graph theoretical dimensions of brain architecture in the mouse, the cat, marmoset, and macaque monkeys, with the aim to extrapolate a general blueprint of mammalian cortical connectomes. With the exception of the marmoset monkey, the authors found that connections tend to span short distances and link brain regions with a similar cytoarchitectonic structure. Moreover, the same study reported notable species-specific differences in the organization of core-periphery topology, with the core of the cat and the macaque monkey exhibiting a lower neuronal density and a reduced degree of cytoarchitectonic differentiation than the mouse and marmoset monkey,

suggesting an evolutionary displacement of network core in mammals. In summary, while graph theory alone revealed the existence of species invariant network properties, the inclusion of complementary data analysis techniques may shed light into species-specific organizational principles. Additional species-specific wiring features appear to present in the organization of functional circuits. For instance, a comparison of bonobos, chimpanzees, and human connectomes showed an evolutionary gradient of complexity in the anatomical organization of the arcuate fasciculus, a large white fronto-temporal matter tract involved in development of language and speech processing (van den Heuvel, Bullmore, *et al.*, 2016).

1.6 Linking structural and functional connectivity

The availability of high precision connectomes has also made it possible to relate structural features to large-scale functional network organization as assessed with multiple neuroimaging methods. By using task-free resting state functional MRI (rsfMRI), a non-invasive neuroimaging methods that exploits the blood oxygen level dependent (BOLD) signal as an indirect measure of neural activity, it is now possible to define an index of synchronization between fluctuating signals across brain regions which is commonly used as proxy for functional connectivity (FC, Raichle *et al.*, (2001) but see Mohanty *et al.*, (2020) for a critical discussion and alternatives to the use of correlation for FC definition). rsfMRI-based FC studies have reliably shown that the bran is organized in synchronous network that recapitulate functional systems of the brain engaged in task-based activity (Smith *et al.*, 2009). In humans, numerous investigations have attempted to disentangle the relationship between SC as measured with dMRI and FC (Figure 4), both from a graph-theoretical and bio-physical modeling perspectives, reporting weak to moderate overlap between FC and SC

(Abdelnour *et al.*, 2014; Goni *et al.*, 2014; Mišić *et al.*, 2015; Cabral *et al.*, 2017; Lim *et al.*, 2019; Suárez *et al.*, 2020).

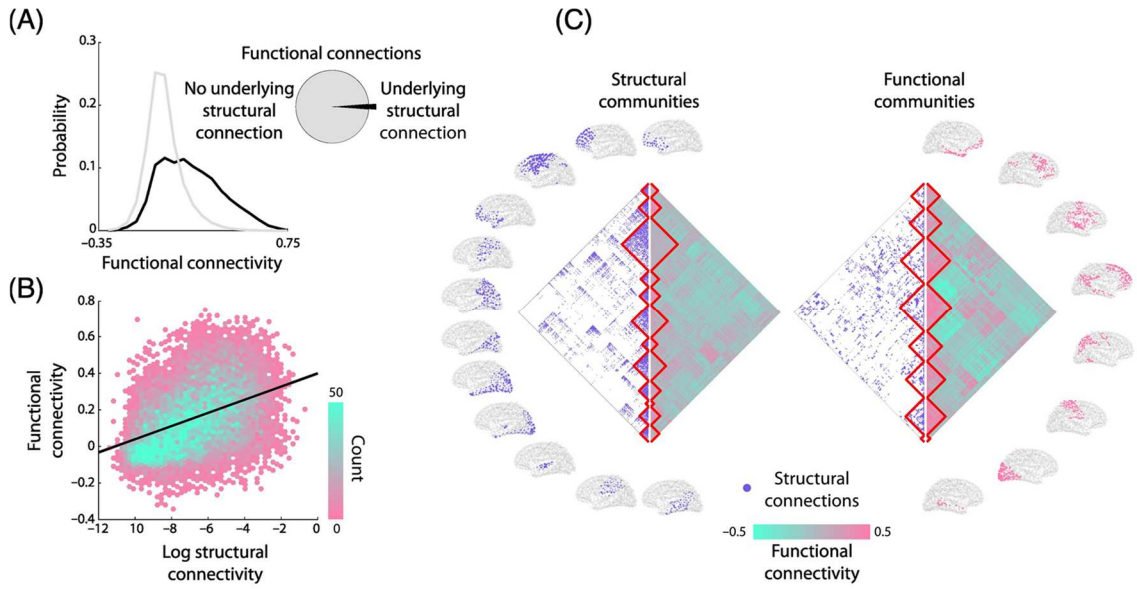

Figure 4. Structural connectivity does not fully recapitulate functional connectivity. In humans, the vast majority of the functional connections represent higher order interactions and as such are not supported by direct structural connectivity (A). Even in the presence of an underlying structural connection, the overall correlation between structural and functional connectivity remains moderate, both at the local level and when comparing the spatial topography of modules/community (B-C, Suárez *et al.*, 2020).

Non-human connectomes, together with advent of rsfMRI in animals, have made it possible to probe how mesoscale SC relate to macroscale FC expanding the comparison of these phenomena across levels of inquiry (Gozzi & Schwarz, 2016). A study by Díaz-Parra *et al.*, (2017) found high correspondence between SC obtained with viral tracing and rsfMRI in rats, as well as high correspondence between empirical and modeled FC, suggesting that the structural connectome may indeed shape the functional architecture of the brain. In keeping with these findings, Grayson *et al.*, (2016) were able to predict the widespread functional disruptions caused by the pharmacogenetic inactivation of the amygdala from the virtual deletion of the corresponding white matter tracts in the

structural connectome of rhesus macaque monkey, suggesting a causal role of SC in generating FC. Of note, the relationship between SC and FC was best predicted by communicability, a graph-theoretical metric sensitive to polysynaptic connections, being the weighted sum of direct and indirect SC (Benzi & Klymko, 2013; Avena-Koenigsberger *et al.*, 2018). These results suggest that monosynaptic connectivity may not be able to fully and reliably account for FC. In keeping with this, chemogenetic inhibition of mouse medial prefrontal cortex has been recently shown to produce increased fMRI connectivity between the silenced areas and its structurally connected cortical and subcortical targets, an effect that driven by increased entrainment of hyperconnected areas with underlying slow brain rhythms (Rocchi *et al.*, 2022, in press). This result provides causal evidence that cortical inactivation does not necessarily lead to reduced inter-areal coupling, but can counterintuitively increase fMRI connectivity via enhanced, less-localized slow oscillatory processes. According to this model, SC critically constrains FC under resting conditions, but structural connections serve as poor predictors of functional interactions in the cognitively active brain, or when brain activity is perturbed by pathological or neuromodulatory input.

Stafford *et al.*, (2014) provided the first description of the relationship between FC and SC in the mouse brain. The authors reported a moderate whole brain FC-SC correspondence, but the authors found a strong overlap between SC and FC for a specific functional circuit supposed to represent the mouse homologue of the human default mode network (DMN, see also (Sforazzini *et al.*, 2014)). The DMN comprises a set of brain regions that were shown to decrease their activity during externally induced task. These regions have been found to be functionally connected, and DMN aberrancies seems to be ubiquitous across psychiatric and neurological conditions (Buckner & DiNicola, 2019; van den Heuvel & Sporns, 2019). Anatomically, the human DMN encompasses a midline component, centered on the anterior cingulate cortex and precuneus, and lateral component that includes the

parietal cortices (Buckner & DiNicola, 2019). The rodent DMN has a similar spatial configuration, and with the exception of the precuneus that has no clear anatomical correlate in mice, it encompasses evolutionarily similar brain areas (Sforazzini *et al.*, 2014; Vogt & Paxinos, 2014; Whitesell *et al.*, 2021). By replicating and extending the results of Sforazzini *et al.*, (2014), the study of Stafford *et al.*, (2014) has important translational implications, as it shows that the one the most studied neural circuits in humans may be present in rodent.

Grandjean *et al.*, (2017) recently provided a comprehensive comparison of FC and SC in the mouse. In first set of analyses, the authors compared viral injections experiments with volume matched seed-based mapping of rsfMRI connectivity. By using this method, the authors found that SC-FC concordance was highest in the isocortex, followed by the hippocampal formation. By contrast, experiments performed in subcortical structures exhibited weak correlations with FC. The authors then specifically probed the FC-SC correspondence for cortico-cortico, cortico-striatal, and cortico-thalamic circuits using SC obtained from the work from Oh *et al.*, (2014). The results of these analyses showed a strong degree of similarity between FC and SC for cortico-cortico and cortico-striatal circuits, but low correspondence in cortico-thalamic connections. Lastly, the authors compared FC and SC in terms of path lengths (number of edges between nodes, a graph-theoretical measure of distance), trying to disentangle the contribution to mono- and polysynaptic connections to FC. The results highlighted how the majority of intra- and interhemispheric functional cortico-cortico circuitry seems to be driven by monosynaptic structural connections, whereas homotopic functional connectivity of subcortical structures was more frequently associated with polysynaptic SC, with the isocortex acting as a possible relay-station.

Recent analyses have also explored whether and how the connectome supports rsfMRI brain dynamics. By investigating the relationship between the mouse connectome and time-series

properties extracted from the rsfMRI BOLD signal, Sethi *et al.*, (2017) reported a positive association between the strength of the incoming projections and the autocorrelation of the BOLD signal, suggesting that brain regions characterized by strong incoming connectivity tend to display longer timescales of activity fluctuations. Again using the mouse connectome, Choi & Mihalas, (2019) took a simulation approach to dissect how specific spatial patterns of structural connections may potentially shape brain dynamics. The authors replicated prior evidence for a power law distribution of connections weights as a function of distance, with spatially close brain regions more strongly connected than distal regions. They next focused on the connections that were stronger than predicted by the power-law relationship, reporting that these connections spanned multiple spatial scales of the network, were localized in deep subcortical regions and the hippocampus, and were shown to promote rapid transitions between local and global synchronization, revealing a specific subset of brain regions that allow to switch between brain states depending on the context. Together, these results suggest that mesoscale topological properties of the structural connectome affect both the "statistic" functional structure of the brain at macroscale level and may shape brain dynamics in a very specific manner.

1.7 Principal axis of connectome organization: diffusion embedding & connectivity gradients

A number of advanced connectomic analyses techniques have been proposed over the last few years to expand the methodological repertoire provided by graph theory and advance our understanding of the structural (and functional) organization of the mammalian brain. One of such advancements of great potential entails a decomposition of whole-brain connectivity data into a sparse set of hierarchically – on the basis on variance explained – components via diffusion

embedding, commonly labeled as gradients (Margulies *et al.*, 2016). From a methodological standpoint, diffusion embedding consists in deriving from SC (and/or FC) a metric of spatial affinity, which encodes – for each brain regions or voxel under analysis – the similarity of the connectivity profiles over space. Instead of delineating discrete network parcellations, the network is than decomposed into regions characterized by gradients of higher (or lower) similarity reflecting the similarity in the spatial arrangement of cortical connectivity. The advantages of this method are twofold (Margulies *et al.*, 2016). First, it does not require a discrete brain parcellation, and as such it potentially allows to discover large scale networks without a priori spatial constrains. Second, it allows to study large scale networks in a continuous space, hence reflecting a more fine-graded view of brain organization. Margulies *et al.*, (2016) first applied diffusion embedding to human rsfMRI data, showing a principal gradient that was anchored on one end in the DMN, and on its other extreme in unimodal primary sensory regions, and a second gradient exhibiting an axis of differentiation between primary sensory cortices (Figure 5). The authors also showed that local peaks in the gradient expression within the DMN were maximally distant from the unimodal sensory regions, thus suggesting that the functional decoupling between transmodal and unimodal brain regions is reflected in the geometrical organization of spontaneous brain activity. Lastly, the authors also found a similar gradient of connectivity in the macaque structural connectome, suggesting that the functional decoupling between trans- and unimodal brain regions may be anchored in the structural organization of the brain and be already present in lower primate species. Intriguingly, this fundamental axis of organization is not limited to the spatial arrangement of cortical connectivity, but it has also been showed to reflect the spatial variation of several biological properties, ranging from neuron density to synaptic excitation, and it is thought to reflect the hierarchical integration

across distinct modalities (Mesulam, 1998; Margulies *et al.*, 2016; Hilgetag & Goulas, 2020; Wang, 2020).

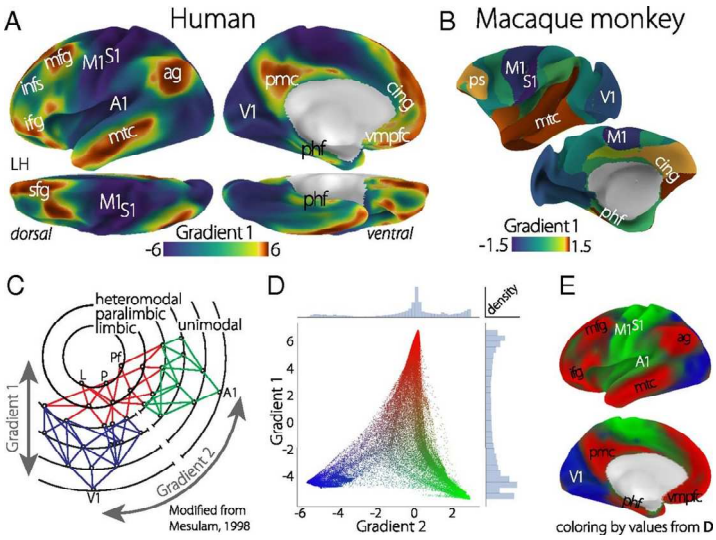

Figure 5. The organization of cortical connectivity can be described by smooth spatial transitions. In both humans (A) and macaque monkey (B), the principal gradient describing the spatial arrangement of cortical connectivity is anchored at the one end in associative brain regions, and at the other end in primary sensory cortices, in line with previous models postulating a hierarchy of increasing functional integration propagating from the unimodal end to transmodal regions (C). The first gradient is accompanied by a differentiation within the primary sensory cortices, separating the somatomotor and auditory cortex from the visual cortex (D-E, Margulies *et al.*, 2016).

Importantly, it has been recently shown that diffusion embedding can capture imbalances in network hierarchy in autism, it can be used to probe gradients of connectivity variations during development and it can reveal new insights into the FC-SC relationship (Hong *et al.*, 2019; Larivière *et al.*, 2019; Vázquez-Rodríguez *et al.*, 2019; Benkarim, Paquola, Park, Hong, *et al.*, 2021; Benkarim, Paquola, Park, Royer, *et al.*, 2021). Mimicking the first principal axis of connectivity variation, it has been shown that the correspondence between FC and SC is high in primary sensory cortices, while FC gradually diverges from SC in polymodal brain regions (Vázquez-Rodríguez *et al.*, 2019; Benkarim, Paquola, Park, Royer, *et al.*, 2021). Furthermore, a new family of bio-physical models in which local

parameters were let free to vary across brain regions revealed the existence of a hierarchical cortical gradient, a feature that significantly increased the fitting between simulated and empirical FC (Wang *et al.*, 2019).

An extension of this approach to cross-species mapping has been recently provided by Fulcher *et al.*, (2019), who provided the first evidence for the existence of human-alike hierarchical gradients in the mouse brain. The authors mapped cortical gradients in the mouse by using the ratio of T1-weighted to T2-weighted images (T1w:T2w), a MRI measurement that is commonly interpreted as a marker of grey matter myelin content and recently used by Burt *et al.*, (2018) in both humans and macaque monkey to replicate and extend the results of Margulies *et al.*, (2016). Using this approach, the authors showed that a decreasing T1w:T2w ratio along an antero-posterior gradient in the mouse brain, reminiscent of the trans- to unimodal gradient reported by Margulies *et al.*, (2016) using rsfMRI, and by Burt *et al.*, (2018) using T1w:T2w ratio. The antero-posterior gradient was found to be predictive for a range of microstructural properties of the mouse brain, including cytoarchitecture, gene expression, interneuron density, and structural connectivity. Collectively, these investigations show how the use of dimensionality reduction techniques can enhance our understanding of the fundamental organizational principles of the brain, and help relate these to underlying architectural and biological properties of developmental or translational relevance.

1.8 General perspective and open questions

Owing to the growing number of high-quality connectomes of different species reconstructed in the recent years, the field of connectomics has gained considerable momentum. Two main research streams within this field are focused on mapping species specific and species invariant features of brain organization, as well as finding a mapping between structure and function. In both cases, graph

theory has proven fruitful, revealing the presence of hubs, clusters/communities, and a small world structure across species, scales, and different imaging modalities.

However, while these approaches have advanced our understanding the organizational principles of the brain, a few outstanding technical and interpretational limitations remain to be addressed, preventing a steadfast interpretation of the results obtain in human and animal connectome mapping. For one, to reduce the computational complexity, network metrics are typically extracted and computed within given brain parcellations. However, macroscopic parcellations limit spatial resolution by definition, imposing sharp, arbitrary boundaries in a system that is continuous, thus potentially leading to inaccurate localization of network features. Moreover, the weakest connections – supposed to represent spurious connectivity – are typically removed using arbitrarily defined thresholds. Both these steps need to be accurately controlled for and motivated, as they can remarkably affect network properties (Garrison *et al.*, 2015; van den Heuvel *et al.*, 2017; Hallquist & Hillary, 2018). The use of parcellation-free topological analyses represents an interesting extension in the field of connectomics. An example of this approach has been recently shown in functional imaging of the mouse brain, in which hub-like properties have been mapped with voxel resolution using rsfMRI (Liska *et al.*, 2015). However, no such analyses have been reported for the mouse structural connectome.

Another set of issues related to current brain network analyses concerns the choice of network metrics to extract, as it is not always possible to translate network properties into meaningful brain features. For example, the biological plausibility of communication processes unfolding on the network shortest paths has been questioned, because it implicitly assumes that each nodes has global knowledge about network topology (see (Avena-Koenigsberger *et al.*, 2018) for a critical overview and possible alternatives). It should also be noted that some algorithms are intrinsically

limited with regards to the network feature that they can extract. As shown by Betzel *et al.*, (2018), community detection algorithms based on modularity maximization can recover only assortative and non-overlapping communities, but the brain –in both health and disease – may significantly deviate from this organizational scheme.

Specifically to the mouse connectome, great effort has been put in trying to elucidate plausible bio-physical and universal wiring mechanisms, but more relevant biological questions have been neglected. For example, a precise characterization of both degree/strength and connector hubs accounting for the directionality of the mouse connectome, and trascending regional parcellation is lacking. The issue of biological plausibility and interpretability applies also to advanced computational modeling and diffusion embedding (Cabral *et al.*, 2017; Huntenburg *et al.*, 2018).

Overall, it is becoming more and more apparent the many network models of SC and brain structure and their related computational assumptions lack empirical probing using causal or experimental manipulations aimed to test their validity. Toward an empirical validation of the assumptions underlying modern connectomics analyses, and the relationship between SC and FC, the implementation of connectomics in physiologically accessible model organisms such as the mouse represents a key milestone that is posed to advance our understanding of these phenomena across multiple scales.

1.9 Aim of this research and structure of my thesis

My research has been prompted by the observation that most connectome research in the mouse has been carried out using an anatomically parcellated version of the mouse mesoscale brain connectome originally described by Oh *et al.*, (2014). My hypothesis was that the use of predefined anatomical might have biased prior network analyses of the mouse connectome, possibly concealing

important network properties critical to the network organization of the mammalian brain. Leveraging a recently released voxel-wise connectome model of the mouse brain (Knox *et al.*, 2019), I thereby undertook a series of network analyses aimed to provide a voxel-level description of the network and hierarchical structure of the directed mouse connectome, unconstrained by regional partitioning. As part of these investigations, I provide a spatially unbiased mapping of a number of key network attribute of the mouse connectome as inferred from graph analyses and gradient mapping, and related them to the corresponding macroscale functional organization of the mouse brain as assessed with rsfMRI. I describe the results of this investigation in Chapter 2. As predicted, these investigations revealed a number of previously unappreciated organizational principles in the mammalian brain, including a directional segregation of hub regions into neural sink and sources, and a strategic wiring of neuromodulatory nuclei as connector hubs and critical orchestrators of network communication. We also found that the mouse cortical connectome is hierarchically organized along two superimposed cortical gradients reflecting unimodal-transmodal functional processing and a modality-specific sensorimotor axis, recapitulating a phylogenetically conserved feature of higher mammals.

The observed spatial correspondence between structural and functional modules, as well as between structural and functional gradients, prompted me to next focus on the investigation of structure-function relationship in the mouse brain. Chapter 3 briefly summarizes some of the results of two collaborative studies in which we compared the mouse functional and structural connectomes across different levels of brain organization, and brain states, respectively. I would like to point out here that Chapter 3 only provides a high-level, and limited summary of these otherwise much larger studies, which I have decided to omit from my thesis to keep this document compact.

In the first of these investigations, I took part in a fine-grained characterization of the structural basis of an evolutionarily important FC network of the mouse brain, i.e. the default mode network (DMN). In collaboration with the Allen Brain Institute, we described the axonal substrates of this network with sublaminar precision and cell-type specificity. We found that regions of the mouse DMN are predominantly located within the isocortex and exhibit preferential connectivity, and that layer 2/3 DMN neurons projected mostly in the DMN, whereas layer 5 neurons project both in and out. Further analyses revealed the presence of separate in-DMN and out-DMN-projecting cell types with distinct genetic profiles.

In a second study I compared network structure of functional and axonal connectome in awake and anaesthetized mice. This research showed that, like previously observed in in conscious primates, functional networks in the awake mouse brain undergo a profound topological reconfiguration such to maximize cross-talk between cortical and subcortical neural systems, departing from the underlying structure of the axonal connectome. By contrast, under anesthesia, the spatial correspondence between structural and functional networks is robust and prominent. Finally, in chapter 4 I briefly summarize the findings of this thesis and discuss some of limitations of my work, as well as a number of future directions.

During my PhD, the voxel-wise connectome model I have developed has been used in a number of additional collaborative studies that are however not reported here. A full list of the published or submitted papers I have contributed to is reported at the beginning of this document (Page viii).

Chapter 2 Network structure of the mouse brain connectome with voxel resolution

This chapter has been published as: Coletta, L., Pagani, M., Whitesell, J. D., Harris, J. A., Bernhardt, B., & Gozzi, A. (2020). Network structure of the mouse brain connectome with voxel resolution. *Science Advances*, *6*(51), eabb7187. DOI: 10.1126/sciadv.abb7187

2.1 Introduction

Studies examining the structural architecture of the brain have advanced our knowledge of how information is processed and integrated across distributed and specialized neural circuits. Current network theory applied to brain connectomes has greatly contributed to this process, highlighting a series of common organizational principles underlying brain connectivity, many of which appear to be species and scale invariant (van den Heuvel & Sporns, 2019). These include the presence of discrete regional sub-systems (termed *communities*) critically interlinked by a small number of highly-connected *hub* nodes, a configuration optimally suited for effective information processing and integration of neural signals across sensory and cognitive domains (van den Heuvel & Sporns, 2013). Brain communities and hub regions have been observed at different investigational scales and using multiple connectivity readouts in several species, from the nematode *C. Elegans* to humans (Towlson *et al.*, 2013; Rubinov *et al.*, 2015; Wang *et al.*, 2018).

Recently, the mesoscale connectome of the mouse brain has been mapped via the use of directional viral tracers, representing one of the best characterized directed mammalian connectome ever described to date (Oh *et al.*, 2014; Rubinov, 2016; Harris *et al.*, 2019). The integration of this

dataset with gene expression maps and layer-specific viral tracing have advanced our understanding of the wiring principles of the mammalian brain, revealing a network core of highly interconnected and metabolically costly hub nodes (Fulcher & Fornito, 2016), and a phylogenetically conserved feedforward-feedback laminar hierarchy in intracortical structure (Harris *et al.*, 2019). However, most investigations of the mouse connectome to date have been limited by the use of pre-defined anatomical parcellations in which connectional parameters, from which network attributes are computed, are quantified under the assumption of regional homogeneity (Oh *et al.*, 2014). This has typically entailed the interrogation of subsets of anatomically aggregated meta-regions (for example, 213 x 213 regions in (Fulcher & Fornito, 2016), or 130 x 130 in (Rubinov *et al.*, 2015)), an option that greatly increases the computational tractability of the mouse connectome. The use of predefined meta-areas is however non ideal, as the sharp inter-areal boundaries that characterize most neuro-anatomical parcellations reflect a discretization of otherwise regionally continuous cytoarchitectural or anatomical parameters that may straddle cross-regional network features. Moreover, the use of meta-regions might limit the resolution of topological mapping in the mouse connectome, biasing the ensuing network metrics towards areas that are anatomically larger or more prominent, and potentially obscuring fine-grained or sub-regional attributes that could be critical to the network organization of the mammalian connectome. The recent release of a voxel-level data-driven model of the mouse connectome (Knox *et al.*, 2019) offers the possibility of overcoming the limitations or regional-aggregated investigations in this species. This resource entails an improved interpolation model for single tracer injection maps and provides whole-brain coverage, encompassing subcortical districts not covered by state-of-the-art parcellations (Oh *et al.*, 2014; Knox *et al.*, 2019). Moreover, the voxel-wise mouse connectome is characterized by a sampling resolution that is unprecedented

for mammalian species, offering the opportunity to probe the topological structure of the mammalian connectome at a regional-scale never investigated so far.

Here we leverage the voxel-level mouse connectome by Knox et al. (Knox *et al.*, 2019) to provide a brain-wide, high-resolution description of the network structure and hierarchical organization of the directed mouse connectome, unconstrained by regional partitioning (15,314 x 15,314 matrix, Voronoi voxel volume 0.027 mm^3 non isotropic, mean spatial extension of Voronoi voxels: 242 µm x 323 µm x 336 µm, see Materials and Methods). Our results show that the mouse connectome is characterized by a finer network topography than previously reported, uncovering some previously underappreciated network features of the mammalian connectome. These include a segregation of hub regions into source and sink nodes, pointing at an organizational hierarchy in which higher order cortical areas serve as primary sources of neural output to the rest of the brain, and basal ganglia are configured as pivotal recipients of incoming projections. Using in silico network attacks, we also uncovered a strategic role of ascending modulatory nuclei as essential orchestrators of network communicability, a connectional property that makes these systems points of vulnerability for network function. We also found a tight inter-dependence between functional and structural brain organization, entailing the spatial arrangement of mouse cortical areas according to a hierarchy reflecting unimodal-transmodal and modality-specific functional processing, hence broadly reconstituting basic organizational principles of the primate brain. Our findings define a high-resolution structural scaffold linking mesoscale connectome topography to its macroscale functional organization, and create opportunities for identifying targets of interventions to modulate brain function in a physiologically-accessible species.

2.2 Materials and Methods

Construction of the structural connectome

Our work leverages a high-resolution models of the mouse brain connectome (100 μm^3) previously released by Knox and colleagues (Knox *et al.*, 2019). The Knox connectome is based on 428 viral microinjection experiments in C57BL/6J male mice obtained from the Allen Mouse Brain Connectivity Atlas (http://connectivity.brain-map.org/). The connectome data were derived from imaging eGFP-labeled axonal projections which were then registered to the Allen Mouse Brain Atlas, and aggregated according to a voxel-wise interpolation model (Knox *et al.*, 2019). All the additional computational steps detailed below were implemented to make this resource computationally tractable and suited to the topological analyses we described in our manuscript. Before constructing the structural connectivity (SC) matrix, we ensured symmetry along the right-left axis for all the major macrostructures of the mouse brain. This step was required because the computation of most graph-based metrics require the use of a square connectivity matrix as input. To this purpose, we flipped each macrostructure (isocortex, hippocampal formation, sub-cortical plate, pallidum, striatum, pons, medulla, midbrain, thalamus, hypothalamus, cerebellum, and olfactory bulb) along the sagittal midline (once for the right hemisphere and once for the left hemisphere) and we took the intersection with the respective non flipped macrostructure This procedure resulted in the removal of a set of non-symmetric voxel (total fraction, 8.6%), the vast majority of which residing in fringe white/gray matter or CSF/gray matter interfaces. Importantly, the removal of these non-symmetric voxels did not substantially affect the network structure of the resampled connectome, as assessed with a spatial correlation analysis between the symmetrized and non-symmetrized right ipsilateral (i.e. squared) connectome (spatial correlation 0.98, 0.93, and 0.97 Spearman Rho, for global, incoming and outgoing connectivity strength, respectively). We then filtered out fiber tracts and

ventricular spaces, and estimated SC using a resampled version of the recently published voxel scale model of the mouse structural connectome (Knox *et al.*, 2019), to make the original matrix computationally tractable. Resampling of the Knox et al. connectome was carried out by aggregating neighboring voxels according to a Voronoi diagram based on Euclidean distance between neighboring voxels (Fig. 6). Voronoi-based resampling allowed us to spatially weight voxels with respect to neighboring areas, preserving the intrinsic architectural foundation of the connectome (Knox *et al.*, 2019). Moreover, this procedure allowed us to minimize spatial blurring and boundary effects between ontogenically distinct neuroanatomical divisions of the mouse brain, or white/grey matter, and parenchymal/ventricular interfaces. Finally, by averaging the connectivity profile of neighboring voxels based on their relative spatial arrangement, this strategy has also the advantage of mitigating limitations related to the enforced smoothness of source space employed by the original kernel interpolation employed by Knox *et al.*, (2019).

The employed Voronoi-based aggregation strategy entails the identification, for each voxel of the mouse connectome, of its 27 closest neighbors as per Euclidean distance (Figure 6), and the subsequent averaging of their connectivity profiles into a single value. We also made sure not to include the same 27 voxels in the computation of a new down-sampled voxel, to avoid spatial redundancy and oversampling. As a trade-off between spatial resolution and computational tractability, we decided to reduce spatial resolution by a factor of three, therefore aggregating the connectivity profile of 27 voxels into a single one. To keep the estimation of structural connectivity consistent with the procedure of Knox *et al.*, (2019) and minimize mixing or cross-regional anatomical features, a Voronoi diagram was computed for each of the 12 same major brain divisions of the Allen Institute atlas separately and for one hemisphere only, flipping the resulting diagram across the sagittal midline to ensure Voronoi grid symmetry across the two hemispheres. Given that

connectome resampling was carried out on the original 100 µm-resolution connectome from Knox *et al.*, (2019) the resulting averaged Voronoi voxels are characterized by a total volume of 0.027 mm^3 but are not necessarily isotropic or regular. The average spatial extension of the obtained Voronoi voxels in each plane corresponds to 242 µm x 323 µm x 336 µm in the x (sagittal), y (horizontal) and z (coronal) planes, respectively.

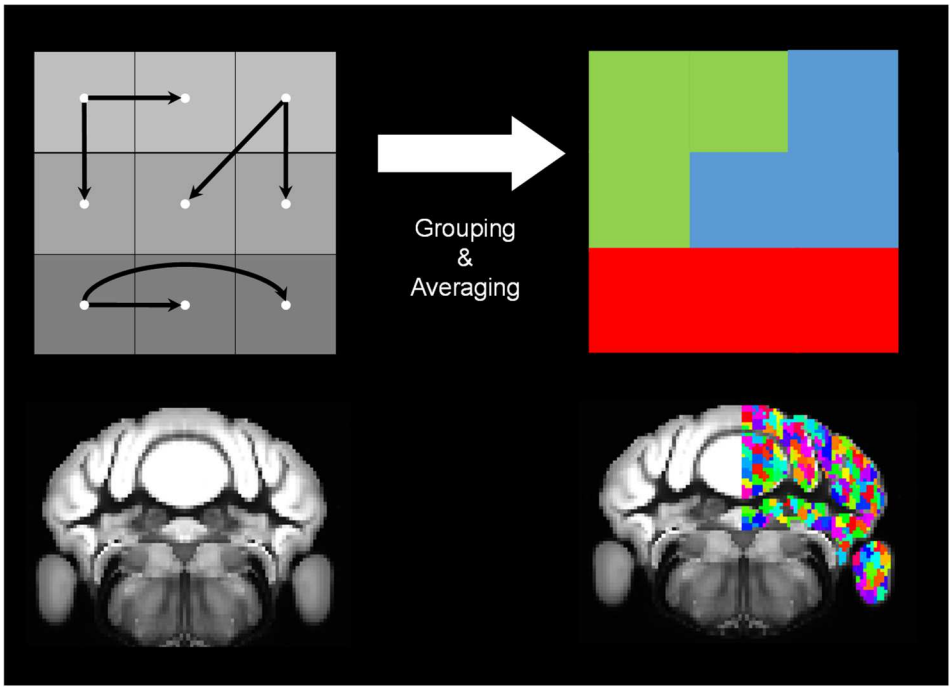

Figure 6. Voronoi resampling scheme of the mouse brain connectome. Top row: Two-dimensional representation of the employed Voronoi-sampling procedure. For each voxel of the mouse brain in the CCFv3 space, we identify its 27 closest neighbors as per Euclidean distance, averaging their connectivity profiles into a single value. Bottom row: Resulting Voronoi tessellation of the mouse cerebellum.

To probe whether the employed Voronoi re-sampling procedure (and the resulting anisotropic Voronoi voxels) would affect the connectional and spatial properties of the mouse connectome, we computed for each Voronoi voxel, the average spatial correlation between the connectivity profile of each of its 27 original constituting 100 μm^3 voxels across 12 macrostructures. This computation

yielded an average Spearman rho correlation of 0.98, 0.96, 0.99, 0.99, 0.99, 0.99, 0.99, 0.998, 0.97, 0.98, 0.98, and 0.99 for the cerebellum, subcortical plate, hippocampal formation, isocortex, medulla, midbrain, olfactory areas, pallidum, pons, striatum, and thalamus, respectively, corroborating the specificity of the employed resampling strategy and suggesting that the resampled connectome offers a reliable fine-grained representation of the most salient connectional features of the original Knox et al connectome.

A whole brain connectome was then built under the assumption of brain symmetry (Rubinov *et al.*, 2015). Forty-four dangling nodes (i.e. nodes with no outgoing connectivity) were next removed from the resulting matrix, resulting in a final weighted and directed 15,314 x 15,314 matrix composed of 0.027 mm^3 aggregate Voronoi voxels. The obtained Voronoi diagram allowed us to map the results back into the original 100 µm three-dimensional coordinate system of the Allen Institute mouse brain connectome (CCFv3 (Wang *et al.*, 2020)).

Both the original voxel-wise connectome from Knox *et al.*, (2019) and our resampled version were almost 100% dense, raising the issue of how to account for and remove weak or irrelevant connections. To address this problem we employed a recently developed method based on graph percolation (Bordier *et al.*, 2017). Briefly, this procedure consists in iteratively removing the weakest connections until the giant component of the graph starts breaking apart. The threshold that maximizes sparsity without breaking the giant component (i.e. the largest integral graph within the matrix) is the one that should be selected for the analysis. Bordier *et al.*, (2017) showed that the threshold obtained through percolation analysis maximizes information on the network community structure. This sparsification procedure resulted in a network density of 22%. Importantly, a comparison of multiple topological attributes and metrics (i.e. global, sink, source hubs, in/out ratio, modules and gradients) at different thresholds (percolation threshold, 30% and 40%, respectively)

revealed that all the probed parameters are highly robust to thresholding (Dice coefficient > 0.97 for all modules and hubs at all thresholds; Spearman rank correlation > 0.99 for Out/in ratio and > 0.97 for all gradients, at all thresholds).

Regional quantifications of network properties and correlations between structural and functional attributes were carried out using three main sets of predefined anatomical parcellations of the mouse connectome. To quantify the subregional localization of network attributes (Figure 11), we employed one of the finest parcellation available of the mouse connectome (i.e. the lowest hierarchical level in the Allen Mouse Brain Atlas, excluding layer-encoding, (Wang *et al.*, 2020)). This parcellation was volumetrically matched to the sampling dimension of our voxels by discarding small nuclei whose spatial extension was – for either hemisphere – lower than the resolution of our voxel-wise connectome (45 regions out of 323, Table 1). Regional quantifications of sub-regional localizations were then limited to the remaining set of 278 areas. Correlation between functional and structural connectivity was carried out on a set of meta-regions to reduce spatial resolution and maximize the contrast with corresponding correlations at the voxel-level. The list of the 89 regions used for such comparisons is reported in Table 2. Meta-regions were selected such to cover the anatomical distribution of the functional modules described in (Liska *et al.*, 2015)). Regional quantification of structural gradient features and cortical hierarchy were carried out using the original cortical parcellation described in (Harris *et al.*, 2019), corresponding to the isocortical subset in Table 1. Finally, to probe the robustness and resolution dependence of the topological properties we described in the present work, we re-computed all the network attributes and metrics using the state-of-the-art parcellated mouse connectome described in Oh *et al.*, (2014) (426 x 426 connectivity matrix).

Hub and rich club mapping

Normalized out-strength (source), in-strength (sink), and in+out strength (global) hub regions of the voxel-wise connectome were computed at the percolation threshold. To map the anatomical extension of hub-like areas and obtain an "hubness" index for individual voxels, for each metric we first iteratively identified and labelled the highest-ranking voxels at increasing percentile threshold (50^{th} to 99^{th}). The obtained information was then combined into a single frequency (%) map by plotting the number of times a voxel was labelled as hub across varying percentile thresholds. We limited the visualization to the nodes that were classified as hubs at least 90% of the times, with the aim to capture top strength nodes and produce heatmaps where hotter colors indicate hub-like voxels corresponding to highest percentile ranking. This approach ultimately led to the final representation of nodes exceeding the 94% strength percentile for all hub categories. Importantly, no correlation between global connectivity strength (total, incoming, outgoing) and injection density or distance inferred from Knox et al., (2019) was observed ($p > 0.6$, $r < 0.17$, all six correlation pairs, Figure 7), arguing against a confounding contribution of regional injection inhomogeneity in our sub-regional hub mapping.

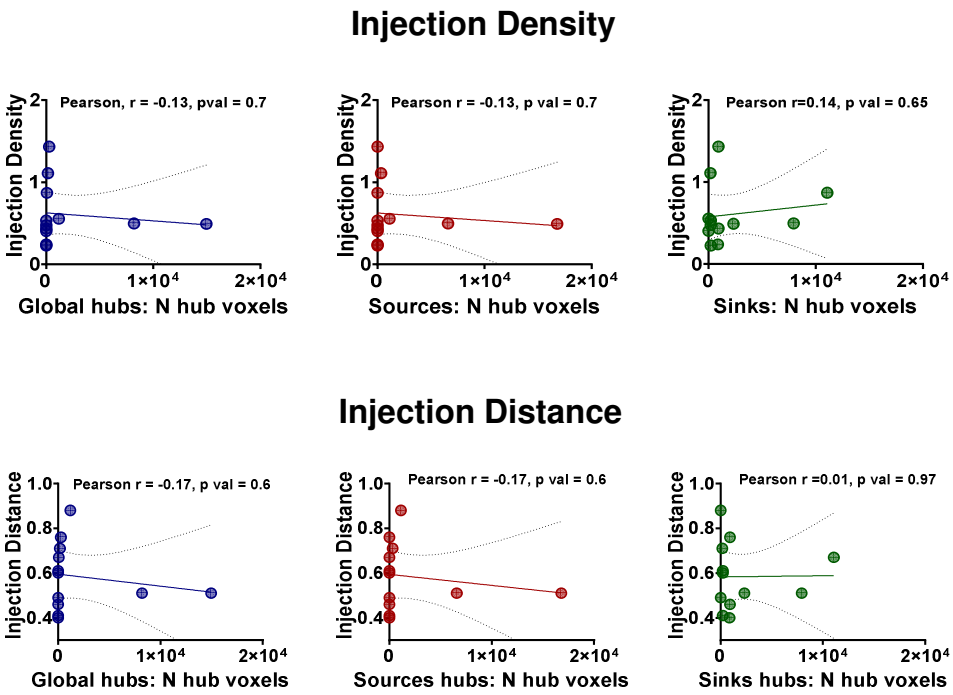

Figure 7. Hub mapping is distance and injection density independent. We plotted the number of voxels labelled as global strength hubs, source or sinks hubs as a function of mean injection distance (inferred from (Knox et al., 2019)) for each of the 12 major anatomical divisions of the mouse brain employed in our study and used by (Knox et al., 2019). Hub identification in our voxel-wise connectome did not appear to be affected by regional injection density or distance.

The network core or "rich club" of the mouse connectome was mapped using with the weighted variant described in Fulcher & Fornito (2016), limiting the analysis to the weighted ipsilateral connectome to ensure the computational tractability of the corresponding null models (Fulcher & Fornito, 2016). Specifically, we first obtained a percolation threshold specific for the ipsilateral connectome, and we then computed the normalized rich club coefficient, defined as the ratio between the empirical rich club coefficient and the rich club coefficient obtained from an ensemble of 1,000 rewired networks where each network maintained the empirical in and out degree, together with the total wiring length of each node (as assessed by Euclidean distance, (Maslov & Sneppen, 2002; Samu *et al.*, 2014)). Due to the high computational demands of the rewiring procedure, we left a margin of 5% error on nodal wiring length constraint. Instead of testing all possible degree

configurations, which usually range from 1 to *k* with k being the highest degree found in the network, we restricted the mapping between 6'720 and 8'143, corresponding to the 90th and 99th percentile, respectively, of the total degree distribution. This choice was motivated to both reduce the influence of low degree nodes, unlikely to represent hubs of the network, and to reduce the computational demands associated with rich club mapping with our high-resolution matrix. Statistical significance ($P < 0.05$) was assessed by obtaining a P value directly from this null distribution. Across all normalized rich club coefficients, we next computed for each node the fraction of times it was included in the rich club to produce a frequency map, similarly to the procedure described for the definition of source, sinks, and global hubs. Given the more restricted percentile range explored for the rich club with respect to global hubs, the rich club (Fig. 9B) was mapped over a wider frequency range (0.2-1) than the other metrics. We observed that all rich club coefficients tested in the above-mentioned range yielded statistically significant results ($p < 0.001$).

Multiscale modular decomposition and participation coefficient

We analyzed the network structure of the weighted and directed mouse structural connectome using the Louvain algorithm as implemented in the Brain Connectivity Toolbox (Rubinov & Sporns, 2010). Similarly to the procedure outlined in Rubinov *et al.*, (2015), we systematically varied (from 0.3 to 3.0 in 0.1 step, 100 repetitions at each step) the resolution parameters controlling the size of the modules, performing consensus clustering (Lancichinetti & Fortunato, 2012) and thus obtaining a representative community subdivision for each of the tested resolution setting. As in Rubinov *et al.*, (2015), we next sought to identify a range of gamma yielding topographically stable partitions (Figure 8). To this purpose, we computed adjusted mutual information to assess the spatial similarity between the modular partitions obtained at different gamma values, producing a γ x γ matrix.

We next computed, for increasing mutual information thresholds (ranging from 0.9 to 1.0 - 0.005 step), a modular partition of the corresponding γ x γ matrix via a consensus clustering (Lancichinetti & Fortunato, 2012). The identified modules in these γ x γ matrices define a discrete γ interval within which modular partitions of the connectome are topographically comparable. We finally obtained a single agreement matrix by computing the binarized fraction of times each pair of nodes (i.e. gamma values) would be classified as part of the same module, for each modular partition of the thresholded γ x γ matrices. The resulting final γ x γ matrix (Figure S8) is assumed to provide an optimized representation of the discrete gamma intervals yielding stable modular partitions across spatial resolution hierarchies. Given the focus of this work on brain-wide network organization and its relationship with previous community partitioning of large-scale functional connectivity, for all subsequent analyses, we focused on the first stable hierarchy level ($0.6 < Y < 1.1$). Using normalized mutual information index (as in (Rubinov *et al.*, 2015)) instead of the adjusted mutual information yielded similar results, with highest hierarchy level being identical across the two measures. Within the chosen $0.6 < Y < 1.1$ interval, we selected $\gamma = 1$ as representative resolution parameter, and at the selected spatial scale, we run 500 independent iterations of the Louvain algorithm, followed again by consensus clustering. Importantly, a computation of the Dice coefficient for all the structural community across all the $0.6 < Y < 1.1$ interval (0.1 step) produced mean values of 0.98, 0.98, 0.98. 0.93, and 0.94 for the cerebellar-pontine, basal-olfactory, hippocampal, default-mode, and latero-cortical modules, respectively supporting the validity of our gamma selection, and corroborating the notion of a stable partition topography within the selected $0.6 < \gamma < 1.1$ range. We finally probed the statistical significance of the final partition against 1,000 randomly rewired networks characterized by the same empirical in and out degree distribution, and by maintaining the total wiring length of each node (Samu *et al.*, 2014; Fulcher & Fornito, 2016). Specifically, we used the total connectivity

strength within each module as significant variable, reasoning that the internal cohesion of a given partition should be higher than expected by chance. We found that the total connectivity strength of each module always exceeded the total connectivity strength of the 1,000 rewired networks, suggesting that the degree sequences as well as the total wiring length of each node cannot adequately account for the spatial organization of the communities of the mouse structural connectome.

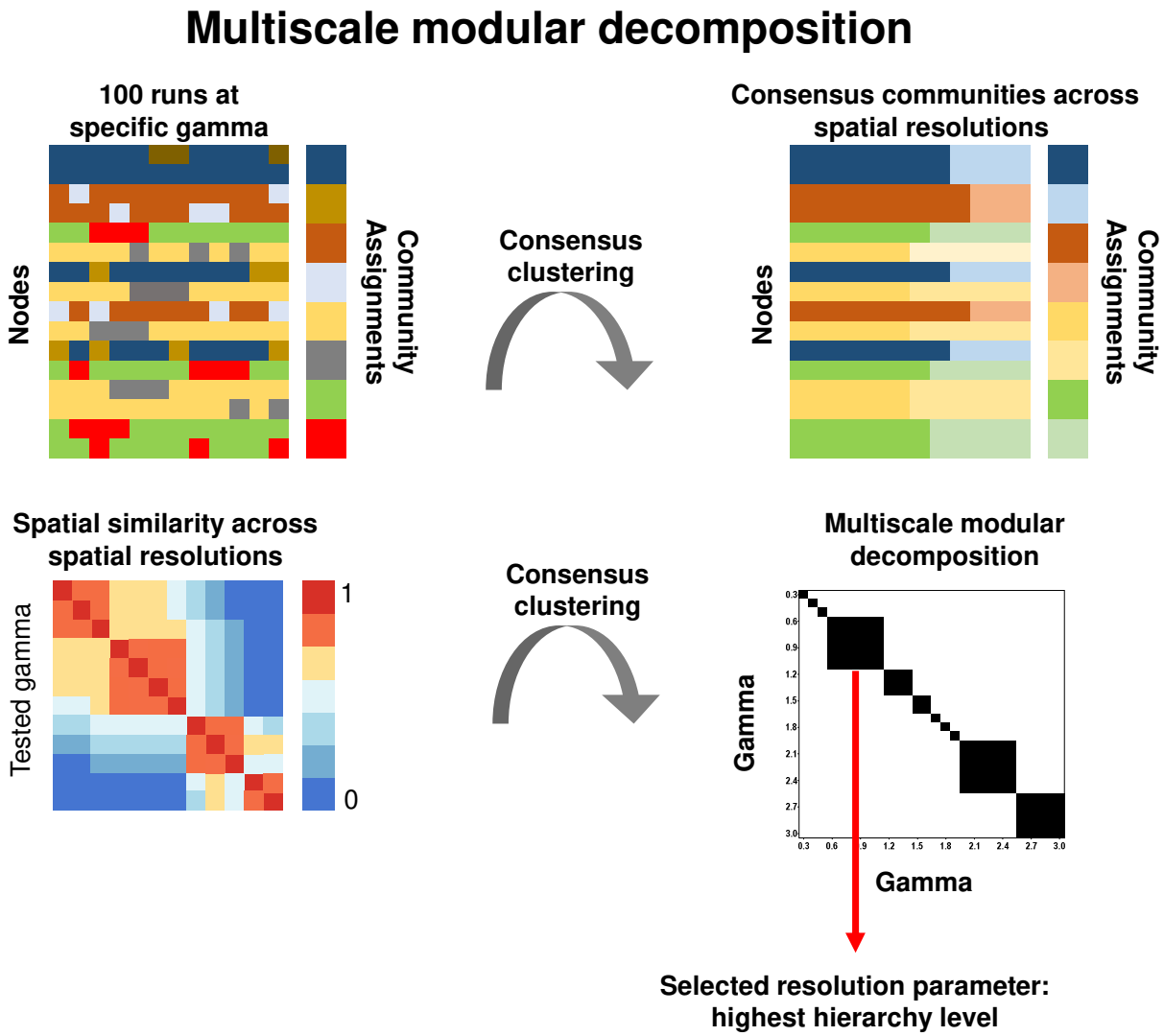

Figure 8. Multiscale modular decomposition of the structural connectome. We systematically varied the resolution parameter controlling the size of the modules, performing a consensus clustering and thus obtaining a

representative community subdivision for each of the tested resolution setting as originally described by (Rubinov et al., 2015), (top row). We then computed similarity between all the consensus partitions using the adjusted mutual information (AMI) score (bottom left). We next iteratively applied a mutual information (AMI) threshold to the similarity matrix, employing consensus clustering to obtain, for each AMI threshold, a community subdivision of the resolution landscape. We finally computed an agreement matrix to obtain a binarized gamma x gamma matrix grouping the original voxel-wise modules based on the similarity of their spatial topography as a function of gamma (bottom right – note this is the actual gamma x gamma matrix pertaining our analyses). The identification of discernible gamma x gamma clusters in this matrix is indicative of the presence of discrete gamma intervals within which the corresponding voxel-wise communities are topographically stable and similar. We based all subsequent analyses on the partition obtained at the first stable highest hierarchical level (i.e. lower gamma range), testing its statistical significance against a set 1,000 rewired networks with preserved degree and strength sequences, and where we additionally controlled for nodal wiring length, as assessed by Euclidean distance.

Module topography in the structural connectome was further corroborated using an agglomerative hierarchical clustering procedure of a matrix obtained by computing between-nodes similarity (as by Spearman Rank correlation) based on the connectivity profile of each node. A comparison of the obtained clusters using the dice coefficient revealed an overall high concordance between the results obtained with these two procedures. We found a dice coefficient of 0.7 for the DMN, 0.82 for the LCN, 0.91 for the hippocampal module, and 0.92 for the olfactory-basal forebrain community. Finally, we found that the pontine-cerebellar module was almost equally represented by two clusters, one encompassing the cerebellum, and the other covering pons and medulla (dice coefficient of 0.66 and 0.56, respectively).

Our module detection procedure led to the identification of N = 7 modules, including two symmetric monohemispheric DMN and two olfactory-basal forebrain components, which we have joined into a single module for consistency with functional mapping and before computing their significance. The functional (rsfMRI) modules described in Figure 14 were obtained from (Liska *et al.*, 2015). The procedure for functional module detection has been extensively described in the original work (Liska *et al.*, 2015). To better match SC and FC modules, the basal forebrain and ventral midbrain

modules identified in Liska *et al.*, (2015) were merged together to constitute a single ventral brain community. Finally, to map the anatomical extension of global (in+out), in-, and out-connector hubs, we carried out a voxel-wise computation of participation coefficient (i.e. a network measure of connection diversity, (Guimerà & Nunes Amaral, 2005)), and iteratively identified and labelled the highest ranking voxels at increasing percentile threshold (50^{th} to 99^{th}). The obtained information was then combined into a single frequency (%) map by plotting the number of times a voxel was labelled as hub across varying percentile thresholds. We limited the visualization to the nodes that were classified as hubs at least 90% of the times.

Virtual lesion mapping

The role of hubs for the network global functioning was probed by means of targeted virtual attacks. For each of the metrics of interest (in- and out strength, and global participation coefficient), we removed a given fraction of the highest ranking nodes (from 5 to 40%, in 5% step by zeroing all the incoming and outgoing connections), comparing the size of the giant component, global efficiency (measured as the average inverse shortest path length), and total network communicability, here limited to map path length ≤ 3 corresponding to a polysynaptic connectome (Benzi & Klymko, 2013). Metrics were computed pre- and post-attack, and changes with respect to these indices were expressed as a percentage of the intact network's value. For each fraction of removed nodes, we compared targeted hubs deletion to 1000 random attacks, assessing statistical significance ($P < 0.05$) by obtaining a P value directly from the null distribution. To limit inferences of virtual lesions to a nodal range that is biologically meaningful, we restricted the illustration of in silico lesions to the 5-20% range (Figure 16).

Functional and structural gradients

Gradient computations were explicitly aimed at probing the presence of evolutionarily relevant mouse cortical topographies capturing the polymodal-unimodal and modality specific organization of cortical connectivity previously reported for the human and primate brain (Margulies *et al.*, 2016; Oligschläger *et al.*, 2019). To this aim, we applied diffusion map embedding on SC and functional connectivity (FC) as previously described (Margulies *et al.*, 2016; Vos de Wael *et al.*, 2020). Briefly, this nonlinear dimensionality reduction technique seeks to project high dimensional connectivity data into a lower dimensional Euclidean space, identifying spatial gradients in connectivity patterns. The cortical SC (FC) matrix is first mapped into an affinity matrix that represent the similarity of connectivity profiles across nodes. The eigenvectors describing the diffusion operator formed on the normalized graph Laplacian of the affinity matrix identify gradients in connectivity patterns over space.

To compute SC gradients, we first extracted from the non-thresholded whole brain connectome the nodes belonging the isocortex, and we next computed a new threshold via percolation analysis resulting in a density of 7%. The structural affinity matrix was then built based on the connectional profile of each node, i.e. by incorporating the information provided by both incoming and outgoing connections. The functional affinity matrix was built using the same steps described by Margulies *et (al.*, 2016). In reporting the results, we explicitly looked for gradients capturing polymodal-unimodal sensory-fugal differentiation as well as a modality specific organization of cortical connectivity as described in recent human and primate work (Margulies *et al.*, 2016; Oligschläger *et al.*, 2019). To this purpose, we first ranked SC and FC gradients based on explained variance (Fig. 19). We next visually inspected the top three ranking SC and FC gradients and found that the SC and FC gradient #1 were characterized by a clear unimodal-polymodal differentiation (Gradient A in Figure 18A and

18B), whereas the second ranked functional and the third ranked structural gradients delineated a comparable modality specific spatial configuration of cortical connectivity (Gradient B). In keeping with this observation, these pairs of FC and SC gradients exhibited highly concordant topographies (Fig. 19, Spearman Rho 0.83 and 0.78, respectively).

We additionally computed the correlation between SC gradients spatial maps and a dominant rsfMRI co-activation patterns (CAPS) published by Gutierrez-Barragan *et al.*, (2019), in an attempt to establish a link between the organization of the structural connectome and FC dynamics. In their work, Gutierrez-Barragan *et al.*, (2019) described three pairs of recurring oscillatory states account for the more than 60% of rsfMRI variance. Notably, two of these oscillating patterns are characterized by a conserved cortical topography entailing the opposing engagement of latero-cortical and DMN regions reminiscent of the mapped cortical gradients, the main difference between them being a differential involvement of subcortical structures (i.e. hippocampus). To correlate the topography of these dominant co-activation patterns with that of the structural gradients, we therefore generated a mean cortical CAP out of these two fluctuating states, using the mean value across the hemispheres. We did not consider the third pair of states (CAPs 3 and 4 in (Gutierrez-Barragan *et al.*, 2019)) owing to its more widespread cortical topography and strong coherence with fMRI global signal, implicating the involvement of a possible global external input to the emergence of this meta-state. Finally, we also computed the correlation between SC gradients and cortical hierarchy scores computed on the basis of feedforward-feedback laminar connectivity patterns of the mouse brain as described and computed in Harris *et al.*, (2019), using the same set of cortical brain regions described by the authors. For all the spatial correlational analyses involving gradients, we accounted for the spatial autocorrelation using Moran spectral randomization as implemented in the BrainSpace toolbox,

using Euclidean distance between nodes as input for computing the Moran eigenvector maps (Vos de Wael *et al.*, 2020).

rsfMRI data

The rsfMRI dataset used in this work consists of N = 15 scans in adult male C57Bl6/J mice which are publicly available (Gutierrez-Barragan *et al.*, 2019; Grandjean *et al.*, 2020). All in vivo experiments were conducted in accordance with the Italian law (DL 26/214, EU 63/2010, Ministero della Sanita`, Roma) and the recommendations in the Guide for the Care and Use of Laboratory Animals of the NIH. Animal research protocols were reviewed and consented by the animal care committee of the Italian Institute of Technology, and Italian Ministry of Health. Animal preparation, image data acquisition, and image data preprocessing for rsfMRI data have been recently described in greater detail elsewhere (Liska *et al.*, 2015; Gutierrez-Barragan *et al.*, 2019; Pagani *et al.*, 2019). Briefly, rsMRI data were acquired with a 7.0 Tesla scanner (Bruker Biospin, Ettlingen) equipped with BGA-9 gradient set, using a 72 mm birdcage transmit coil, and a four-channel solenoid coil for signal reception. Single-shot blood-oxygen level dependent (BOLD) EPI time series were acquired using an echo planar imaging sequence with the following parameters: TR/TE 1000/15 ms, flip angle 30°, matrix 100 × 100, field of view 2 × 2 cm^2, 18 coronal slices, slice thickness 0.50 mm, 500 (n = 21) or 1500 (n = 19) volumes and a total rsfMRI acquisition time of 30 minutes, respectively.

2.3 Results

Global hubs and rich-club core of the voxel-wise mouse connectome

A defining characteristic of brain connectomes is the presence of spatially localized set of integrative *hub* regions, characterized by high connectivity density (van den Heuvel & Sporns, 2013).

Hub regions serve as focal points of network interaction and exert a tight influence on the structure and dynamics of brain networks (van den Heuvel & Sporns, 2013). To identify regional features exhibiting hub-like properties at the voxel scale, we first mapped voxels exhibiting high connectivity strength using a spatially-resampled (15,314 x 15,314) version of the Allen Institute mouse connectome (Knox *et al.*, 2019), irrespective of the directionality of the connections. We termed the identified regions as *global hubs* to distinguish them from further hub identification carried out using the directed connectome (described below). This analysis revealed several focal areas exhibiting global hub-like properties (Figure 9A). Consistent with the high centrality of hub regions, the identified foci were prominently located in associative cortical areas such as the prefrontal, anterior cingulate, posterior parietal and retrosplenial cortices (Figure 9A). An additional large cluster of hub voxels was apparent in dorsal portions of the hippocampus. Finally, our fine-grained mapping also allowed the recognition of a small set of hub nodes in sub-regional portions of the basolateral and central amygdala.

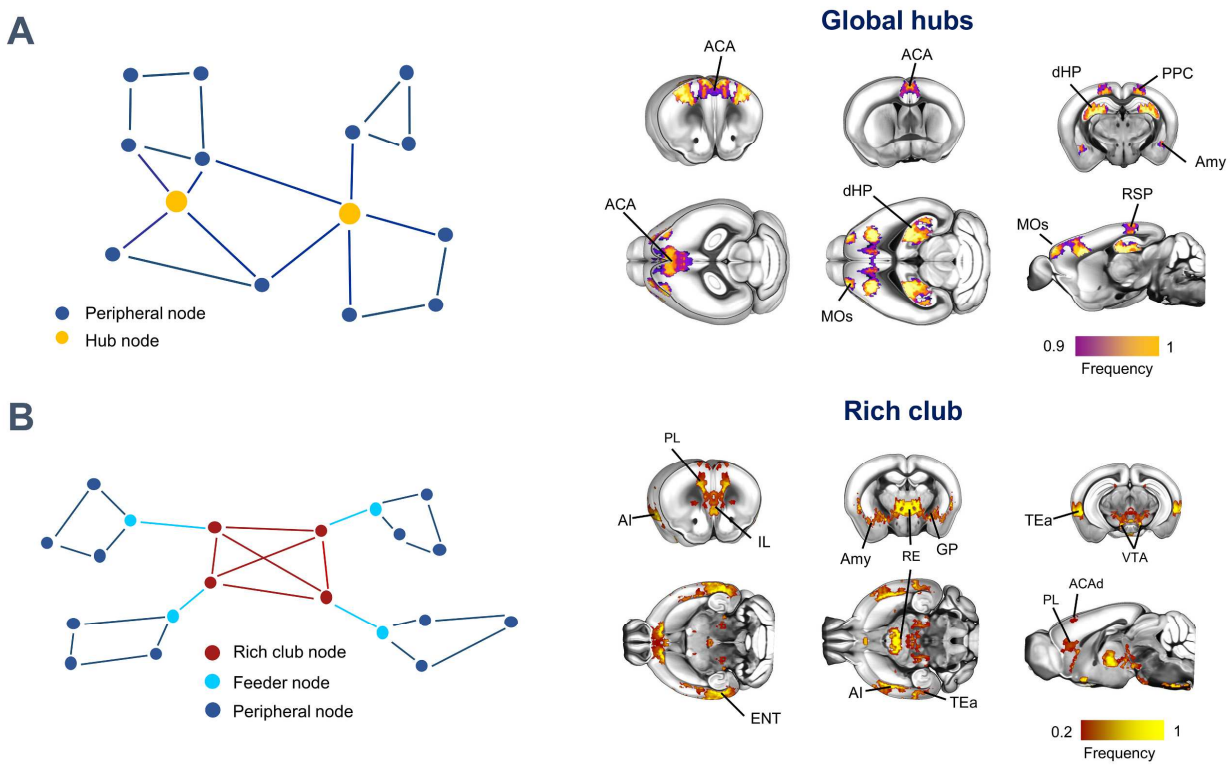

Figure 9. Global hubs and rich club of the mouse connectome. (**A**) Anatomical distribution of global hubs of the voxel-wise mouse connectome. Global hubs (yellow nodes on the left panel) were defined on the basis of nodal total strength. A frequency map was obtained by computing the fraction of times a node scored among the highest-ranking strength nodes, limiting the visualization to the nodes that were classified as hubs at least 90% of the time. (**B**) Anatomical distribution of the rich club (red nodes on the left panel) of the voxel-wise mouse connectome. The frequency map indicates fraction of times high-degree nodes were retained as significant with respect to a set of random networks. ACA, anterior cingulate area; ACAd, anterior cingulate area, dorsal part; AI, agranular insular area; Amy, Amygdala; dHP, dorsal hippocampal area; ENT, entorhinal area; GP, globus pallidus; IL, infralimbic area; MOs, secondary motor area; PL, prelimbic area; PPC, posterior parietal cortex; RE, nucleus reuniens; RSP, retrosplenial area; TEa, temporal association areas.

In brain networks, highly connected central hub nodes have a tendency to be tightly interlinked with each other, defining a core network structure, often referred to as *rich club*, which supports the efficient integration of otherwise segregated neural systems (Towlson *et al.*, 2013; Fulcher & Fornito, 2016). To obtain a description of the mouse brain rich-club unconstrained by pre-existing anatomical partitioning, we employed the procedure described by (Fulcher & Fornito, 2016) on the ipsilateral voxel-wise connectome, benchmarking our mapping against 1,000 weighted rewired networks

characterized by the same empirical in and out degree distribution (Maslov & Sneppen, 2002). The obtained map revealed a more extended spatial topography than observed with global hub mapping, encompassing two major antero-posterior integrative axes (Figure 9B and 10). The first of these included transmodal cortical integrators of sensory input (i.e. insula and temporal association cortex (Zingg *et al.*, 2014)). The second axis encompassed infralimbic and mid-thalamic components of the fronto-hippocampal gateway (Vertes, 2004). Nodal mapping also revealed the participation of midbrain nuclei such as the ventral tegmental area, pointing at a previously unappreciated involvement of ascending dopaminergic nuclei as integral components of the rich club of the mouse connectome.

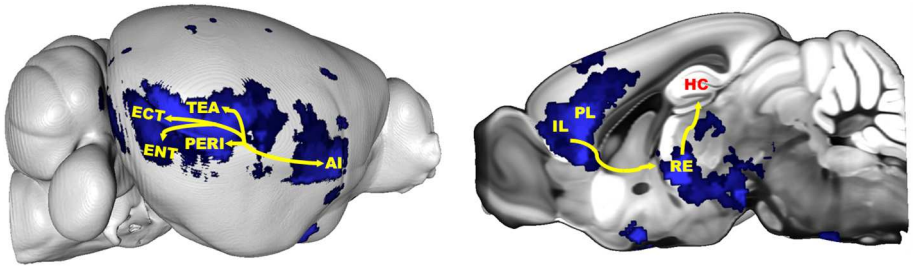

Figure 10. The rich club of the mouse connectome encompasses two major integrative axes of the mouse brain. The first axis (Left panel) is centered on transmodal cortical integrators of sensory input (i.e. insula and temporal association cortex, (Zingg et al., 2014).

Importantly, the spatial extension of global hubs and rich-club voxels in most cases encompassed only a marginal portion of the corresponding anatomical structure as defined in the Allen Brain Atlas, significantly deviating from corresponding voxel-level distributions at the regional level (Figure 11). In keeping with this notion, a qualitative comparison of voxel-wise mapping with that obtained with a state-of-the-art anatomical parcellation (Oh *et al.*, 2014) revealed substantial differences in the anatomical distribution of hub-like and rich-club regions (Fig. 13). This result corroborates the

specificity of our findings, suggesting that prior mapping of hub-like properties in the parcellated connectome might have been resolution-limited.

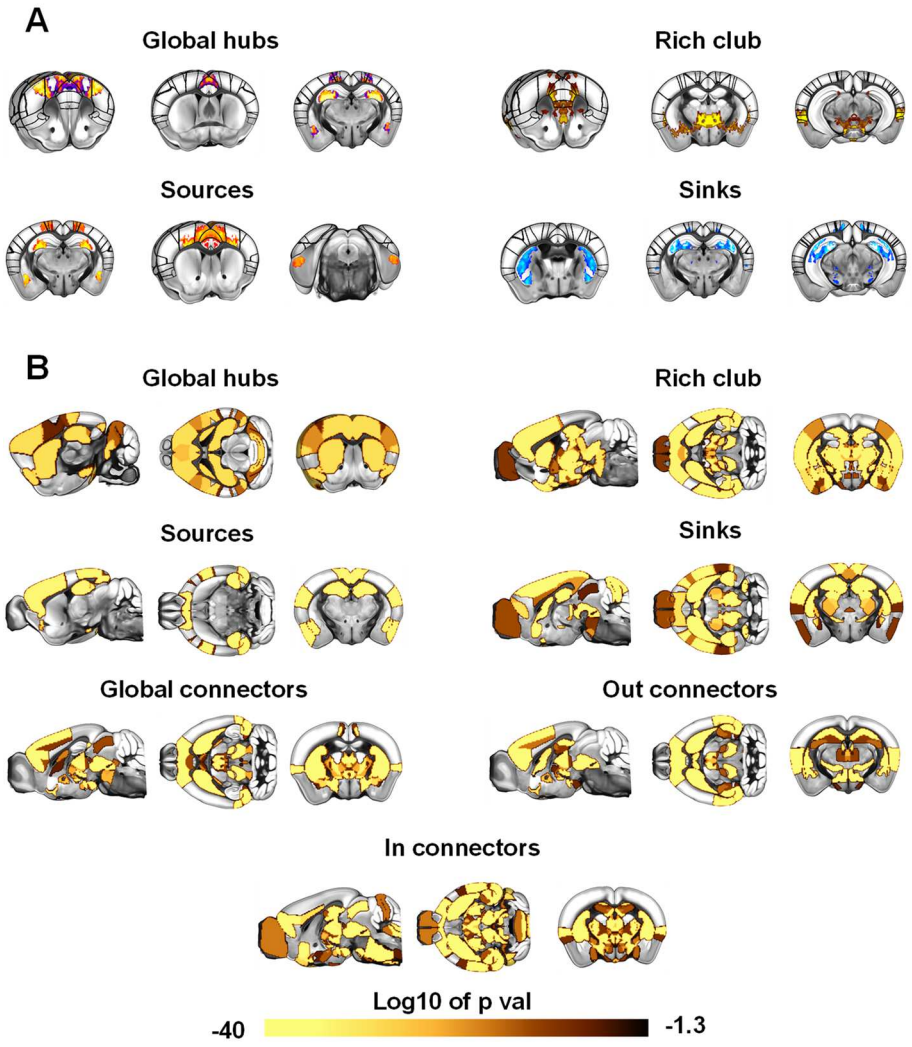

Figure 11. **Subregional localization of hub-like regions.** (A) Anatomical distribution of hub-like voxels with respect to a super-imposed cortical parcellation derived from the Allen Mouse Brain Atlas (CCFv3. Hubs-labelled voxels are often localized within sub-portions of cortical areas. No representation of connector hubs was generated given the negligible cortical location of this hub family (cf. Fig. 14). (B) Regional maps showing, for each anatomical district of

the mouse brain, how the distribution of hub-like voxels therein contained statistically deviate from the distribution of all the remaining (non-hub) voxels (Student t test).

Hub regions can be directionally segregated into neural sinks and sources

Our initial analyses were aimed at mapping global network features, and as such were carried out on a non-directed version of the mouse connectome. However, directionality is a fundamental feature of brain connectomes, and most structural brain networks are intrinsically directed because of the monodirectional nature of axonal projections. Thus, directional encoding can critically add key information to the topological organization of brain networks (Kale *et al.*, 2018), revealing organizational motifs that can be predictive of the information flow and hierarchical organization of the mammalian brain. To probe how the direction of structural connections affect network attributes, we parsed high connectivity strength regions based on their directional profile, resulting in the identification of a set of segregable nodes which we termed *source* and *sink*, characterized by high-strength outgoing or incoming connections, respectively (Figure 12A).

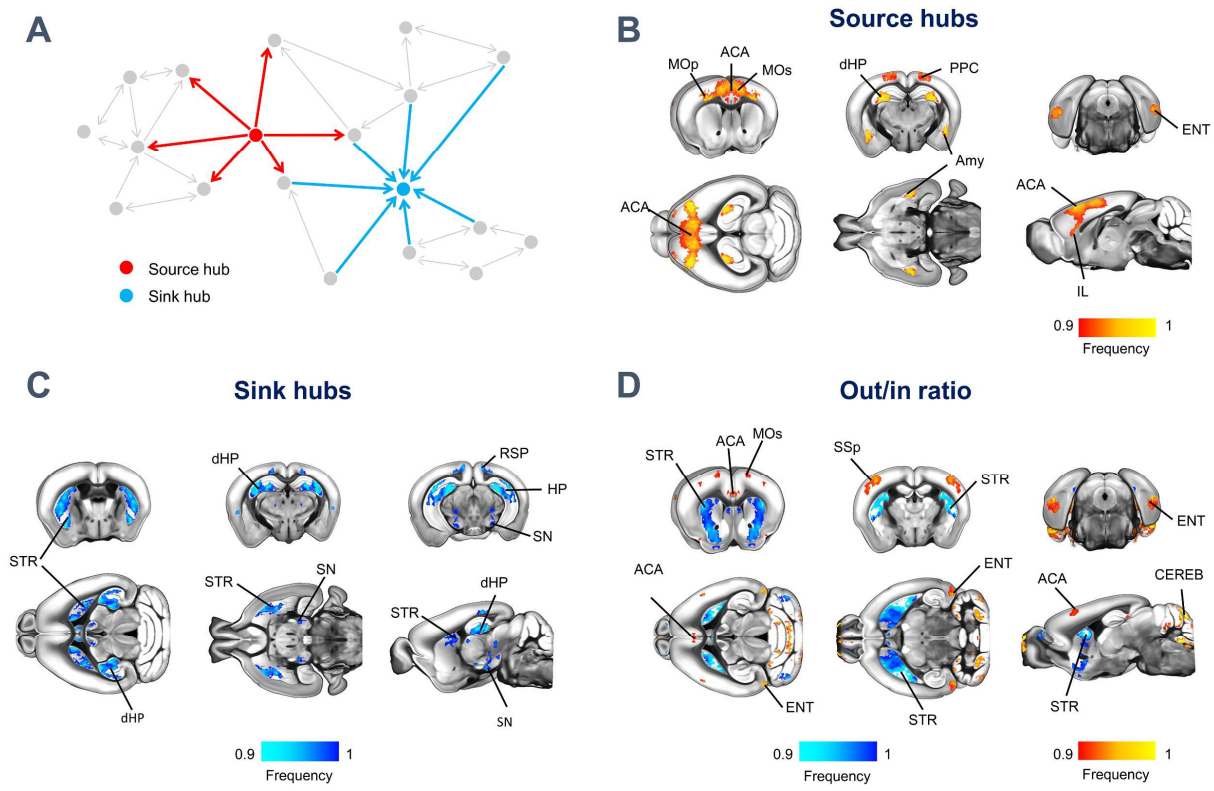

Figure 12. Source and sink hubs of the mouse connectome are spatially segregable. (**A**) Network schematic illustrating our topological classification of high strength regions into neural sources (red) and sinks (light blue). Source (**B**) and sink (**C**) hubs were defined on the basis of the voxel-wise strength of outgoing and incoming connectivity, respectively. Frequency maps were obtained by computing the fraction of times a node scored among the highest-ranking strength nodes, limiting the visualization to the nodes that were classified as hubs at least 90% of the time. (**D**) Out/in ratio mapping. For each node, we computed the ratio between the strength of the outgoing and incoming connectivity. Frequency maps were obtained by computing the fraction of times a node scored among the highest (red/yellow) or lowest ranking (light blue/blue) nodes as in (C) and (D). ACA, anterior cingulate area; Amy, Amygdala; CEREB, cerebellum; dHP, dorsal hippocampal area; ENT, entorhinal area; HP, hippocampus; MOp, primary motor areas; MOs, secondary motor area; PPC, posterior parietal cortex; RSP, retrosplenial area; SN, substantia nigra; SSp, primary somatosensory area; STR, striatum.

Source node distribution broadly recapitulated the location of global hubs, encompassing higher order areas such as the anterior cingulate and posterior parietal cortices, amygdala, dorsal hippocampus, together with posterior entorhinal areas (Figure 12B). Interestingly, mapping of sink nodes revealed the involvement of dorsal hippocampal areas along with a new set of substrates, which comprised the basal ganglia throughout their antero-posterior extent (Figure 12C).

Participation of nuclei within the *substantia nigra* was also apparent. These results show that high connection strength regions can be segregated based on their directional profile, and point at an organizational hierarchy in which higher order areas, such as the prefrontal cortex, serve as primary sources of neural output to the rest of the brain, while basal ganglia are pivotal recipients of incoming projections. In keeping with what we observed with hub and rich-club regions, the identified sink and source voxel clusters showed prominent sub-regional distribution with respect to pre-existing anatomical subdivision (Figure 11) and a remarkably different spatial organization when computed using an anatomical parcellation (Figure 13), corroborating the specificity of our fine-grained mapping with respect to canonical parcellation-based approaches.

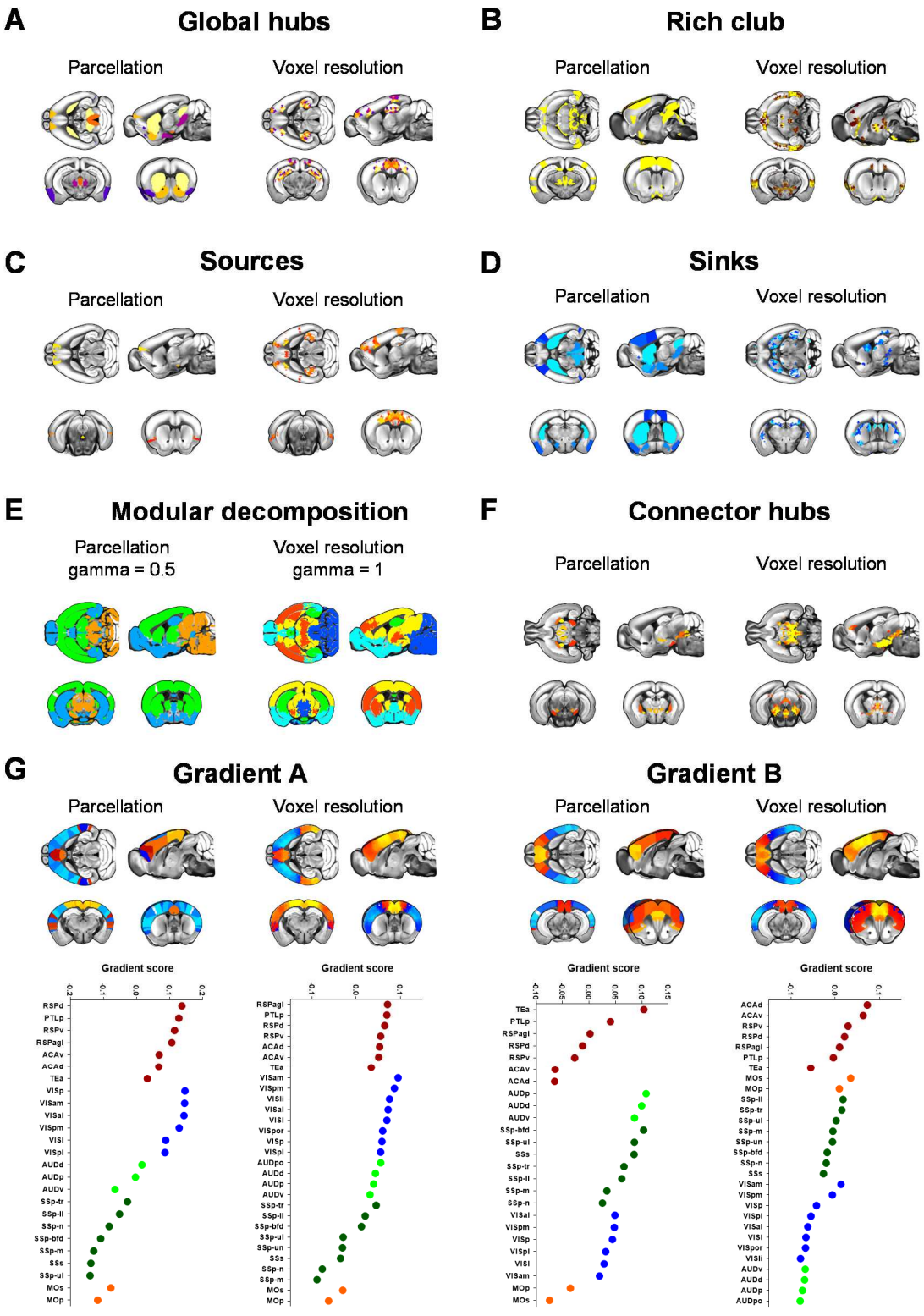

Figure 13. Parcellations conceal critical network attributes of the mouse connectome. We re-computed all the network attributes and metrics described in the present work using the parcellated connectome presented in Oh et al., 2014 (426x426 connectivity matrix). (A-G) Qualitative comparison of the topological properties at the voxel and regional

level. Global hubs (A) were defined on the basis on total node strength, whereas the parcellated rich club map in (B) was derived from (Fulcher & Fornito, 2016). We computed source (C) and sink (D) hubs by computing separately the strength of the outgoing and incoming connectivity, respectively. We obtained a multiscale modular decomposition of the parcellated connectome (E) with the same procedure outlined for the connectome with voxel resolution (see "Material and methods section), and we computed connector hubs (F) at the highest stable hierarchical level. Across all network metrics, hubs were defined with the same iterative procedure used for the connectome with voxel resolution. Similarly, we computed gradients (G) using the procedure described for the connectome with voxel resolution, comparing regional gradient scores across the most important functional circuits of the mouse brain (DMN, somatosensory, motor, auditory, and visual in red, dark green, orange, light green, and blue respectively).

The observation of segregable sink and source high-connection strength areas prompted us to investigate whether such a hierarchy could be expanded to non-hub areas (i.e. to all brain regions, independent of their connection strength), by computing the voxel-wise ratio between outgoing and incoming connection strength, a metric which we term "out/in ratio" (van den Heuvel, Scholtens, *et al.*, 2016). This analysis might allow us to differentiate regions characterized by a net connectional imbalance from those exhibiting both high input and output density (e.g. dorsal hippocampus). The resulting out/in ratio map (Figure 12D) revealed a prominent configuration of basal ganglia as regions characterized by a low ratio of outgoing/incoming connections, corroborating a configuration of these substrates as connectivity *sinks*. Conversely, foci exhibiting a high out/in connection ratio were identifiable in higher order cortical areas, such as the anterior cingulate and entorhinal cortices, but also prominently encompassed some *non-hub* substrates, such as the cerebellum, and primary motor-sensory regions. Taken together, these results show that the directed connectome is topologically rich and configured according to a global hierarchy that can be used to segregate regions in primary sources or receivers of axonal connections. Furthermore, they provide a fine-grained description of hub-like topography that may guide further targeted manipulations of salient network attributes in this species.

Structural communities of the voxel-wise connectome recapitulate large-scale fMRI networks of the mouse brain

The presence of distinct sub-networks or "communities" of tightly interlinked nodes is a hallmark of all mammalian connectomes mapped to date (Rubinov, 2016). Structural communities are composed of topologically-related neural elements reflecting regularities in wiring diagram, typically delineating groups of brain areas with shared functionality (Betzel & Bassett, 2017). Prior investigations of the community structure of the mouse connectome have been either anatomically biased by the use of metaregions (Rubinov *et al.*, 2015) or limited to the sole cortical mantle (Harris *et al.*, 2019), preventing a fine-grained description of the community structure of the entire mouse connectome. To identify stable brain-wide communities in the directed connectome with voxel-resolution, we used a multiscale modular decomposition approach (Rubinov *et al.*, 2015) (Figure 8). This approach revealed five prominent communities, encompassing different combinations of cortical and subcortical regions (Figures 14). Corroborating the robust structural foundations of rsfMRI network architecture (Margulies *et al.*, 2016; Buckner & DiNicola, 2019), the identified structural communities exhibited a spatial distribution closely recapitulating previously described resting state fMRI (rsfMRI) connectivity communities of the mouse brain (Sforazzini *et al.*, 2014; Liska *et al.*, 2015). The first of such communities comprised transmodal cortico-limbic areas as well as the dorsal striatum and antero-medial thalamus, spatially reconstituting key components of the mouse default-mode network (DMN, (Gozzi & Schwarz, 2016)). A second community encompassed latero-cortical motor-sensory areas, striatal and thalamic nuclei which have been previously characterized as component of the mouse *latero-cortical network* (LCN). This network is considered to be a possible evolutionarily precursor of the human "task-positive" network, as it appears to be tightly anticorrelated to DMN activity (Sforazzini *et al.*, 2014). A third module encompassed septo-

hippocampal areas, while the fourth comprised olfactory areas and basal forebrain regions, once again recapitulating corresponding rsfMRI functional communities (Liska *et al.*, 2015). Of note, anatomically similar structural connectivity partitions were also obtained using an agglomerative hierarchical clustering procedure (Dice coefficient 0.7, 0.8, 0.9, and 0.9 for the DMN, LCN, hippocampal system, and olfactory/basal forebrain moduli, respectively), corroborating the validity of the nodal partitioning reported here. By contrast, community detection in the parcellated connectome revealed three macro-modules (Figure 13) whose spatial topography was not directly relatable to corresponding rsfMRI communities, underscoring a closer structural-functional correspondence of the voxel-wise connectome with respect to parcellated connectome.

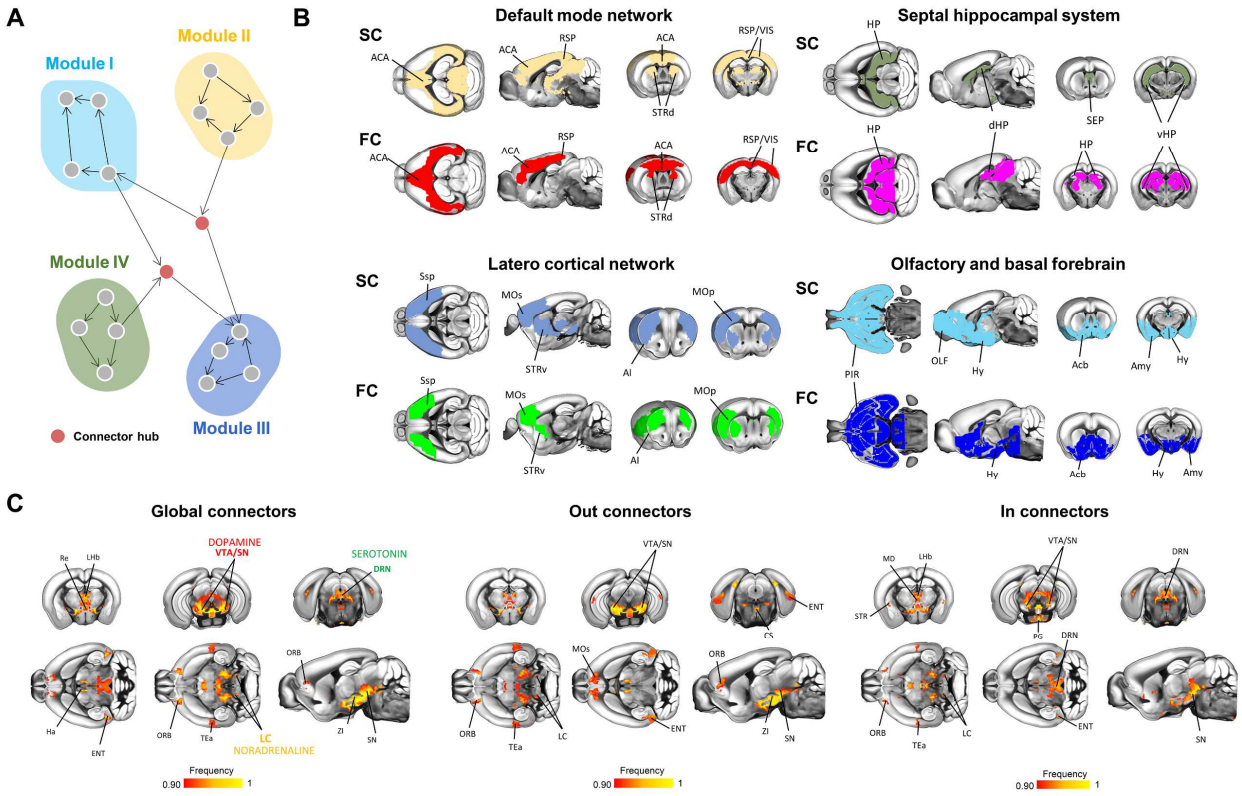

Figure 14. Connector hubs encompass key ascending neuromodulatory nuclei. (**A**) Network schematic illustrating a graph-based definition of communities and connector hubs. (**B**) Structural communities anatomically recapitulate functional (rsfMRI) networks of the mouse brain. Structural communities (SC; top row; see Materials and Methods) were matched to corresponding functional communities [FC; bottom row; Liska *et al.* (***19***)]. (**C**) Neuromodulatory nuclei are configured as connector hubs. Global (left), out-connector (middle), and in-connector (right) hubs were computed on the basis of the participation coefficient metric, accounting for outgoing or incoming connections only. ACA, anterior cingulate area; Acb, nucleus accumbens; AI, agranular insular area; Amy, amygdala; CS, superior central nucleus raphe; DRN, dorsal nucleus raphe; ENT, entorhinal area; HP, hippocampus; Ha, habenula; Hy, hypothalamus; LC, locus coeruleus; LHb, lateral habenula; MD, mediodorsal nucleus of the thalamus; MOp, primary motor areas; MOs, secondary motor area; OLF, olfactory areas; ORB, orbital areas; PG, pontine gray; PIR, piriform area; RE, nucleus reuniens; RSP, retrosplenial area; SEP, septal complex; STRd, striatum dorsal region; STRv, striatum ventral region; TEa, temporal association areas; vHP, ventral hippocampal area; VIS, visual areas; VTA, ventral tegmental area; ZI, zona incerta.

The close topographical overlap between voxel-wise structural communities and corresponding rsfMRI functional networks prompted us to probe the relationship between structural and functional connectivity (SC and FC, respectively) at the level of individual co-registered voxels. To this purpose, we carried out a correlation analysis between SC and FC for the DMN, LCN and hippocampal networks three well-characterized distributed mouse rsfMRI networks (Grandjean *et al.*, 2020) for which we

identified unambiguous structural correlates. In keeping with recent investigations in primates (Hori *et al.*, 2020), we found that voxel-wise correlation between FC and SC was non-linear, reflecting connection length dependent contributions (Figure 15). Specifically, functional-structural correlation was moderate to high (Spearman's rho 0.35, 0.45, and 0.34 for DMN, LCN, and the hippocampal network, respectively) for relatively short connections (<1 mm, e.g. the scale of mouse cortical width), but lower for longer-range links (> 2mm, Spearman's rho 0.26, 0.38, and 0.17 for DMN, LCN and hippocampal network, respectively). Consistent with the neural-mass nature of rsfMRI fluctuations, the correlation between FC and SC was robustly linear when both quantities were resampled at a lower spatial resolution using an anatomical parcellation (Pearson's r, 0.59, 0.55, 0.54, $p< 0.0001$ for the DMN, LCN, and hippocampal network, respectively). Taken together, these findings underscore the robust structural foundations of functional network activity as inferred from rsfMRI and suggest that spontaneous fMRI signal fluctuations underscoring macroscale rsfMRI coupling reflect the pooled activity of large ensembles of neurons, exceeding the finer spatial scale of the voxel-wise mouse connectome (Deco *et al.*, 2008; Breakspear, 2017; Gutierrez-Barragan *et al.*, 2019).

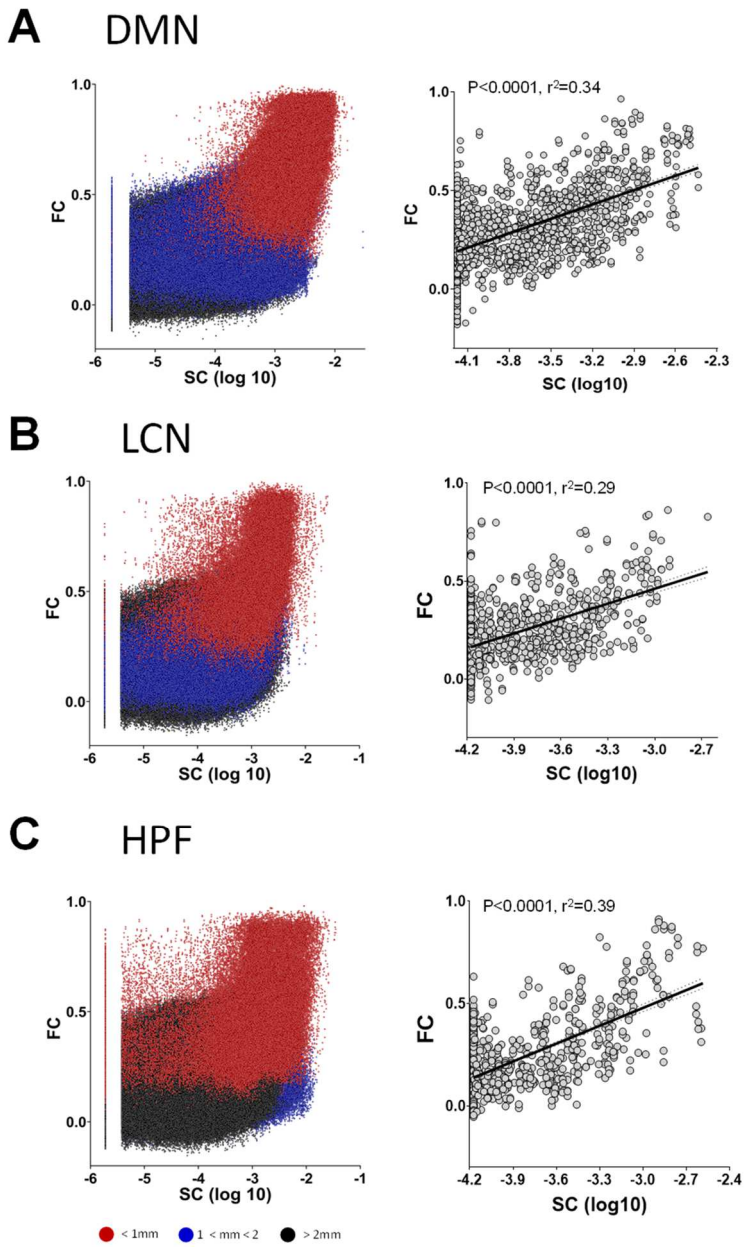

Figure 15. SC-FC correlation is distance dependent. (A) SC-FC correlation for the Default Mode network module obtained by (Liska *et al.*, 2015). The correlation was computed at both the voxel level (left panel) and after aggregation in regions of interest (right panel). (B) SC-FC correlation for the Latero cortical network module obtained by (Liska *et al.*, 2015). The correlation was computed at both the voxel level (left panel) and after aggregation in regions of interest (right panel). (C) SC-FC correlation for the hippocampal module obtained by (Liska *et al.*, 2015). The correlation was computed at both the voxel level (left panel) and after aggregation in regions of interest (right panel). Red dots: distance < 1mm, Blue: distance >= 1mm and < 2mm, Black dots: distance >=2mm.

Ascending modulatory nuclei are configured as between-network connector hubs

The observation of tightly overlapping structural and functional communities prompted us to investigate the topological structure and anatomical location of network nodes configured as *connector hubs*. These are nodal components critically configured as key orchestrators of inter-modular communication, enabling the dynamic interaction of lower and higher order networks to control complex behavioral and cognitive functions (Gratton *et al.*, 2018).

We first located connector hubs irrespective of the directionality of the connections, and termed the identified connector nodes *global connectors* (Figure 14). We found global connector hubs to be mainly localized in midbrain, hypothalamic and medio-dorsal thalamic regions, with only a marginal cortical involvement limited to orbitofrontal and temporal association areas. Remarkably, midbrain connector hubs focally encompassed three major set of ascending neuromodulatory nuclei, namely the ventral tegmental area and substantia nigra (dopamine), dorsal raphe nuclei (serotonin) and a set of voxels encircling the locus coeruleus (norepinephrine). Accounting for the directionality of the connections revealed evidence of a negligible topological segregation for most of the identified connector nodes (Figure 14C). As observed with other hub subtypes, most connector hub nodes exhibited a significant sub-regional distribution with respect to a predefined high-resolution anatomical parcellation (Figure 11B). Moreover, anatomical mapping of connector hubs using a parcellated connectome failed to reveal the involvement of key neurotransmitter nuclei (e.g. VTA, raphe areas, and locus coeruleus), hence concealing a key topological attribute of the mouse connectome. Collectively, these results reveal that ascending modulatory system are strategically wired as connector regions. The robust topographical correspondence between functional and structural modules support a role for the identified connector hubs as strategic orchestrators of brain-wide network activity (Gordon *et al.*, 2018), a notion consistent with emerging evidence

pointing at a pivotal contribution of cathecolaminergic neurotransmission in modulating functional network activity and dynamics (Van den Brink *et al.*, 2016; van den Brink *et al.*, 2018).

Connector hubs are critical mediators of network communicability

Graph theory postulates a critical contribution of hub regions to network integrity and stability, a notion supported by computational modelling of the human brain connectome (Aerts *et al.*, 2016). These properties support a theoretical framework in which hub regions serve as putative points of vulnerability for network disruption in the mammalian connectome (van den Heuvel & Sporns, 2013). To test whether these assumptions hold for the voxel-wise mouse connectome, we performed a series of targeted in silico nodal attacks and assessed how these virtual lesions affect the ensuing network properties (Figure 16). The effect of hub (or random node) removal was assessed using two well-characterized global network attributes: (i) the size of the *giant component*, i.e. the largest subgraph in the network, a proxy for the network's integrity (Aerts *et al.*, 2016) and (ii) global network efficiency, a measure of the ability of a network to efficiently route information (Rubinov & Sporns, 2010). This latter attribute is a measure of integration closely related to characteristic path length, based on the intuition that short path lengths in a network will facilitate rapid and efficient communication. A globally efficient network is therefore a network in which information can be efficiently routed in a cost-effective way. Interestingly, targeted removal of sources and out-connector hub nodes did not produce appreciably larger network fragmentation than observed with random nodal attacks (Figure 16). Similarly, the removal of central nodes had an overall marginal impact in decreasing network efficiency, producing a fragmentation that was on average only ~1.5% greater than random node removal ($p<0.01$, Figure 16). These results are line with previous observations suggesting that, independent of its sampling resolution (Figure 17A), the topological

structure of the mouse connectome does not recapitulate a canonical scale-free organization (Oh *et al.*, 2014; Henriksen *et al.*, 2016). They also support the notion that, irrespective of their classification and directionality, hub nodes of the voxel-wise connectome are not critical for the integrity and efficiency of brain network, making the mouse connectome highly resilient to targeted perturbations.

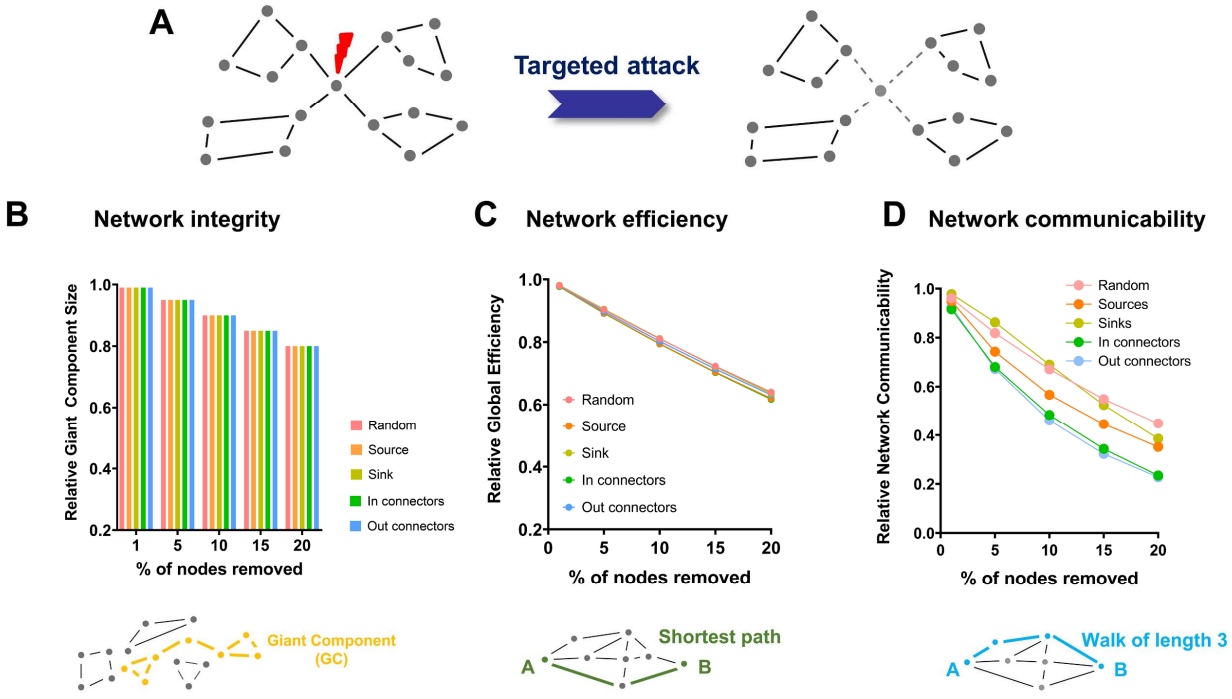

Figure 16. Connector hubs are critical effectors of network communicability. (**A**) Schematic illustration of targeted node removal and its effect on network integrity. (**B** to **D**) Effect of targeted hub removal on different network properties.

We therefore next probed whether hub regions could be key to a different communication mechanism other than the routing of information through shortest paths (i.e. as measured by network efficiency). To this purpose, we measured the effect of virtual hub lesioning using *total network communicability* (Benzi & Klymko, 2013; Avena-Koenigsberger *et al.*, 2018). This graph attribute measures the network's capacity for parallel information transfer, i.e. by taking into account the ability of information to disperse equally across all paths and walks in the network, i.e. not

necessarily and exclusively through the shortest paths. This property has therefore been equated to a measure of "bandwith" or "broadcasting capacity" (Benzi & Klymko, 2013) for information transfer within a network. Notably, we found that removal of connector hubs dramatically reduced network communicability with respect to random node deletion ($p<0.001$, Figure 16). Interestingly, a replication of virtual lesioning using a state-of-the-art parcellation (Oh *et al.*, 2014) produced similar results (Figure 17B), suggesting that the resiliency of the mouse connectome in terms of network integrity and efficiency, as well as its vulnerability in terms of network communicability, are resolution-invariant properties.

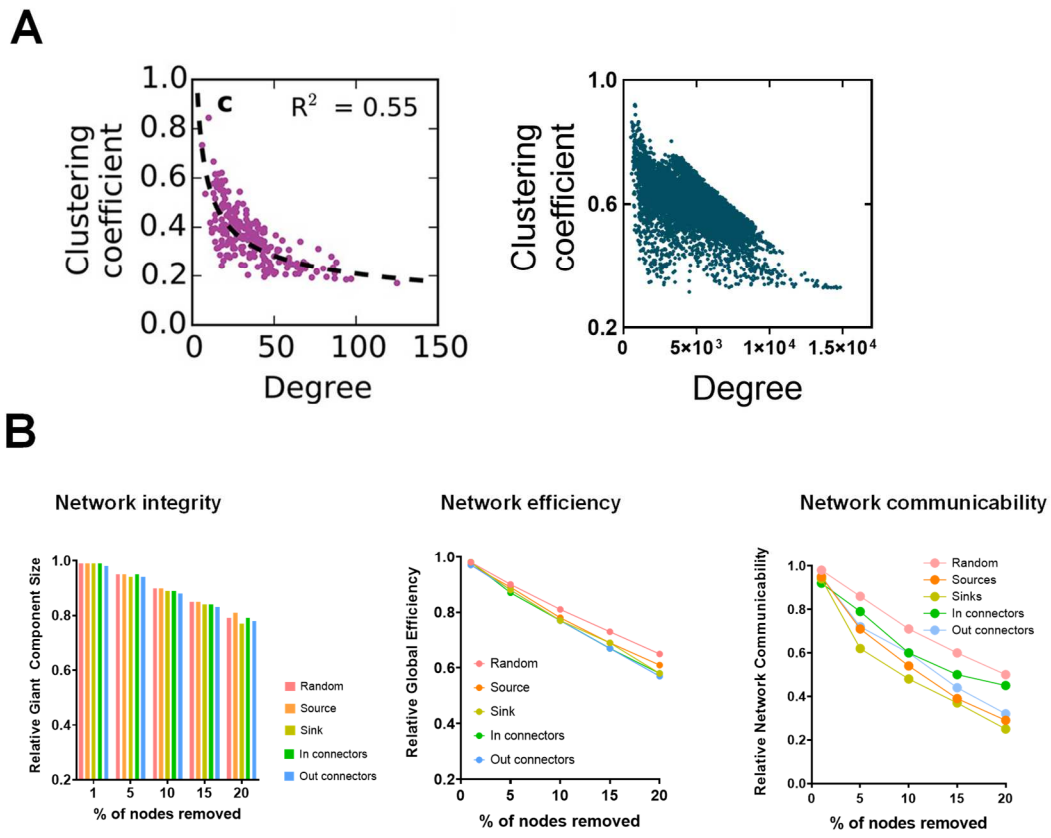

Figure 17. The mouse connectome does not exhibit a canonical scale-free architecture. (A) Clustering coefficient-degree joint distribution of the parcellated (left, modified from (Henriksen *et al.*, 2016), with permission) and voxel-wise mouse connectomes (right). These graphs suggest that both connectomes are similarly departing from a canonical scale

free topological organization. (B) Effect of targeted hub removal on different network properties using the parcellated connectome described in Oh et al., 2014.

Taken together, these findings suggest that connector hubs, and the neurotransmitter nuclei therein contained, besides acting as pivotal orchestrators or inter-modular communication, are also configured as key effectors of network communicability, enabling effective routing of information across regions via multiple parallel pathways.

The voxel-wise mouse connectome is organized along two superimposed cortical gradients

Recent functional and structural investigations in humans and primates have shown that the spatial arrangement of cortical connectivity reflects two superimposed gradients along which cortical locations are ordered according to their similarity in connections to the rest of the cortex (Margulies *et al.*, 2016). A first dominant cortical gradient is anchored in sensorimotor regions and radiates toward higher-order transmodal areas; a second gradient exhibits instead an axis of differentiation between sensorimotor modalities (Margulies *et al.*, 2016). Importantly, the organization of the unimodal-transmodal gradient is thought to define a hierarchy of increasing functional integration which guides the propagation of sensory inputs along multiple cortical relays into transmodal regions (Mesulam, 1998).

The fine-grained sampling of the voxel-wise connectome is ideally suited to probe the structural foundations of these organizational axes at an unprecedented spatial resolution. To this aim, we first probed whether a similar organization is phylogenetically conserved in rodents. We therefore applied diffusion map embedding (Margulies *et al.*, 2016) to the directed cortical connectome (Figure 18). To account for the directional encoding of the connectome, the procedure was applied to a matrix mapping the connectional profile of each node, i.e. incorporating the information provided by both

incoming and outgoing connections. Notably, we found that the structural connectome exhibits two spatial gradients of connectivity broadly recapitulating organizational principles observed in primates. Specifically, a dominant gradient (gradient A) involved a sensory-fugal transition between unimodal motor-sensory regions of the mouse LCN and transmodal components of the mouse DMN (Figure 18A). A second gradient (Gradient B) extended across unimodal visual and auditory cortices up to primary motor sensory regions, hence providing a regional differentiation between sensorimotor modalities. The spatial topography of cortical gradients appeared to be seemingly preserved when computed using a state-of-the-art parcellation (Figure 13G). However, resolution-dependent discrepancies in the topology of gradient B were apparent when a parcellation scheme was used, encompassing an atypical involvement of associative areas that departs from the modality-specific structure of analogous cortical gradients in higher mammals (Figure 13).

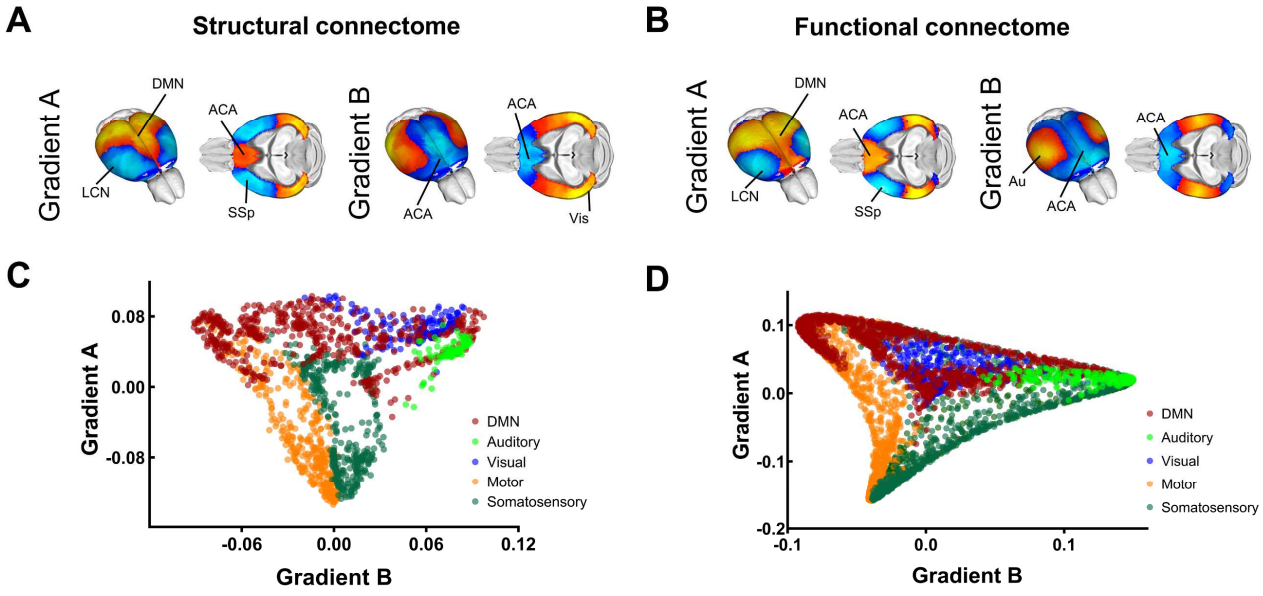

Figure 18. Gradients of SC and FC in the mouse cortex exhibit comparable topology. Structural (**A**) and functional (**B**) gradients of cortical organization in the mouse connectome. Gradient A encompasses a unimodal-polymodal spectrum of cortical regions extending from motor-sensory LCN (light blue/blue) to the DMN (yellow/red). Gradient B extends antero-posteriorly across primary sensorimotor (yellow) and transmodal associative regions (blue). (**C** and **D**) Regional scatter plots of gradient organization for

SC (C) and FC (D). ACA, anterior cingulate area; Au, auditory area; DMN, default mode network; LCN, latero-cortical network; SSp, primary somatosensory area; Vis, Visual areas.

Gradients of structural and functional connectivity in the mouse cortex exhibit comparable topology

The close topographical overlap between structural and functional communities observed in our modular analyses prompted us to probe the presence of a similarly tight relationship between anatomical and rsfMRI gradient organization in the mouse brain (Figure 18B and 19). To this aim, we mapped cortical gradients with voxel resolution in the mouse functional connectome. This analysis revealed that the functional connectome is organized into a unimodal-transmodal gradient (DMN-LCN, Gradient A) and a modality-specific gradient (Gradient B, Figure 18B) closely recapitulating key topographical features of the structural voxel-wise connectome (spatial correlation, Spearman's rho = 0.83, $p < 0.01$ for gradient A and rho = 0.60, $p < 0.05$ for gradient B, corrected for spatial autocorrelation). An anatomical classification of the regional constituents of the identified gradients revealed that the topographical organization of trans-modal and unimodal areas was broadly comparable across modalities (Figure 18C-D), although a small rearrangement in the spatial organization of modality-specific areas in functional gradient B was apparent, peaking in auditory-somatosensory regions as opposed to auditory-visual areas (Figure 18B and 19B).

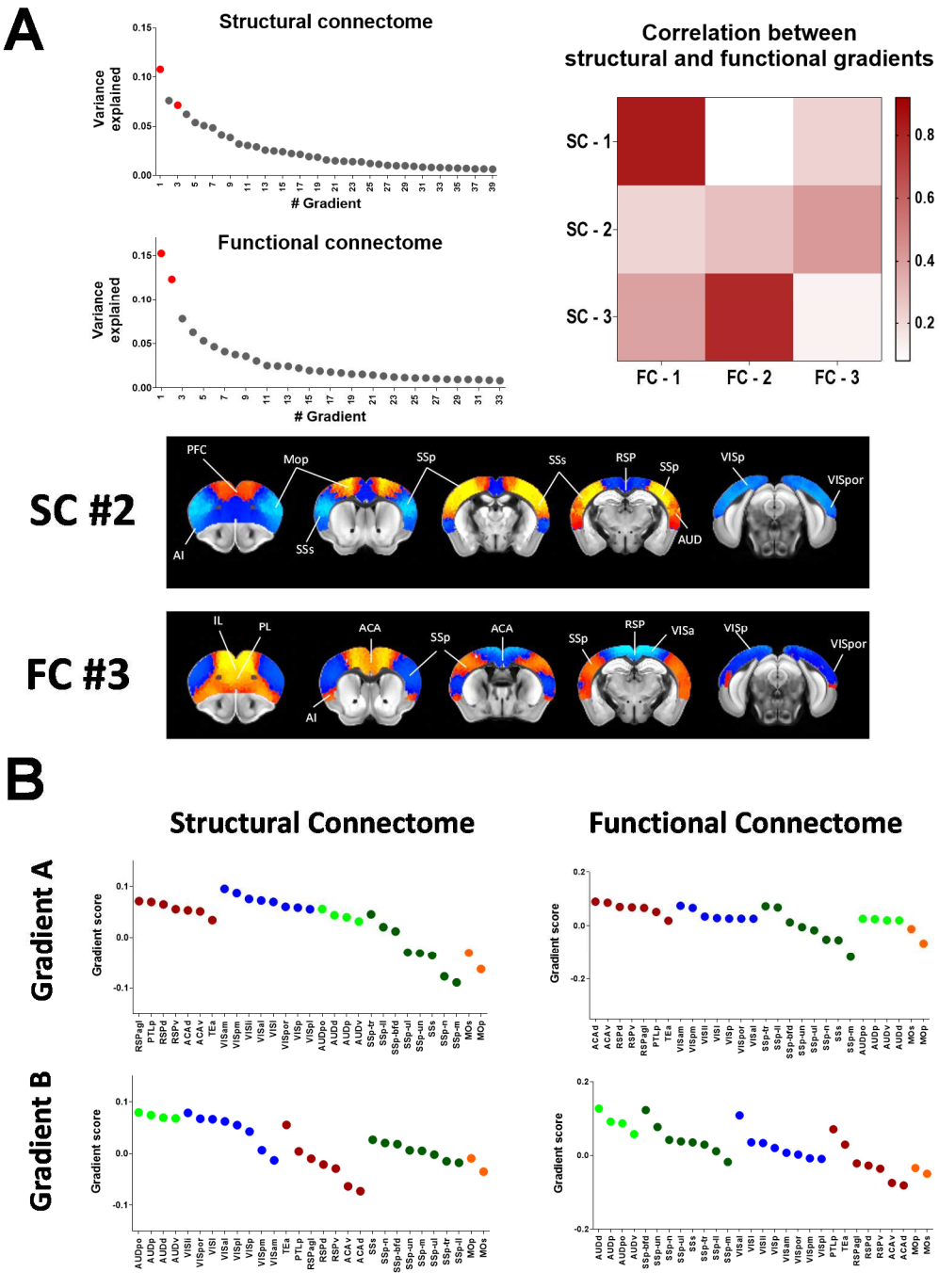

Figure 19. Identification and characterization of evolutionary-relevant structural and functional gradients. (A) Top left panel: Scree plot of explained variance for all the identified structural and functional gradients Red dots indicate the selected gradients. Top right panel: spatial correlation between first three functional and structural gradients (Spearman Rho – SC: structural gradients; FC: functional gradients). Bottom panels: anatomical representation of structural gradient #2 (SC #2) and functional gradient #3 (FC #3). (B) Cortical arrangement in the identified structural and functional gradients (see Table 2 for anatomical abbreviations).

Notwithstanding these modality-specific differences, unimodal vs. polymodal cortical arrangement in the functional and axonal connectomes appeared to be largely similar, pointing at a common hierarchical organization for the functional and structural mouse connectome. Taken together, these results reveal a robust structural foundation for cortical gradient organization in the mammalian cortex and show that the mouse brain connectome recapitulates phylogenetically conserved architectural principles observed in higher mammalian species.

Gradients of structural connectivity reflect cortico-cortical laminar hierarchy, and constrain fMRI network dynamics

Human studies have linked the organization of cortical gradients to hierarchical structure inferred from patterns of laminar cortical connectivity (Burt *et al.*, 2018). The recent description of a feedforward-feedback laminar hierarchy in cortical regions of the mouse brain (Harris *et al.*, 2019) allowed us to probe whether a similar organizational principle could explain the architectural organization of some of the gradients identified in the connectome. By computing the correlation between laminar hierarchy from Harris *et al.*, (2019) and structural gradient topography in a set of corresponding cortical regions, we found that the regional organization of the modality-specific gradient (Gradient B) was robustly correlated with intracortical laminar hierarchy (Figure 20A, Spearman's rho = 0.49, $p<0.01$ corrected for spatial autocorrelation), hence linking mouse cortical gradient (B) organization to patterns of laminar connectivity. Intralaminar cortical hierarchy was instead not predictive of unimodal-polymodal gradient (Gradient A) topography (Figure 20A, Spearman's rho = 0.17, $p=0.33$, corrected for spatial autocorrelation).

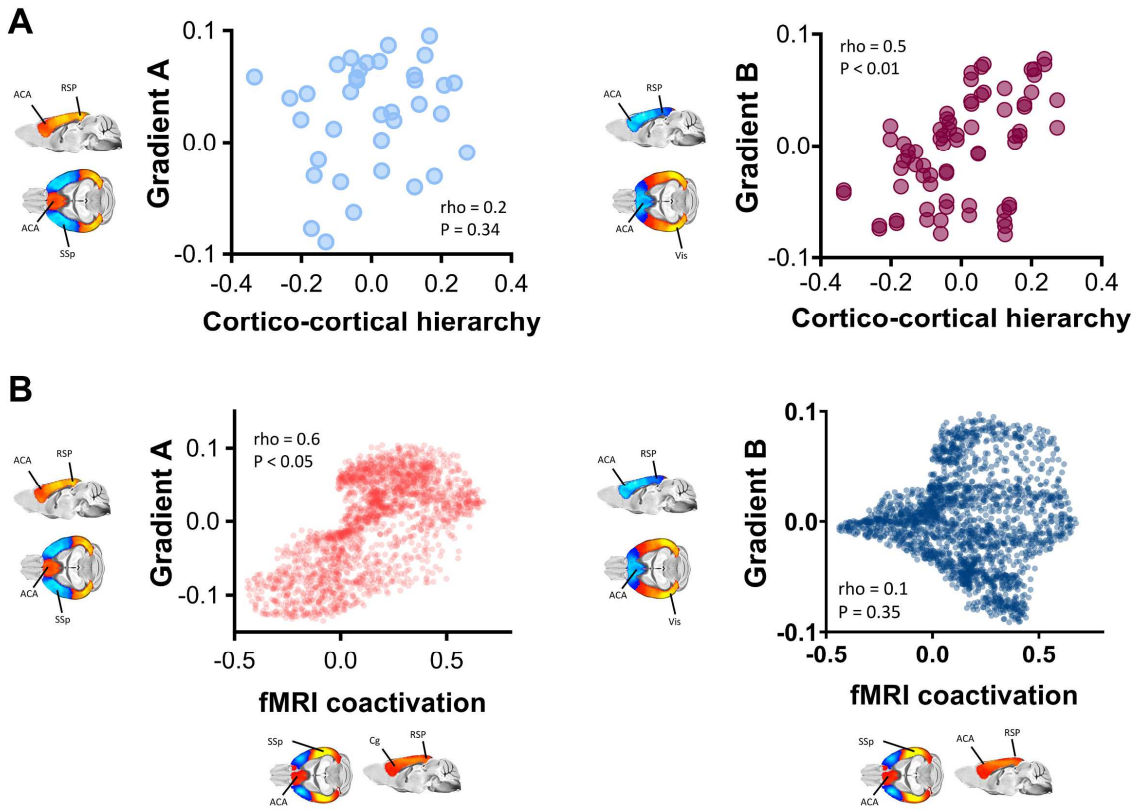

Figure 20. Gradients of SC reflect cortico-cortical laminar hierarchy and constrain fMRI network dynamics. (**A**) Modality-specific gradient B (right), but not polymodal-unimodal gradient A (left), reflects hierarchical intra-laminar organization of the mouse cortex. (**B**) Unimodal-polymodal DMN-LCN gradient A, but not modality-specific gradient B, closely recapitulates the spatial topography of dominant cortical CAPs governing fMRI dynamics in the mouse. ACA, anterior cingulate area; RSP, retrosplenial area; SSp, primary somatosensory area; Vis, Visual areas.

We finally noted that the anatomical organization of the unimodal-polymodal gradient A was anatomically consistent with the topography of dominant patterns of BOLD fMRI co-activation patterns (co-activation patterns - CAPs) recently described in the mouse (Gutierrez-Barragan *et al.*, 2019). CAPs serve as recurring "building-blocks" of spontaneous fMRI network dynamics, and are characterized by a distinct anatomical topography involving infraslow oscillatory transitions differentially affecting unimodal latero-cortical areas and midline poly-modal regions (Yousefi *et al.*, 2018; Gutierrez-Barragan *et al.*, 2019). The observation of a possible anatomical overlap between cortical gradient organization and dominant CAP topography may therefore explain the so far

unaccounted specific anatomical organization of these large-scale dynamic fluctuations (Gutierrez-Barragan *et al.*, 2019). In keeping with this notion, we found a strong spatial correspondence (Figure 20B, Spearman's rho=0.60 and p<0.05, corrected for spatial autocorrelation) between gradient A and dominant CAP topography. Conversely, the modal-specific gradient B did not show a significant relationship with the spatiotemporal structure of this dominant CAP (Figure 20B, right panel, Spearman's rho = 0.09 and p = 0.35, corrected for spatial autocorrelation). These results suggest that the hierarchical organisation of the cortical connectome may critically shape and constrain spontaneous patterns of fMRI network dynamics.

2.4 Discussion

Here we provide a fine-grained description of salient architectural motifs of the mouse connectome, without the imposed limits of discrete regional parcellations. Departing from regional-constrained studies, we find that hub regions and core network components of the voxel-wise mouse connectome exhibit a rich topography encompassing key cortical and subcortical relay regions. We also typify regional substrates based on their directional topology into sink or source regions, and report a previously unappreciated role of modulatory nuclei as critical effectors of inter-modular and network communicability. Finally, we demonstrate a close spatial correspondence between the mesoscale topography of the mouse connectome and its functional macroscale organization, and show that, like in primates and humans, the mouse cortical connectome is organized along two major topographical axes that can be linked to hierarchical patterns of laminar connectivity, and shape the topography of fMRI dynamic states, respectively.

Our regionally-unconstrained mapping of hub-like regions complements and expands prior investigation of the mouse connectome, providing a spatially precise identification of network

features and hierarchical motifs that may guide future manipulations of nodal properties in this species (Rubinov *et al.*, 2015). These include a fine-grained localization of hub-like properties in sub-regional components of large integrative areas, such as the dorso-lateral hippocampus or the central and basolateral amygdala, which were previously been considered as regionally homogeneous (Rubinov *et al.*, 2015). Similarly, our rich club mapping revealed a more detailed spatial topography than previously reported (Fulcher & Fornito, 2016), revealing two major organizational axes of high relevance for sensory-integration and higher cognitive functions, and which recapitulate organizational features observed also in non-mammalian species (Kunst *et al.*, 2019). Of note, perturbational studies support the biological relevance of our findings, as chemogenetic inactivation of the nucleus reuniens of the thalamus – a pivotal component of the mouse rich club – has been recently shown to impair hippocampal-dependent cognitive function in mice (Vetere *et al.*, 2017). These results suggest that subcortical relay stations are core components of nodal rich clubs across evolution, serving as critical integrators between top-down and bottom-up functional processing. Importantly, our analyses also show that hub-like network attributes in the voxel-wise mouse connectome are neuroanatomically segregable. This finding suggests that the network structure of the mammalian connectome is the result of converging evolutionary pressure, resulting in a regional organization in which spatially distinct hub-like regions delineate a hierarchy between higher order highly-interconnected associative regions, and bottom-up input from neuromodulatory areas configured as critical effectors of interregional communication.

Importantly, our results also revealed previously unappreciated organizational features of the mouse connectome that advance our understanding of the fundamental wiring principles of the mammalian brain in three main directions. First, the use of a high-resolution and directed connectome enabled us to segregate hub regions into *source* and *sink* areas. The ensuing

classification revealed the emergence of a global hierarchy in which higher order cortical areas and hippocampal regions serve as primary sources of neural input to the rest of the brain, and basal ganglia (plus focal mesencephalic nuclei) are wired as major receivers of distributed neural input. This hierarchical configuration follows a phylogenetic gradient in the arrangement of structural connectivity, and is optimally designed for the execution of rapid motor responses in response to salient external stimuli (Baldassarre *et al.*, 2013). Such a hierarchical configuration could also be expanded to non-hub regions via a brain-wide computation of the ratio of outgoing and incoming connectivity strength, defining a related organizational axis with motor-related nuclei, such as the cerebellum and basal ganglia, being located at its extremes. Of note, most of the network and topological attributes we describe in the present work appear to be resolution-specific (Figure 13), suggesting that prior topological mapping of the mouse connectome may have been biased by the coarser resolution of existing regional parcellations.

A second notable feature is our observation of a strategic configuration of ascending modulatory systems as connector hubs and essential effectors of network communicability. Previous investigations of the regionally-segregated mouse connectome have produced a largely cortico-centric description of connector hubs, involving cingulate, orbitofrontal and posterior association cortices, together with the basal ganglia and regionally undifferentiated midbrain regions (Rubinov *et al.*, 2015). Our results shift the focus from the cortex to subcortical relay stations, and document that ascending neurotransmitter systems are central to the mouse connectome and are configured as inter-modular connector hubs. Importantly, the observed spatial correspondences between the structural and functional topography of the mouse connectome argue for a critical role for these neuromodulatory nuclei in shaping large-scale neural activity. This notion is consistent with the observation that catecholaminergic and serotonergic activity critically control functional network

topography and dynamics (Giorgi *et al.*, 2017; van den Brink *et al.*, 2018). Together with the observation that connector hub removal critically diminishes network communicability, these results suggest that that ascending modulatory systems are strategically wired as central orchestrators of large-scale inter-modular communication, enabling the parallel routing of large chunks of information across the network. This network property might be key in ensuring the effective and finely-tuned control of complex behavioral and physiological states exerted by these systems. At the same time these properties might render these nodes key points of vulnerability for functional network disruption in brain disorder, a notion consistent with emerging evidence linking neuromodulatory dysfunction to neurodegenerative pathologies (Weinshenker, 2018). Interestingly, targeted removal of global hubs did only negligibly affect measurements of network integrity and efficiency when compared to random node deletion. This finding suggests that the mammalian connectome is structurally highly resilient, and argues against a role for this class of hub regions as critical mediators of network integrity in the mouse connectome. This result is partly supported by analogous investigations of the human connectome. For example, Crossley *et al.*, (2014) reported a linear decrease in global efficiency in a targeted attack for human structural networks, analogously to what we observed for the mouse connectome. Similarly, Alstott *et al.*, (2009) found functional network fragmentation to occur only when about 75% of the high strength nodes were removed. It should however be noted that other reports seem to be at odds with these results, suggesting a significant vulnerability of the human connectome against targeted attacks in human networks (see (Aerts *et al.*, 2016) for a recent overview on the topic). Whether these discrepancies reflect modality- and resolution-related discrepancies, or a lower proportion of long-range integrative fibers in rodents owing to evolutionary scaling of white/grey matter ratio (Mota *et al.*, 2019), remains to be established.

Finally, our voxel-wise description of two principal axes of cortical organization in the mouse connectome, and their topological linking with cortico-laminar organization and patterns of spontaneous fMRI dynamics, establishes a direct link between the mesoscale topography of the mouse connectome and its functional macroscale organization. These results suggest that the spatial arrangement of cortical areas along unimodal-polymodal and modality-specific gradients represents a general evolutionarily conserved principle governing the hierarchical organization of the mammalian cortex across evolution, and one that might intimately constrain the emergence and topology of spontaneous brain activity. This notion is consistent with a recent description of a cortical hierarchy in the parcellated mouse brain, as assessed by using an imaging marker of intracortical myelin content (Fulcher *et al.*, 2019). Our findings expand these prior observations by providing cross-modal and voxel-wise evidence of two superimposing functional and structural cortical gradients broadly recapitulating organizational principles observed in the human and primate brain. These include a hierarchical organization reflecting a well-characterized feedforward-feedback laminar hierarchy (Harris *et al.*, 2019), and a spectrum between unimodal regions and transmodal areas. It should be noted however that in the mouse the latter are known to exhibit a much lower degree of regional specialization than in primates, an observation that explains a categorization of latero-posterior visual and auditory territories as polymodal components of the posterior parietal cortex (Iurilli *et al.*, 2012; Meijer *et al.*, 2019). Importantly, our results also revealed that a dominant cortical gradient spatially shapes the emergence of prevailing patterns of cortical co-activation governing spontaneous fMRI dynamics, further relating the topography of the connectome with the structure and temporal evolution of spontaneous cortical activity (Gutierrez-Barragan *et al.*, 2019). The notion of a tight constraining effect of the structural connectome on functional network topography was further corroborated by evidence of largely overlapping functional and structural communities. This

finding expands prior investigations of the mouse functional connectome (Stafford *et al.*, 2014; Grandjean *et al.*, 2017), by highlighting a robust structural basis for distributed fMRI networks of the mouse brain such as the DMN and LCN. Such a close spatial overlap, however, does not appear to comprise hub topography, as previous voxel-wise mapping of functional hubs in the mouse only partly recapitulated the rich connectional features reported here (Liska *et al.*, 2015). Such incongruity might reflect the fact that the spontaneous fMRI signal is a neural mass phenomenon, reflecting local and remote contributions that are negligibly constrained by more fine-grained topological features of the structural connectome.

Multiple lines of future research that expand and complement our work can be envisaged. Rich club mapping was carried out here and in previous studies (Fulcher & Fornito, 2016) on the ipsilateral connectome to enable computational tractability. Further testing of rich club topography using a whole brain connectome may be warranted to corroborate the validity of these findings. Similarly, future network investigations using the full resolution, non-symmetrized connectome from (Knox *et al.*, 2019), may complement our work by revealing attributes especially sensitive to the microscale properties of the mouse connectome. Finally, future differentiations of the excitatory or inhibitory connectional output for each of the mapped network features via cell-type specific tracing could greatly expand the scope of our findings, especially for cerebellar and striatal areas characterized by high density of inhibitory populations.

In summary, here we provide a precise characterization of the network structure of the mouse connectome, with voxel resolution. Our results reveal a high-resolution structural scaffold linking mesoscale connectome topography to its macroscale functional organization, and create opportunities for identifying targets of interventions to modulate brain function and its network structure in a physiologically-accessible species.

Chapter 3 Probing the structure-function relationship in the mouse brain across scales and states

In the previous chapter we showed that the structural communities of the voxel-wise connectome recapitulate large-scale fMRI networks of the mouse brain. Moreover, we also showed that the spatial embedding of SC is tightly related to the spatial organization of both FC and CAPs, providing strong evidence for a close spatial correspondence between the mesoscale topography of the mouse connectome and its functional macroscale organization. However, how the structure-function relationship varies across different levels of brain organization and brain states, remains unclear. As discussed in the general introduction, human connectome research heavily relies on MRI derived connectome, measuring the mapping between brain structure and functions at the coarsest level, hence preventing fine-grained investigations of the relationship between these entities. These problems can be tackled in physiologically accessible species like the mouse, where state-of-the-art manipulations and computational models may converge, bearing great potential to advance our understanding of brain functioning, both theoretically and translationally (Gozzi & Schwarz, 2016). In the remainder of this chapter, I will briefly introduce the results of some ongoing and/or published collaborations, restricting the scope of the discussion to the analysis of the structure function relationship in the mouse brain. In the first section (Chapter 3.1) I will briefly describe the results of a recent study in collaboration with the Allen Brain Institute where we used layer specific tracing to uncover the wiring diagram of the mouse default network. In the second section (Chapter 3.2) we used our voxelwise connectome to probe how the functional reorganization of brain networks in awake mice leads to a configuration that departs from that of the underlying SC.

3.1 Cell-type-specific connectivity of the mouse default mode network

An extended version of the results depicted in this chapter has been published in: Whitesell, J. D., Liska, A., Coletta, L., Hirokawa, K. E., Bohn, P., Williford, A., ... & Harris, J. A. (2021). Regional, Layer, and Cell-Type-Specific Connectivity of the Mouse Default Mode Network. *Neuron*, 109(3), 545-559.

Since its serendipitous discovery, the DMN has been one of most investigated large-scale networks of the mammalian brain (Gozzi & Schwarz, 2016; Buckner & DiNicola, 2019). Of note, the DMN seems to be a fundamental "building block" of the brain's intrinsic architecture, whose salience in capturing essential features of brain (dys)organization seems to be preserved across animal species and modalities (Sforazzini *et al.*, 2014; Liska *et al.*, 2015; Margulies *et al.*, 2016; Bertero *et al.*, 2018; Buckner & DiNicola, 2019; Hong *et al.*, 2019; Coletta *et al.*, 2020). However, the coarse mapping provided by MRI-derived connectomes, and the correlational nature of the studies examining the structure-function relationship are limiting factors that prevent a fine-grained description of the structural basis of the DMN. A characterization of the DMN spanning multiple levels of brain organization is therefore of fundamental importance, given the translational relevance of this functional network. In Whitesell *et al.*, (2021) we set out to fill this gap, mapping the anatomical bases of the DMN with sublaminar precision (see Figure 21 for a simplified graphical representation of the experimental procedure).

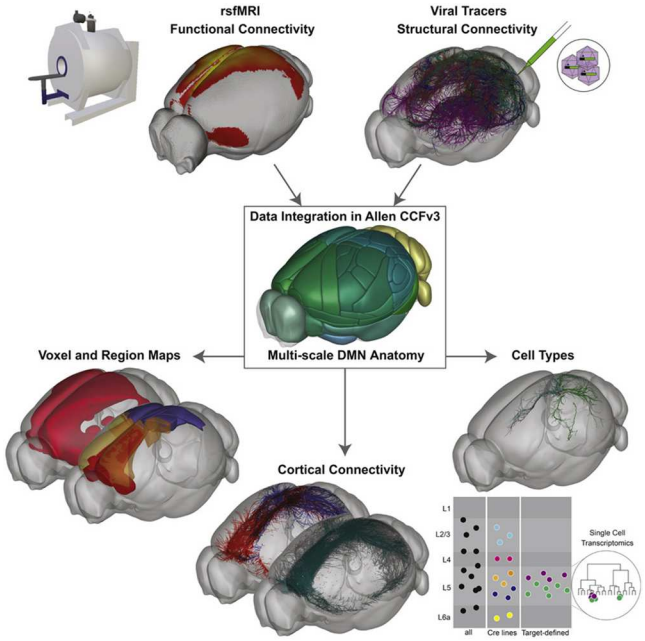

Figure 21. Schematic representation of the experimental procedure used for our multiscale default mode network characterization. Default mode network (DMN) definition was based on resting state fMRI functional connectivity (top left). Viral tracing experiments performed on an independent cohort of mice allowed to track structural connectivity at the level of single neurons (top right). Integrating both functional and structural connectivity maps into the common coordinate framework (version 3, CCFv3) of the Allen Brain Institute enabled to probe the multiscale organization of the DMN within the same reference system (middle box). Connectivity maps were analyzed at the voxel and regional levels (bottom left), revealing the existence of distinct structural cortical connectivity patterns with unique cell type specific signatures (bottom left).

To identify the DMN, we mapped mouse rsfMRI networks (recorded under light anesthesia, (Gutierrez-Barragan *et al.*, 2019)) via a low-dimensional group Independent Component Analysis (5 components estimated on 40 mice), corroborating the DMN definition with seed-based probing of the anterior cingulate cortex, a key cortical region of the mouse DMN. The independent component corresponding to the DMN was scaled to z scores, thresholded at Z = 1 and Z = 1.7 as per Sforazzini *et al.*, (2014) to obtain a DMN and a DMN-core mask (respectively), registered to the CCFv3 space, and finally overlaid with CCFv3 region boundaries to define the anatomical structures of the DMN. We used the core mask exclusively to define “in-DMN” and “out-DMN” brain regions, all subsequent analysis were performed with the Z=1 mask. Within this framework, a brain region was said to belong

to the DMN if more than 50% of its voxel were in the core mask. As expected, and in line with previous findings, the quantification revealed that most (77.6 and 89.6 % for Z=1 and Z=1.7, respectively) of the voxels in the DMN belonged to the prefrontal and medial regions of isocortex. A focal involvement of the mediodorsal thalamus and the dorsal striatum was also apparent. However, regions outside the isocortex did not survive the strict criterion for DMN inclusion at the regional level and were therefore labelled as not belonging to the DMN.

A quantitative analysis performed on a dedicated set of 300 viral injections experiments across the isocortex (Figure 22A) revealed that DMN regions preferentially project to other DMN regions (Figure 22B), even after accounting for distance. These findings provide empirical evidence that the DMN is indeed a prominent structural community of the mouse brain, experimentally corroborating the results of Coletta *et al.*, (2020), who showed its existence with a pure data driven procedure. Intriguingly, we also found that DMN exhibited a higher fraction of outgoing connections than the networks, once again highlighting its integrative role.

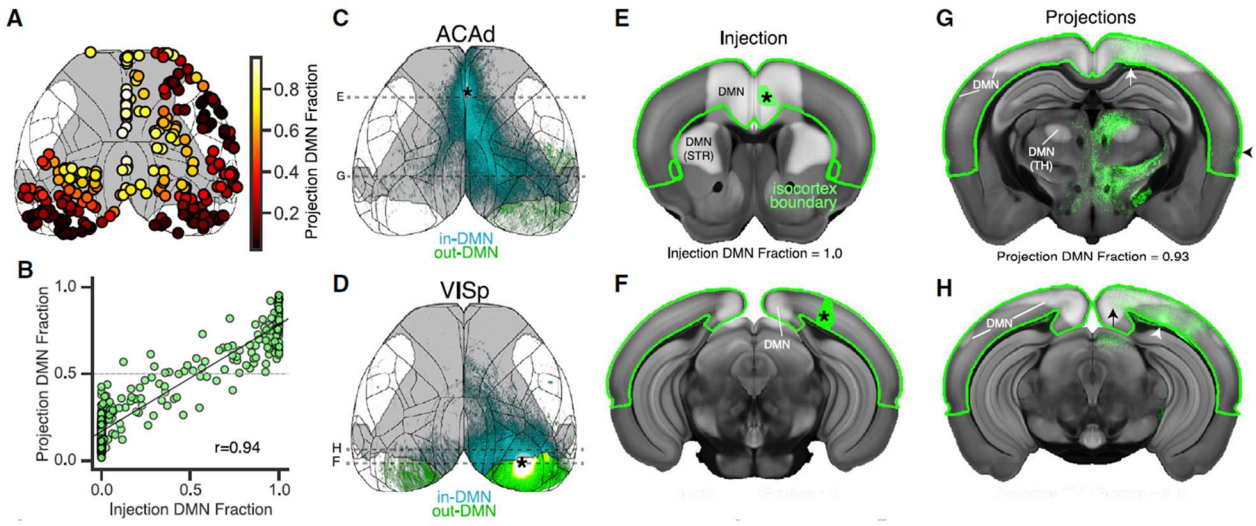

Figure 22. DMN Regions Preferentially Project to Other DMN Regions. (A) Top-down view of the cortical surface showing the spatial distribution of the 300 tracing experiments used to quantify fraction of DMN projections (shown by colormap). Gray, DMN mask; black, region boundaries. (B) Projection DMN fraction as a function of the injection DMN fraction for the experiments in (A).

r, Pearson correlation. (C and D) Cortical projection images showing axons arising from an experiment inside (C, dorsal anterior cingulate cortex) and outside of (D, primary visual cortex, VISp) the DMN mask. Asterisks indicate the approximate injection centroid. Cyan, in-DMN projections; green, out-DMN projections. (E–H) Virtual sections of the CCFv3 template overlaid with aligned experiment data at (E and F) the center of each injection site (green pixels with asterisks; E, ACAd; F, VISp) and (G and H) target areas with high axon projection densities (green pixels). Arrows, in-DMN projections; arrowheads, cortical projections outside of the DMN; green edges, isocortex boundary; white overlay, DMN mask; portions overlapping the striatum (STR) and thalamus (TH) are also labeled. [DMN: default mode network].

Prompted by the observation that a non-negligible fraction of "in-DMN" regions project outside the DMN, we next examined the structural connectivity of the DMN at the laminar level (350 viral injections experiments, 14 different cre lines). Of note, we found that layer 2/3 DMN neurons project mostly in the DMN, whereas layer 5 neurons project both in and out. Further analysis (and dedicated tracing experiments) revealed the presence of separate in-DMN and out-DMN-projecting cell types in postero-medial regions of the DMN, especially in the ventral retrosplenial cortex, where we identified a midline DMN projecting pattern and a visual projecting pattern. The two clusters also exhibited significant differences in their genetic profile; we found midline-projecting cells having higher expression of the *Arc* and *Gne* genes. A cross-comparison with the *in situ* hybridization (ISH) data of the Allen Mouse Brain Atlas revealed that *Arc* expression appears to be stronger in the superficial part of L5, where the midline-projecting cells are found, further corroborating the robustness of the finding. This result is important as it paves the way to the genetic targeting of DMN-specific neurons for future manipulation studies.

Taken together, our results provide one of the most advanced characterizations of a mammal functional network to date. In good agreement with previous investigations (Stafford *et al.*, 2014; Coletta *et al.*, 2020), we found that the mouse DMN is predominantly composed of preferentially-interconnected isocortical regions. The (sub)laminar specificity of viral tracing experiments allowed us to disentangle layer-specific patterns of DMN connectivity, and to link them to specific genetic

profiles defining a novel class of network-specific cells. Our results also highlight the translational potential of structural and functional connectomics in the mouse along two main directions. First, the establishment of layer specific connectivity patters allows to generate new testable predictions about the anatomical basis of a phylogenetically conserved functional network. Second, the differential gene analyses revealed two potential marker genes for the midline-projection types, namely *Arc* and *Gne*, whose combination can define a genetically targetable subclass of neurons. Of note, both genes have recently associated with neurodevelopmental conditions (schizophrenia and autism spectrum disorders, respectively (Managò & Papaleo, 2017; Yang *et al.*, 2020)), endowing our findings of potential translational relevance for the study of brain functional connectopathy.

3.2 Functional network organization departs form underlying axonal structure in the awake mouse brain

An extended version of this chapter has been accepted for publication in *Current Biology*, and is currently available as: Singh, N. A., Gutierrez-Barragan, D., Alvino, F., Coletta, L., Rocchi, F., De Guzman, E. A., ... & Gozzi, A. (2022). Unique spatiotemporal fMRI dynamics in the awake mouse brain. Current Biology, in press

Besides the multiscale characterization of functional circuits, understanding the brain's organization across different physiological states and how these relate to the underlying structural scaffold is of primary interest. In humans and primates, great effort has been dedicated to understanding how macroscale functional networks reconfigure during the transition from deep anesthesia to wakeful conditions, as the ensuing reconfiguration can be used as a putative signatures of consciousness (Barttfeld *et al.*, 2015; Demertzi *et al.*, 2019; Huang *et al.*, 2020). Specifically,

influential primate and human studies have reported that loss of consciousness in these species results in a partial reorganization of long-range functional connectivity, disappearance of anticorrelated cortical states and a repertoire of dynamic states dominated by rigid functional configurations tied to the underlying anatomical connectivity (Barttfeld *et al.*, 2015; Demertzi *et al.*, 2019; Huang *et al.*, 2020). By contrast, conscious wakefulness has been associated with greater global integration and inter-areal cross-talk, anticorrelation between the activity of different brain regions, and a more flexible repertoire of functional brain configurations departing from anatomical constraints (Barttfeld *et al.*, 2015; Demertzi *et al.*, 2019; Huang *et al.*, 2020). Whether similar spatiotemporal organizational principles apply to the mouse brain is still unknow, as awake imaging is notoriously difficult to perform in this species (Grandjean *et al.*, 2020).

Leveraging a novel, robust protocol for rsfMRI in awake head-fixed mice, we recently provided a fine-grained comparison of the functional topography and dynamic structure of rsfMRI networks between wakeful and anesthetized animals, relating the two conditions to the underlying structural connectivity.

To map the functional organization of rsfMRI networks in awake conditions, we systematically probed rsfMRI connectivity networks via seed-based correlation mapping (Figure 23A, left panel). This analysis revealed robust interhemispheric and antero-posterior rsfMRI synchronization, including the presence of distributed networks anatomically recapitulating rsfMRI systems previously described in lightly anesthetized mice, such as the DMN, LCN, a salience (insular-cingulate) network, a visual-auditory latero-posterior network (LPN), plus a number of subcortical sub-systems, including dorsal (caudate-putamen) and ventrostriatal networks (mesolimbic pathway); a dorsal hippocampal network and a widely-distributed olfactory and amygdaloid network. A comparison with age-matched anesthetized mice (two different anesthetic regimens, halothane and isoflurane-medetomidine,

respectively) revealed a set of focal state-dependent differences in the extension and anatomical organization of rsfMRI connectivity networks (Figure 23A, right panel and 23B). First, we found that rsfMRI networks in awake animals exhibited robust functional anti-coordination between some of the probed regions and their long-range substrates. Anti-coordination was especially prominent between medial prefrontal cortex (PFC) and olfactory regions, as well as between visual-auditory areas and midline regions of the DMN. The observed anti-correlation was accompanied by a reduced spatial extension of the DMN in awake mice, where a clear segregation of midline corticolimbic and visuo-auditory postero-lateral portions of the DMN was apparent. Moreover, in awake mice ventral forebrain area (e.g. diagonal band, hypothalamus, nucleus accumbens) were part of an extended highly-synchronous network that exhibited only marginal functional coupling in anesthetized subjects. More nuanced network-specific differences in rsfMRI connectivity strength were also apparent, with evidence of reduced cortico-cortical coupling in the DMN and LCN, and stronger connectivity in visual-auditory and basal forebrain areas in awake versus anesthetized animals.

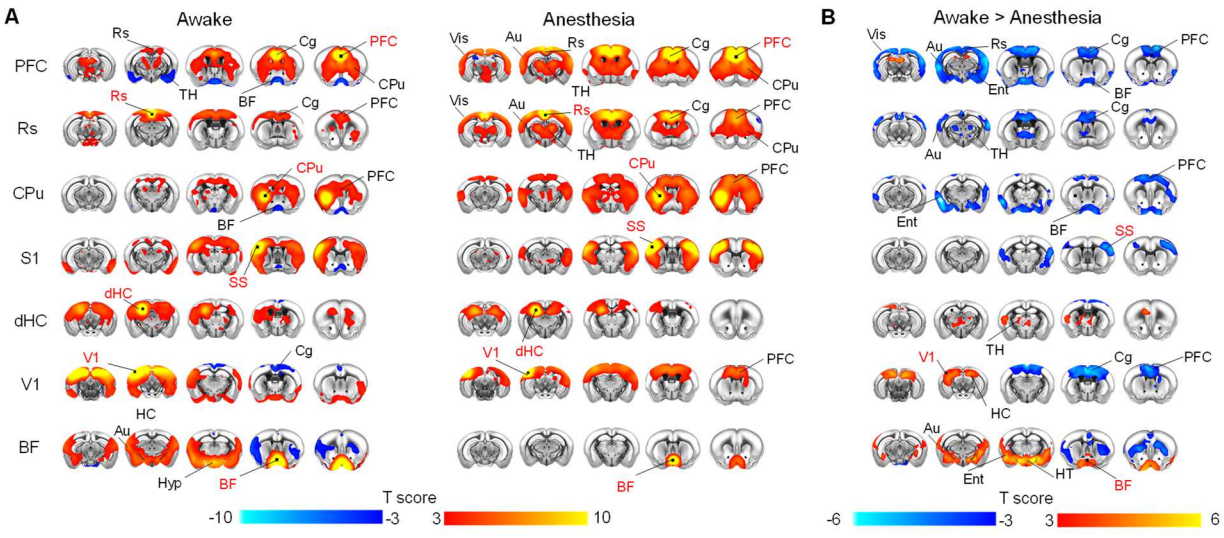

Figure 23. rsfMRI network topography in the awake and anesthetized mouse brain. A) Group averaged seed-based correlation maps in awake (N = 10, left) and halothane anesthetized (N = 19, right) mice, thresholded to voxels with significant connectivity (one sample T-test, $p < 0.01$, cluster corrected with defining threshold T = 2.8). B) Between group connectivity differences (two-sample T-

test, $p < 0.01$, FWER corrected with defining threshold T=2.8). [DMN: Default mode network, LCN: Latero-cortical network, HC: Hippocampal network, OF-BF: olfactory-Basal forebrain network, PFC: Prefrontal cortex, Cg: Cingulate cortex, Rs: Retrosplenial cortex, TH: thalamus, CPu: Caudate putamen, Ins: Insula, dHC: dorsal Hippocampus, Ent: Entorhinal cortex, Au: Auditory cortex, M1: Primary Motor, SS: Somatosensory cortex, V1: Visual, BF: Basal forebrain, Amy; Amygdala, NAc: Nucleus Accumbens, HT: Hypothalamus].

The observation of areas of negative correlation in the awake mouse brain is of great interest, as similar findings have been suggested to serve as a putative signature of fMRI network activity in conscious states in other mammalian species such as marmosets, macaques, and human (Barttfeld *et al.*, 2015; Demertzi *et al.*, 2019; Esfahlani *et al.*, 2020; Hori *et al.*, 2020). Importantly, these reports also showed that network configuration in anesthetized and wakeful animals may be characterized by different anatomical organization, with the unconscious state being more tied to the anatomical map, and awake brain networks exhibiting a topographical departure from their underlying anatomical architecture. To investigate whether similar principles would apply to the mouse brain, we used a graph theoretical approach to probe the relationship between the structural and functional connectome in wakeful and anesthetized animals. To this aim, we leveraged the anatomical partition of the voxel-wise mouse axonal connectome into four macro-communities that spatially reconstitute macroscopic network systems of the mouse brain, i.e. the DMN, the LCN, the hippocampus and olfactory-basal forebrain areas ((Coletta *et al.*, 2020), chapter 2). A graphic representation of the functional connectome with respect to these axonal communities (Figure 24A) revealed that, departing from the modular partitioning of the axonal connectome, fMRI networks in awake subjects exhibit greater inter-areal communication than corresponding anesthetized state. In keeping with this notion, structure-function correspondence was significantly lower in awake animals compared to anesthetized subjects ($p<0.01$, Mann-Whitney test, Figure 24B). Formal quantifications of rsfMRI network connectivity strength corroborated these qualitative observations (Figure 24C), revealing

dramatically increased between-network connectivity in awake mice, a finding that was especially prominent between basal forebrain and cortico-hippocampal areas ($p < 0.01$, Mann-Whitney test, FDR corrected). Furthermore, and corroborating seed based correlational mapping, arousal-related basal forebrain regions also showed significant increased within-network connectivity strength. Importantly, analogous features were observed when we contrasted awake rsfMRI data with those obtained in isoflurane-medetomidine anesthetized animals, hence supporting a possible generalization of this finding to other anesthetic regimens. These findings recapitulate prior observations in conscious primates, suggesting that, departing from the underlying structure of the axonal connectome, rsfMRI network activity in conscious mice topologically reconfigures to maximize cross-talk between cortical and arousal-related subcortical systems.

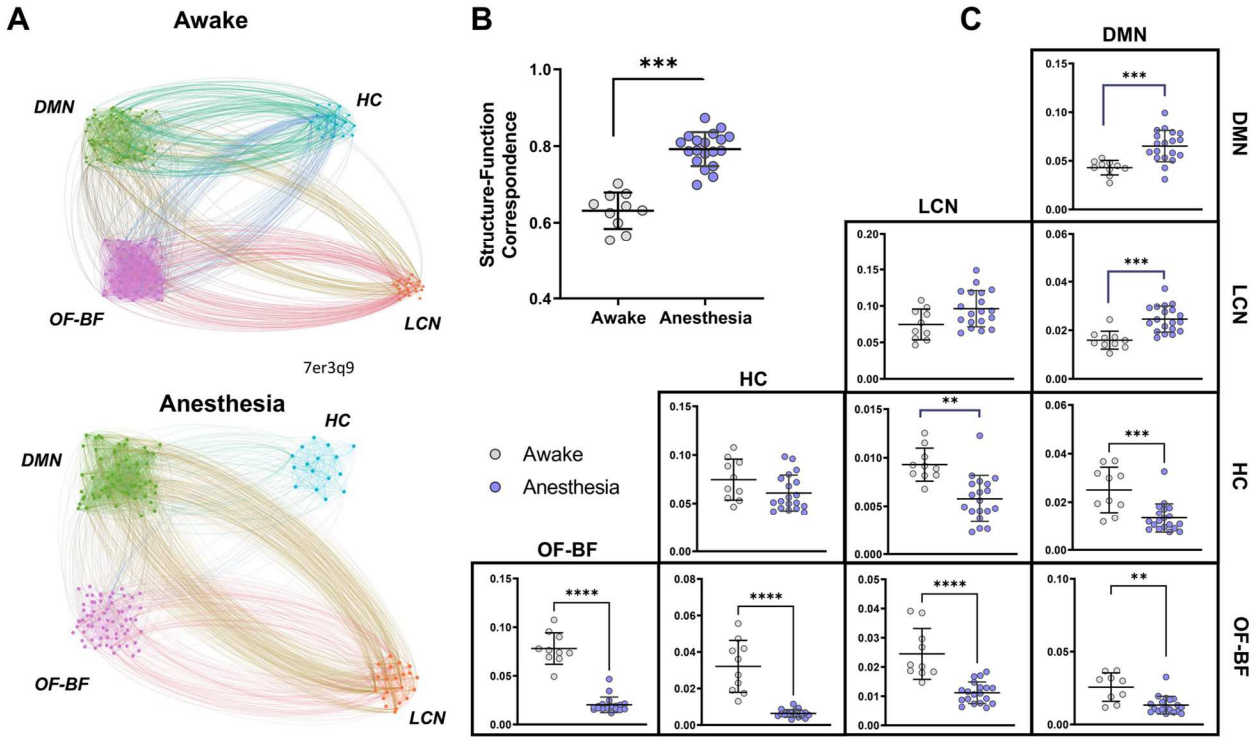

Figure 24. **Structure-function relationship in awake and anesthetized states. A)** Graphic representation of rsfMRI connectivity within and between previously described axonal modules of the mouse brain (DMN, LCN, HC, OF-BF, from Coletta et al., 2020). Each

cluster of nodes represents a subset of anatomically-defined ROIs within the corresponding module. Nodes have been empirically arranged to maximize figure legibility. **B)** Structure-function correspondence in awake (N = 10) and halothane anesthetized mice (N = 19). Between-group differences were assessed with a Mann-Whitney test ($p < 0.05$). **C)** Quantification of within (diagonal) and between (off-diagonal) network functional connectivity (*p<0.05, ** p<0.01, *** p<0.001, **** p<0.0001, Mann-Whitney test, FDR corrected). [DMN: Default mode network, HC: Hippocampus, OF-BF: Olfactory and basal forebrain, LCN: latero-cortical network].

Prompted by the identification of dynamic connectivity signatures of consciousness in primates and human, we hypothesized that the observed time-averaged network changes could similarly reflect state-dependent differences in the underlying dynamic structure of rsfMRI. In keeping with our observations using "static", steady-state measurements of connectivity, a decomposition of rsfMRI activity into recurring CAPs revealed a largely dominant occurrence of brain states encompassing arousal-related forebrain nuclei in wakeful animals. Modelling CAPs timeseries as a Markov process highlighted the engagement of basal forebrain areas and the presence of anti-coordination between DMN and visual regions as a distinctive trait differentiating between awake and anesthesia, further recapitulating dynamic fMRI features recently described to be predictive of consciousness in higher mammalian species (Barttfeld *et al.*, 2015; Demertzi *et al.*, 2019). Taken together, these results suggest that the spatiotemporal structure of rsfMRI activity in the awake rodent brain recapitulates evolutionarily-relevant principles predictive of conscious states in higher mammalian species. We speculate these dynamics features represent a species-invariant signature of consciousness in the mammalian brain.

Chapter 4 Conclusions

The research presented in this thesis focused on providing a precise characterization of the network structure of the mouse structural connectome, unconstrained by regional partitioning (chapter 2). Our results show that the mouse connectome is characterized by a finer network topography than previously reported. Going beyond a canonical network characterization in terms of hubs and communities, we showed that the topological rules governing the network's architecture broadly recapitulates basic organizational principles of the human and non-human primate brain, creating opportunities for identifying targets of interventions to modulate brain function and its network structure in a physiologically-accessible species Of note, we also found a tight inter-dependence between functional and structural brain organization, linking mesoscale connectome topography to its macroscale functional organization. Macroscale structure-function correspondence was analyzed more in-depth for the mouse DMN, providing one of the most advanced characterizations of a mammalian macroscale network available to date, and to characterize the transition from anesthesia to wakeful states. We found that awake fMRI networks in the mouse exhibit a topographical departure from their underlying anatomical architecture, recapitulating a dominant functional configuration that has been associated with conscious conditions in other species. This finding is also consistent with the postulates of prevailing theories of consciousness, according to which functional networks that support awake, conscious states exhibit global integration.

4.1 Limitations & Future Directions

Some technical limitations in the approach employed here should be mentioned. These pertain both the use of rsfMRI and the axonal connectome. Regarding the latter resource, despite being the current gold standard for measuring SC, tract tracing derived monosynaptic connectomes do not allow a direct and whole brain modeling of polysynaptic connectivity, posing hard constraints on the modeling and interpretability of the structure-function relationship (Avena-Koenigsberger *et al.*, 2018). Several network models describing how communication unfolds on the structural connectome have been proposed, and yet determining which one is best suited to describe the dynamics of large-scale brain networks remains an open and central question (Avena-Koenigsberger *et al.*, 2018; Graham *et al.*, 2020). Recent investigations have begun to tackle this aspect (Seguin *et al.*, 2019, 2020). For example, Seguin *et al.*, (2019) were able to infer the directionality of communication flow from an undirected structural connectome by exploiting asymmetries in the pairwise interactions across brain regions, while Seguin *et al.*, (2020) probed the efficacy of different communication models in predicting behavior and FC. Although the results of these preliminary investigation are promising, more work addressing these limitations is needed, for example by comparing different communication models across species, and by generating testable hypothesis about brain function, e.g. via perturbational approaches.

Despite its non-invasiveness, whole-brain coverage, and the translatability from rodents to human, the use of (rs)fMRI to map brain function is associated with at least three notable drawbacks (Lake *et al.*, 2020). First and foremost, fMRI is an indirect measure of neural activity, as it critically relies on the BOLD contrast mechanism. Furthermore, the hemodynamic response at the basis of the BOLD contrast unfolds on the scale of seconds, severely limiting the temporal resolution offered by this imaging method. Lastly, rsfMRI cannot resolve the (indirect) measurement of neural activity with

cellular resolution, limiting its mapping at macroscale level. The use of rsfMRI as a proxy for neural activity should therefore exercised with caution, as the resulting macroscale reorganization maught not be reflective of direct neural interactions. This notion is epitomized by manipulation studies showing that the sign and extension of rsfMRI coupling does not monotonically reflect underlying neural activity (Rocchi *et al.*, 2022, in press). Simultaneous fMRI and wide-field mesoscopic calcium imaging recordings in animal models (Lake *et al.*, 2020) may help disambiguate the cascade linking neural activity to hemodynamic signals. One key strength of this experimental approach is the opportunity to measure the relative contributions of different cell types to the BOLD signal, paving the way toward a better understanding of its physiological basis and significance (Cardin *et al.*, 2020; Lake *et al.*, 2020). Similarly, measuring neural activity across a range of spatiotemporal scales via increasingly available multielectrode recordings may allow for a more nuanced modeling of the structure-function relationship. An example of the power of this approach has been recently demonstrated by Vezoli *et al.*, (2021) by means of invasive electrocorticography in macaque monkeys (Vezoli *et al.*, 2021). These authors showed that different brain rhythms are differentially associated to the underlying axonal connectivity, with the gamma rhythm exhibiting the strongest correlation, and beta rhythm the weakest. Based on these results, the authors proposed that subcortical structures may mediate the emergence of the beta rhythm in cortico-cortical circuits, via a polysynaptic circuit. The extension of these measurements to model organism and their combined used with manipulation techniques may help further disambiguate the complex relationship between functional and structural macroscale organization across evolution, ultimately advancing our understanding of the structural basis of brain activity.

Tables

Table 1. Regional parcellation

ABBR.	NAME	Macro	# voxels bilateral	# voxel right	# voxel left
FRP	Frontal Pole	Isocortex	966	483	483
MOp	Primary motor area	Isocortex	11376	5718	5658
MOs	Secondary motor area	Isocortex	13096	6552	6544
SSp-n	Primary somatosensory area, nose	Isocortex	3032	1520	1512
SSp-bfd	Primary somatosensory area, barrel field	Isocortex	6281	3137	3144
SSp-ll	Primary somatosensory area, lower limb	Isocortex	2361	1178	1183
SSp-m	Primary somatosensory area, mouth	Isocortex	6224	3115	3109
SSp-ul	Primary somatosensory area, upper limb	Isocortex	3764	1878	1886
SSp-tr	Primary somatosensory area, trunk	Isocortex	1399	703	696
SSp-un	Primary somatosensory area, unassigned	Isocortex	1263	633	630
SSs	Supplemental somatosensory area	Isocortex	8993	4504	4489
GU	Gustatory areas	Isocortex	1760	883	877
VISC	Visceral area	Isocortex	2370	1184	1186
AUDd	Dorsal auditory area	Isocortex	1213	609	604
AUDp	Primary auditory area	Isocortex	2152	1079	1073
AUDpo	Posterior auditory area	Isocortex	598	300	298
AUDv	Ventral auditory area	Isocortex	1807	904	903
VISal	Anterolateral visual area	Isocortex	768	391	377
VISam	Anteromedial visual area	Isocortex	775	386	389

VISl	Lateral visual area	Isocortex	1237	618	619
VISp	Primary visual area	Isocortex	7113	3565	3548
VISpl	Posterolateral visual area	Isocortex	792	399	393
VISpm	posteromedial visual area	Isocortex	1043	520	523
VISli	Laterointermediate area	Isocortex	492	243	249
VISpor	Postrhinal area	Isocortex	1269	638	631
ACAd	Anterior cingulate area, dorsal part	Isocortex	3114	1479	1635
ACAv	Anterior cingulate area, ventral part	Isocortex	2387	1128	1259
PL	Prelimbic area	Isocortex	2433	1159	1274
ILA	Infralimbic area	Isocortex	849	403	446
ORB	Orbital area	Isocortex	5886	2907	2979
AId	Agranular insular area, dorsal part	Isocortex	3726	1867	1859
AIp	Agranular insular area, posterior part	Isocortex	2429	1211	1218
AIv	Agranular insular area, ventral part	Isocortex	1737	873	864
RSPagl	Retrosplenial area, lateral agranular part	Isocortex	2308	1162	1146
RSPd	Retrosplenial area, dorsal part	Isocortex	3816	1899	1917
RSPv	Retrosplenial area, ventral part	Isocortex	4331	2090	2241
PTLp	Posterior parietal association areas	Isocortex	2454	1232	1222
TEa	Temporal association areas	Isocortex	3106	1549	1557
PERI	Perirhinal area	Isocortex	797	398	399
ECT	Ectorhinal area	Isocortex	1728	870	858
MOB	Main olfactory bulb	Olfactory Areas	16406	8218	8188
AOB	Accessory olfactory bulb	Olfactory Areas	650	325	325
AON	Anterior olfactory nucleus	Olfactory Areas	4880	2437	2443
TT	Taenia tecta	Olfactory Areas	1431	690	741
DP	Dorsal peduncular area	Olfactory Areas	482	232	250
PIR	Piriform area	Olfactory Areas	11591	5793	5798

NLOT	Nucleus of the lateral olfactory tract	Olfactory Areas	311	153	158
COAa	Cortical amygdalar area, anterior part	Olfactory Areas	763	387	376
COAp	Cortical amygdalar area, posterior part	Olfactory Areas	2495	1251	1244
PAA	Piriform-amygdalar area	Olfactory Areas	1235	619	616
TR	Postpiriform transition area	Olfactory Areas	1323	658	665
CA1	Field CA1	Hippocampal formation	10278	5145	5133
CA2	Field CA2	Hippocampal formation	451	226	225
CA3	Field CA3	Hippocampal formation	6289	3143	3146
DG	Dentate gyrus	Hippocampal formation	6571	3275	3296
FC	Fasciola cinerea	Hippocampal formation	57	29	28
IG	Induseum griseum	Hippocampal formation	108	40	68
ENT	Entorhinal area	Hippocampal formation	11476	5741	5735
PAR	Parasubiculum	Hippocampal formation	930	467	463
POST	Postsubiculum	Hippocampal formation	1074	535	539
PRE	Presubiculum	Hippocampal formation	906	454	452
SUB	Subiculum	Hippocampal formation	2146	1070	1076
Pros	Prosubiculum	Hippocampal formation	1185	594	591
HATA	Hippocampo-amygdalar transition area	Hippocampal formation	420	213	207
APr	Area prostriata	Hippocampal formation	361	179	182
CLA	Claustrum	Cortical subplate	545	271	274
Epd	Endopiriform nucleus, dorsal part	Cortical subplate	1796	899	897
Epv	Endopiriform nucleus, ventral part	Cortical subplate	961	476	485
LA	Lateral amygdalar nucleus	Cortical subplate	843	424	419
BLAa	Basolateral amygdalar nucleus, anterior part	Cortical subplate	764	379	385
BLAp	Basolateral amygdalar nucleus, posterior part	Cortical subplate	710	361	349
BLAv	Basolateral amygdalar nucleus, ventral part	Cortical subplate	414	210	204

BMAa	Basomedial amygdalar nucleus, anterior part	Cortical subplate	777	387	390
BMAp	Basomedial amygdalar nucleus, posterior part	Cortical subplate	708	352	356
PA	Posterior amygdalar nucleus	Cortical subplate	966	481	485
CP	Caudoputamen	Striatum	26040	13031	13009
ACB	Nucleus accumbens	Striatum	4446	2224	2222
FS	Fundus of striatum	Striatum	424	212	212
OT	Olfactory tubercle	Striatum	3829	1913	1916
LSc	Lateral septal nucleus, caudal (caudodorsal) part	Striatum	572	288	284
LSr	Lateral septal nucleus, rostral (rostroventral) part	Striatum	1896	939	957
LSv	Lateral septal nucleus, ventral part	Striatum	601	300	301
SF	Septofimbrial nucleus	Striatum	482	215	267
SH	Septohippocampal nucleus	Striatum	33	16	17
AAA	Anterior amygdalar area	Striatum	504	250	254
BA	Bed nucleus of the accessory olfactory tract	Striatum	25	12	13
CEAc	Central amygdalar nucleus, capsular part	Striatum	308	155	153
CEAl	Central amygdalar nucleus, lateral part	Striatum	267	130	137
CEAm	Central amygdalar nucleus, medial part	Striatum	750	378	372
IA	Intercalated amygdalar nucleus	Striatum	179	89	90
MEA	Medial amygdalar nucleus	Striatum	2024	1014	1010
GPe	Globus pallidus, external segment	Pallidum	1560	784	776
GPi	Globus pallidus, internal segment	Pallidum	427	214	213
SI	Substantia innominata	Pallidum	3000	1489	1511
MA	Magnocellular nucleus	Pallidum	367	185	182
MS	Medial septal nucleus	Pallidum	405	147	258
NDB	Diagonal band nucleus	Pallidum	723	333	390

BST	Bed nuclei of the stria terminalis	Pallidum	1341	672	669
BAC	Bed nucleus of the anterior commissure	Pallidum	8	4	4
VAL	Ventral anterior-lateral complex of the thalamus	Thalamus	801	405	396
VM	Ventral medial nucleus of the thalamus	Thalamus	946	469	477
VP	Ventral posterior complex of the thalamus	Thalamus	2852	1423	1429
PoT	Posterior triangular thalamic nucleus	Thalamus	281	141	140
SPFm	Subparafascicular nucleus, magnocellular part	Thalamus	66	33	33
SPFp	Subparafascicular nucleus, parvicellular part	Thalamus	144	72	72
SPA	Subparafascicular area	Thalamus	139	57	82
PP	Peripeduncular nucleus	Thalamus	58	28	30
MGd	Medial geniculate complex, dorsal part	Thalamus	166	84	82
MGv	Medial geniculate complex, ventral part	Thalamus	276	138	138
MGm	Medial geniculate complex, medial part	Thalamus	255	127	128
LGd-sh	Dorsal part of the lateral geniculate complex, shell	Thalamus	205	103	102
LGd-co	Dorsal part of the lateral geniculate complex, core	Thalamus	420	209	211
LGd-ip	Dorsal part of the lateral geniculate complex, ipsilateral zone	Thalamus	88	44	44
LP	Lateral posterior nucleus of the thalamus	Thalamus	1221	609	612
PO	Posterior complex of the thalamus	Thalamus	1268	630	638

POL	Posterior limiting nucleus of the thalamus	Thalamus	204	103	101
SGN	Suprageniculate nucleus	Thalamus	184	93	91
Eth	Ethmoid nucleus of the thalamus	Thalamus	240	117	123
AV	Anteroventral nucleus of thalamus	Thalamus	415	208	207
AMd	Anteromedial nucleus, dorsal part	Thalamus	247	124	123
AMv	Anteromedial nucleus,ventral part	Thalamus	172	86	86
AD	Anterodorsal nucleus	Thalamus	164	83	81
IAM	Interanteromedial nucleus of the thalamus	Thalamus	47	20	27
IAD	Interanterodorsal nucleus of the thalamus	Thalamus	120	59	61
LD	Lateral dorsal nucleus of thalamus	Thalamus	1006	503	503
IMD	Intermediodorsal nucleus of the thalamus	Thalamus	186	74	112
MD	Mediodorsal nucleus of thalamus	Thalamus	1373	678	695
SMT	Submedial nucleus of the thalamus	Thalamus	297	150	147
PR	Perireunensis nucleus	Thalamus	150	75	75
PVT	Paraventricular nucleus of the thalamus	Thalamus	444	178	266
PT	Parataenial nucleus	Thalamus	230	113	117
RE	Nucleus of reuniens	Thalamus	436	203	233
Xi	Xiphoid thalamic nucleus	Thalamus	74	14	60
RH	Rhomboid nucleus	Thalamus	93	38	55
CM	Central medial nucleus of the thalamus	Thalamus	256	108	148
PCN	Paracentral nucleus	Thalamus	231	118	113
CL	Central lateral nucleus of the thalamus	Thalamus	351	180	171
PF	Parafascicular nucleus	Thalamus	507	258	249
PIL	Posterior intralaminar thalamic nucleus	Thalamus	168	84	84

RT	Reticular nucleus of the thalamus	Thalamus	1432	718	714
IGL	Intergeniculate leaflet of the lateral geniculate complex	Thalamus	67	34	33
IntG	Intermediate geniculate nucleus	Thalamus	22	11	11
Lgv	Ventral part of the lateral geniculate complex	Thalamus	408	205	203
SubG	Subgeniculate nucleus	Thalamus	27	13	14
MH	Medial habenula	Thalamus	315	157	158
LH	Lateral habenula	Thalamus	343	169	174
SO	Supraoptic nucleus	Hypothalamus	40	21	19
ASO	Accessory supraoptic group	Hypothalamus	3	2	1
PVH	Paraventricular hypothalamic nucleus	Hypothalamus	179	89	90
Pva	Periventricular hypothalamic nucleus, anterior part	Hypothalamus	30	28	2
Pvi	Periventricular hypothalamic nucleus, intermediate part	Hypothalamus	151	118	33
ARH	Arcuate hypothalamic nucleus	Hypothalamus	277	134	143
ADP	Anterodorsal preoptic nucleus	Hypothalamus	91	46	45
AVP	Anteroventral preoptic nucleus	Hypothalamus	89	47	42
AVPV	Anteroventral periventricular nucleus	Hypothalamus	184	89	95
DMH	Dorsomedial nucleus of the hypothalamus	Hypothalamus	386	177	209
MEPO	Median preoptic nucleus	Hypothalamus	35	2	33
MPO	Medial preoptic area	Hypothalamus	566	282	284
OV	Vascular organ of the lamina terminalis	Hypothalamus	6	0	6
PD	Posterodorsal preoptic nucleus	Hypothalamus	10	5	5
PS	Parastrial nucleus	Hypothalamus	102	50	52
PVp	Periventricular hypothalamic nucleus, posterior part	Hypothalamus	117	56	61
PVpo	Periventricular hypothalamic nucleus, preoptic part	Hypothalamus	112	55	57

SBPV	Subparaventricular zone	Hypothalamus	120	47	73
SCH	Suprachiasmatic nucleus	Hypothalamus	69	35	34
SFO	Subfornical organ	Hypothalamus	22	7	15
VMPO	Ventromedial preoptic nucleus	Hypothalamus	44	22	22
VLPO	Ventrolateral preoptic nucleus	Hypothalamus	63	30	33
AHN	Anterior hypothalamic nucleus	Hypothalamus	723	363	360
MBO	Mammillary body	Hypothalamus	1017	478	539
MPN	Medial preoptic nucleus	Hypothalamus	401	191	210
PMd	Dorsal premammillary nucleus	Hypothalamus	138	70	68
Pmv	Ventral premammillary nucleus	Hypothalamus	194	97	97
PVHd	Paraventricular hypothalamic nucleus, descending division	Hypothalamus	126	62	64
VMH	Ventromedial hypothalamic nucleus	Hypothalamus	543	270	273
PH	Posterior hypothalamic nucleus	Hypothalamus	701	338	363
LHA	Lateral hypothalamic area	Hypothalamus	2117	1062	1055
LPO	Lateral preoptic area	Hypothalamus	511	257	254
PST	Preparasubthalamic nucleus	Hypothalamus	15	8	7
PSTN	Parasubthalamic nucleus	Hypothalamus	161	79	82
PeF	Perifornical nucleus	Hypothalamus	211	106	105
RCH	Retrochiasmatic area	Hypothalamus	137	69	68
STN	Subthalamic nucleus	Hypothalamus	200	100	100
TU	Tuberal nucleus	Hypothalamus	530	268	262
ZI	Zona incerta	Hypothalamus	1815	910	905
ME	Median eminence	Hypothalamus	85	34	51
SCs	Superior colliculus, sensory related	Midbrain	2124	1042	1082
ICc	Inferior colliculus, central nucleus	Midbrain	1120	558	562
Icd	Inferior colliculus,dorsal nucleus	Midbrain	1311	651	660
Ice	Inferior colliculus, external	Midbrain	2012	1010	1002
NB	Nucleus of the brachium of the inferior colliculus	Midbrain	89	46	43
SAG	Nucleus sagulum	Midbrain	107	52	55
PBG	Parabigeminal nucleus	Midbrain	49	25	24

MEV	Midbrain trigeminal nucleus	Midbrain	13	7	6
SCO	Subcommissural organ	Midbrain	13	2	11
SNr	Substantia nigra, reticular part	Midbrain	1564	787	777
VTA	Ventral tegmental area	Midbrain	427	211	216
PN	Paranigral nucleus	Midbrain	23	11	12
RR	Midbrain reticular nucleus, retrorubral area	Midbrain	131	66	65
MRN	Midbrain reticular nucleus	Midbrain	5174	2588	2586
SCm	Superior colliculus, motor related	Midbrain	5662	2789	2873
PRC	Precommissural nucleus	Midbrain	174	87	87
INC	Interstitial nucleus of Cajal	Midbrain	80	40	40
ND	Nucleus of Darkschewitsch	Midbrain	97	50	47
SU3	Supraoculomotor periaqueductal gray	Midbrain	42	21	21
APN	Anterior pretectal nucleus	Midbrain	1277	639	638
MPT	Medial pretectal area	Midbrain	47	23	24
NOT	Nucleus of the optic tract	Midbrain	214	108	106
NPC	Nucleus of the posterior commissure	Midbrain	286	144	142
OP	Olivary pretectal nucleus	Midbrain	60	30	30
PPT	Posterior pretectal nucleus	Midbrain	143	72	71
RPF	Retroparafascicular nucleus	Midbrain	64	31	33
CUN	Cuneiform nucleus	Midbrain	564	284	280
RN	Red nucleus	Midbrain	792	396	396
III	Oculomotor nucleus	Midbrain	32	17	15
MA3	Medial accesory oculomotor nucleus	Midbrain	20	10	10
EW	Edinger-Westphal nucleus	Midbrain	19	0	19
IV	Trochlear nucleus	Midbrain	6	3	3
VTN	Ventral tegmental nucleus	Midbrain	34	17	17
AT	Anterior tegmental nucleus	Midbrain	43	21	22
LT	Lateral terminal nucleus of the accessory optic tract	Midbrain	17	9	8

DT	Dorsal terminal nucleus of the accessory optic tract	Midbrain	12	6	6
MT	Medial terminal nucleus of the accessory optic tract	Midbrain	51	25	26
SNc	Substantia nigra, compact part	Midbrain	203	101	102
PPN	Pedunculopontine nucleus	Midbrain	888	442	446
IF	Interfascicular nucleus raphe	Midbrain	84	34	50
IPN	Interpeduncular nucleus	Midbrain	348	147	201
RL	Rostral linear nucleus raphe	Midbrain	57	17	40
CLI	Central linear nucleus raphe	Midbrain	82	35	47
DR	Dorsal nucleus raphe	Midbrain	151	37	114
NLL	Nucleus of the lateral lemniscus	Pons	739	369	370
PSV	Principal sensory nucleus of the trigeminal	Pons	1108	550	558
PB	Parabrachial nucleus	Pons	1136	565	570
POR	Superior olivary complex, periolivary region	Pons	372	185	187
SOCm	Superior olivary complex, medial part	Pons	198	98	100
SOCl	Superior olivary complex, lateral part	Pons	340	170	170
B	Barrington's nucleus	Pons	15	8	7
DTN	Dorsal tegmental nucleus	Pons	105	55	50
PDTg	Posterodorsal tegmental nucleus	Pons	47	23	24
PCG	Pontine central gray	Pons	521	251	270
PRNc	Pontine reticular nucleus, caudal part	Pons	2374	1191	1183
SG	Supragenual nucleus	Pons	16	9	7
SUT	Supratrigeminal nucleus	Pons	264	132	132
TRN	Tegmental reticular nucleus	Pons	674	338	336
V	Motor nucleus of trigeminal	Pons	350	176	174
P5	Peritrigeminal zone	Pons	327	163	164
Acs5	Accessory trigeminal nucleus	Pons	14	7	7
PC5	Parvicellular motor 5 nucleus	Pons	66	33	33

I5	Intertrigeminal nucleus	Pons	47	25	22
CS	Superior central nucleus raphe	Pons	591	276	315
LC	Locus ceruleus	Pons	13	6	7
LDT	Laterodorsal tegmental nucleus	Pons	204	102	102
NI	Nucleus incertus	Pons	124	52	72
PRNr	Pontine reticular nucleus	Pons	2334	1165	1169
RPO	Nucleus raphe pontis	Pons	83	36	47
SLC	Subceruleus nucleus	Pons	29	15	14
SLD	Sublaterodorsal nucleus	Pons	49	24	25
AP	Area Postrema	Medulla	53	18	35
DCO	Dorsal cochlear nucleus	Medulla	610	302	308
VCO	Ventral cochlear nucleus	Medulla	1031	514	517
CU	Cuneate nucleus	Medulla	328	164	164
GR	Gracile nucleus	Medulla	81	40	41
ECU	External cuneate nucleus	Medulla	209	104	105
NTB	Nucleus of the trapezoid body	Medulla	153	77	76
NTS	Nucleus of the solitary tract	Medulla	838	406	432
SPVc	Spinal nucleus of the trigeminal, caudal part	Medulla	1658	826	832
SPVI	Spinal nucleus of the trigeminal, interpolar part	Medulla	1808	904	904
SPVO	Spinal nucleus of the trigeminal, oral part	Medulla	1021	514	507
Pa5	Paratrigeminal nucleus	Medulla	101	51	50
VI	Abducens nucleus	Medulla	33	16	17
VII	Facial motor nucleus	Medulla	931	467	464
ACVII	Accessory facial motor nucleus	Medulla	4	2	2
AMBd	Nucleus ambiguus, dorsal division	Medulla	27	14	13
AMBv	Nucleus ambiguus, ventral division	Medulla	16	8	8
DMX	Dorsal motor nucleus of the vagus nerve	Medulla	168	87	81
GRN	Gigantocellular reticular nucleus	Medulla	2606	1274	1332
ICB	Infracerebellar nucleus	Medulla	52	25	27

IO	Inferior olivary complex	Medulla	486	243	243
IRN	Intermediate reticular nucleus	Medulla	2766	1379	1387
ISN	Inferior salivatory nucleus	Medulla	10	5	5
LIN	Linear nucleus of the medulla	Medulla	65	34	31
LRNm	Lateral reticular nucleus, magnocellular part	Medulla	517	258	259
LRNp	Lateral reticular nucleus, parvicellular part	Medulla	59	29	30
MARN	Magnocellular reticular nucleus	Medulla	539	265	274
MDRNd	Medullary reticular nucleus, dorsal part	Medulla	1021	511	510
MDRNv	Medullary reticular nucleus, ventral part	Medulla	897	450	447
PARN	Parvicellular reticular nucleus	Medulla	2331	1165	1166
PAS	Parasolitary nucleus	Medulla	29	14	15
PGRNd	Paragigantocellular reticular nucleus, dorsal part	Medulla	247	125	122
PGRNl	Paragigantocellular reticular nucleus, lateral part	Medulla	713	359	354
NR	Nucleus of Roller	Medulla	35	18	17
PRP	Nucleus prepositus	Medulla	237	115	122
PPY	Parapyramidal nucleus	Medulla	99	48	51
LAV	Lateral vestibular nucleus	Medulla	283	139	144
MV	Medial vestibular nucleus	Medulla	1840	922	918
SPIV	Spinal vestibular nucleus	Medulla	761	379	382
SUV	Superior vestibular nucleus	Medulla	350	177	173
x	Nucleus x	Medulla	56	27	29
XII	Hypoglossal nucleus	Medulla	265	132	133
y	Nucleus y	Medulla	28	14	14
RM	Nucleus raphe magnus	Medulla	113	0	113
RPA	Nucleus raphe pallidus	Medulla	67	0	67
RO	Nucleus raphe obscurus	Medulla	69	0	69
LING	Lingula (I)	Cerebellum	126	55	71
CENT2	Lobule II	Cerebellum	1336	630	706

CENT3	Lobule III	Cerebellum	2742	1320	1422
CUL	Culmen	Cerebellum	6777	3298	3479
DEC	Declive (VI)	Cerebellum	3334	1612	1722
FOTU	Folium-tuber vermis (VII)	Cerebellum	1030	498	532
PYR	Pyramus (VIII)	Cerebellum	1233	590	643
UVU	Uvula (IX)	Cerebellum	2162	1036	1126
NOD	Nodulus (X)	Cerebellum	1503	721	782
SIM	Simple lobule	Cerebellum	5709	2853	2856
ANcr1	Crus 1	Cerebellum	5660	2830	2830
ANcr2	Crus 2	Cerebellum	5118	2560	2558
PRM	Paramedian lobule	Cerebellum	4866	2435	2431
COPY	Copula pyramidis	Cerebellum	2490	1246	1244
PFL	Paraflocculus	Cerebellum	5742	2869	2873
FL	Flocculus	Cerebellum	1310	658	652
FN	Fastigial nucleus	Cerebellum	501	249	252
IP	Interposed nucleus	Cerebellum	348	147	201
DN	Dentate nucleus	Cerebellum	331	167	164
VeCB	Vestibulocerebellar nucleus	Cerebellum	87	46	41

Table 2. Anatomical Metaregions

ABBREVIATION	NAME	MACRO
MOp	Primary motor area	Isocortex
MOs	Secondary motor area	Isocortex
SSp-n	Primary somatosensory area, nose	Isocortex
SSp-bfd	Primary somatosensory area, barrel field	Isocortex
SSp-ll	Primary somatosensory area, lower limb	Isocortex
SSp-m	Primary somatosensory area, mouth	Isocortex
SSp-ul	Primary somatosensory area, upper limb	Isocortex
SSp-tr	Primary somatosensory area, trunk	Isocortex
SSp-un	Primary somatosensory area, unassigned	Isocortex
SSs	Supplemental somatosensory area	Isocortex
GU	Gustatory areas	Isocortex
VISC	Visceral area	Isocortex
AUDd	Dorsal auditory area	Isocortex
AUDp	Primary auditory area	Isocortex
AUDpo	Posterior auditory area	Isocortex
AUDv	Ventral auditory area	Isocortex

VISal	Anterolateral visual area	Isocortex
VISam	Anteromedial visual area	Isocortex
VISl	Lateral visual area	Isocortex
VISp	Primary visual area	Isocortex
VISpl	Posterolateral visual area	Isocortex
VISpm	posteromedial visual area	Isocortex
VISli	Laterointermediate area	Isocortex
VISpor	Postrhinal area	Isocortex
ACAd	Anterior cingulate area, dorsal part	Isocortex
ACAv	Anterior cingulate area, ventral part	Isocortex
PL	Prelimbic area	Isocortex
ILA	Infralimbic area	Isocortex
ORB	Orbital area	Isocortex
AId	Agranular insular area, dorsal part	Isocortex
AIp	Agranular insular area, posterior part	Isocortex
AIv	Agranular insular area, ventral part	Isocortex
RSPagl	Retrosplenial area, lateral agranular part	Isocortex
RSPd	Retrosplenial area, dorsal part	Isocortex
RSPv	Retrosplenial area, ventral part	Isocortex
PTLp	Posterior parietal association areas	Isocortex
TEa	Temporal association areas	Isocortex
PERI	Perirhinal area	Isocortex
ECT	Ectorhinal area	Isocortex
MOB	Main olfactory bulb	Olfactory Areas

AOB	Accessory olfactory bulb	Olfactory Areas
AON	Anterior olfactory nucleus	Olfactory Areas
TT	Taenia tecta	Olfactory Areas
DP	Dorsal peduncular area	Olfactory Areas
PIR	Piriform area	Olfactory Areas
NLOT	Nucleus of the lateral olfactory tract	Olfactory Areas
COA	Cortical amygdalar area	Olfactory Areas
PAA	Piriform-amygdalar area	Olfactory Areas
CA	Ammon's horn	Hippocampal formation
DG	Dentate gyrus	Hippocampal formation
ENT	Entorhinal area	Hippocampal formation
PAR	Parasubiculum	Hippocampal formation
POST	Postsubiculum	Hippocampal formation
PRE	Presubiculum	Hippocampal formation
SUB	Subiculum	Hippocampal formation
ProS	Prosubiculum	Hippocampal formation
HATA	Hippocampo-amygdalar transition area	Hippocampal formation
APr	Area prostriata	Hippocampal formation
CLA	Claustrum	Cortical subplate

EP	Endopiriform nucleus	Cortical subplate
LA	Lateral amygdalar nucleus	Cortical subplate
BLA	Basolateral amygdalar nucleus	Cortical subplate
BMA	Basomedial amygdalar nucleus	Cortical subplate
PA	Posterior amygdalar nucleus	Cortical subplate
STRd	Striatum dorsal region	Striatum
STRv	Striatum ventral region	Striatum
LSX	Lateral septal complex	Striatum
sAMY	Striatum-like amygdalar nuclei	Striatum
PALd	Pallidum, dorsal region	Pallidum
PALv	Pallidum, ventral region	Pallidum
PALm	Pallidum, medial region	Pallidum
PALc	Pallidum, caudal region	Pallidum
DORsm	Thalamus, sensory-motor cortex related	Thalamus
DORpm	Thalamus, polymodal association cortex related	Thalamus
PVZ	Periventricular zone	Hypothalamus
PVR	Periventricular region	Hypothalamus
MEZ	Hypothalamic medial zone	Hypothalamus
LZ	Hypothalamic lateral zone	Hypothalamus
MBsen	Midbrain, sensory related	Midbrain

MBmot	Midbrain, motor related	Midbrain
MBsta	Midbrain, behavioral state related	Midbrain
P-sen	Pons, sensory related	Pons
P-mot	Pons, motor related	Pons
P-sat	Pons, behavioral state related	Pons
MY-sen	Medulla, sensory related	Medulla
MY-mot	Medulla, motor related	Medulla
CBX	Cerebellar cortex	Cerebellum
CBN	Cerebellar nuclei	Cerebellum

References

Abdelnour, F., Voss, H.U., & Raj, A. (2014) Network diffusion accurately models the relationship between structural and functional brain connectivity networks. *Neuroimage*, **90**, 335–347.

Aerts, H., Fias, W., Caeyenberghs, K., & Marinazzo, D. (2016) Brain networks under attack: Robustness properties and the impact of lesions. *Brain*, **139**, 3063–3083.

Alstott, J., Breakspear, M., Hagmann, P., Cammoun, L., & Sporns, O. (2009) Modeling the impact of lesions in the human brain. *PLoS Comput. Biol.*, **5**.

Avena-Koenigsberger, A., Misic, B., & Sporns, O. (2018) Communication dynamics in complex brain networks. *Nat. Rev. Neurosci.*, **19**, 17–33.

Baldassarre, G., Caligiore, D., & Mannella, F. (2013) The Hierarchical Organisation of Cortical and Basal-Ganglia Systems: A Computationally-Informed Review and Integrated Hypothesis. In Baldassarre, G. & Mirolli, M. (eds), *Computational and Robotic Models of the Hierarchical Organization of Behavior*. Springer Berlin Heidelberg, Berlin, Heidelberg, pp. 237–270.

Barttfeld, P., Uhrig, L., Sitt, J.D., Sigman, M., Jarraya, B., & Dehaene, S. (2015) Signature of consciousness in the dynamics of resting-state brain activity. *Proc. Natl. Acad. Sci.*, **112**, 887–892.

Bassett, D.S. & Bullmore, E.T. (2017) Small-World Brain Networks Revisited. *Neuroscientist*, **23**, 499–516.

Benkarim, O., Paquola, C., Park, B., Royer, J., & Rodríguez-cruces, R. (2021) A Riemannian approach to predicting brain function from the structural connectome. *bioRxiv*.

Benkarim, O., Paquola, C., Park, B. yong, Hong, S.J., Royer, J., Vos de Wael, R., Lariviere, S., Valk, S., Bzdok, D., Mottron, L., & C. Bernhardt, B. (2021) Connectivity alterations in autism reflect functional idiosyncrasy. *Commun. Biol.*, **4**, 1–15.

Benzi, M. & Klymko, C. (2013) Total communicability as a centrality measure. *J. Complex Networks*, **1**, 124–149.

Bertero, A., Liska, A., Pagani, M., Parolisi, R., Masferrer, M.E., Gritti, M., Pedrazzoli, M., Galbusera, A., Sarica, A.,

Cerasa, A., Buffelli, M., Tonini, R., Buffo, A., Gross, C., Pasqualetti, M., & Gozzi, A. (2018) Autism-associated 16p11.2 microdeletion impairs prefrontal functional connectivity in mouse and human. *Brain*, **141**, 2055–2065.

Bertolero, M.A., Yeo, B.T.T., & D'Esposito, M. (2017) The diverse club. *Nat. Commun.*, **8**, 1–11.

Betzel, R.F. & Bassett, D.S. (2017) Multi-scale brain networks. *Neuroimage*, **160**, 73–83.

Betzel, R.F. & Bassett, D.S. (2018) Specificity and robustness of long-distance connections in weighted, interareal connectomes. *Proc. Natl. Acad. Sci.*, **115**, E4880–E4889.

Betzel, R.F., Medaglia, J.D., & Bassett, D.S. (2018) Diversity of meso-scale architecture in human and non-human connectomes. *Nat. Commun.*, **9**, 1–14.

Betzel, R.F., Medaglia, J.D., Papadopoulos, L., Baum, G.L., Gur, R., Gur, R., Roalf, D., Satterthwaite, T.D., & Bassett, D.S. (2017) The modular organization of human anatomical brain networks: Accounting for the cost of wiring. *Netw. Neurosci.*, **1**, 42–68.

Bordier, C., Nicolini, C., & Bifone, A. (2017) Graph analysis and modularity of brain functional connectivity networks: Searching for the optimal threshold. *Front. Neurosci.*, **11**, 1–9.

Breakspear, M. (2017) Dynamic models of large-scale brain activity. *Nat. Neurosci.*, **20**, 340–352.

Buckner, R.L. & DiNicola, L.M. (2019) The brain's default network: updated anatomy, physiology and evolving insights. *Nat. Rev. Neurosci.*, **20**, 593–608.

Bullmore, E. & Sporns, O. (2012) The economy of brain network organization. *Nat. Rev. Neurosci.*, **13**, 336–349.

Burt, J.B., Demirtaş, M., Eckner, W.J., Navejar, N.M., Ji, J.L., Martin, W.J., Bernacchia, A., Anticevic, A., & Murray, J.D. (2018) Hierarchy of transcriptomic specialization across human cortex captured by structural neuroimaging topography. *Nat. Neurosci.*, **21**, 1251–1259.

Cabral, J., Kringelbach, M.L., & Deco, G. (2017) Functional connectivity dynamically evolves on multiple time-scales over a static structural connectome: Models and mechanisms. *Neuroimage*, **160**, 84–96.

Calabrese, E., Badea, A., Cofer, G., Qi, Y., & Johnson, G.A. (2015) A Diffusion MRI tractography connectome of the mouse brain and comparison with neuronal tracer data. *Cereb. Cortex*, **25**, 4628–4637.

Cardin, J.A., Crair, M.C., & Higley, M.J. (2020) Mesoscopic Imaging: Shining a Wide Light on Large-Scale Neural

Dynamics. *Neuron*, **108**, 33–43.

Choi, H. & Mihalas, S. (2019) Synchronization dependent on spatial structures of a mesoscopic whole-brain network. *PLOS Comput. Biol.*, **15**, e1006978.

Coletta, L., Pagani, M., Whitesell, J.D., Harris, J.A., Bernhardt, B., & Gozzi, A. (2020) Network structure of the mouse brain connectome with voxel resolution. *Sci. Adv.*, **6**, eabb7187.

Crossley, N.A., Mechelli, A., Scott, J., Carletti, F., Fox, P.T., Mcguire, P., & Bullmore, E.T. (2014) The hubs of the human connectome are generally implicated in the anatomy of brain disorders. *Brain*, **137**, 2382–2395.

de Lange, S.C., Scholtens, L.H., van den Berg, L.H., Boks, M.P., Bozzali, M., Cahn, W., Dannlowski, U., Durston, S., Geuze, E., van Haren, N.E.M., Hillegers, M.H.J., Koch, K., Jurado, M.Á., Mancini, M., Marqués-Iturria, I., Meinert, S., Ophoff, R.A., Reess, T.J., Repple, J., Kahn, R.S., van den Heuvel, M.P., & Initiative, A.D.N. (2019) Shared vulnerability for connectome alterations across psychiatric and neurological brain disorders. *Nat. Hum. Behav.*, **3**, 988–998.

Deco, G., Jirsa, V.K., Robinson, P.A., Breakspear, M., & Friston, K. (2008) The dynamic brain: From spiking neurons to neural masses and cortical fields. *PLoS Comput. Biol.*, **4**, 1–35.

Demertzi, A., Tagliazucchi, E., Dehaene, S., Deco, G., Barttfeld, P., Raimondo, F., Martial, C., Fernández-Espejo, D., Rohaut, B., Voss, H.U., Schiff, N.D., Owen, A.M., Laureys, S., Naccache, L., & Sitt, J.D. (2019) Human consciousness is supported by dynamic complex patterns of brain signal coordination. *Sci. Adv.*, **5**, 1–12.

Díaz-Parra, A., Osborn, Z., Canals, S., Moratal, D., & Sporns, O. (2017) Structural and functional, empirical and modeled connectivity in the cerebral cortex of the rat. *Neuroimage*, **159**, 170–184.

Esfahlani, F.Z., Jo, Y., Faskowitz, J., Byrge, L., Kennedy, D.P., Sporns, O., & Betzel, R.F. (2020) High-amplitude cofluctuations in cortical activity drive functional connectivity. *Proc. Natl. Acad. Sci. U. S. A.*, **117**, 28393–28401.

Fulcher, B.D. & Fornito, A. (2016) A transcriptional signature of hub connectivity in the mouse connectome. *Proc. Natl. Acad. Sci.*, **113**, 1435–1440.

Fulcher, B.D., Murray, J.D., Zerbi, V., & Wang, X.-J. (2019) Multimodal gradients across mouse cortex. *Proc. Natl. Acad. Sci.*, **116**, 4689–4695.

Garrison, K.A., Scheinost, D., Finn, E.S., Shen, X., & Constable, R.T. (2015) The (in)stability of functional brain network

measures across thresholds. *Neuroimage*, **118**, 651–661.

Giorgi, A., Migliarini, S., Galbusera, A., Maddaloni, G., Mereu, M., Margiani, G., Gritti, M., Landi, S., Trovato, F., Bertozzi, S.M., Armirotti, A., Ratto, G.M., De Luca, M.A., Tonini, R., Gozzi, A., & Pasqualetti, M. (2017) Brain-wide Mapping of Endogenous Serotonergic Transmission via Chemogenetic fMRI. *Cell Rep.*, **21**, 910–918.

Gollo, L.L., Roberts, J.A., Cropley, V.L., Di Biase, M.A., Pantelis, C., Zalesky, A., & Breakspear, M. (2018) Fragility and volatility of structural hubs in the human connectome. *Nat. Neurosci.*, **21**, 1107–1116.

Goni, J., van den Heuvel, M.P., Avena-Koenigsberger, A., Velez de Mendizabal, N., Betzel, R.F., Griffa, A., Hagmann, P., Corominas-Murtra, B., Thiran, J.-P., & Sporns, O. (2014) Resting-brain functional connectivity predicted by analytic measures of network communication. *Proc. Natl. Acad. Sci.*, **111**, 833–838.

Gordon, E.M., Lynch, C.J., Gratton, C., Laumann, T.O., Gilmore, A.W., Greene, D.J., Ortega, M., Nguyen, A.L., Schlaggar, B.L., Petersen, S.E., Dosenbach, N.U.F., & Nelson, S.M. (2018) Three Distinct Sets of Connector Hubs Integrate Human Brain Function. *Cell Rep.*, **24**, 1687–1695.

Goulas, A., Majka, P., Rosa, M.G.P., & Hilgetag, C.C. (2019) A blueprint of mammalian cortical connectomes. *PLOS Biol.*, **17**, e2005346.

Gozzi, A. & Schwarz, A.J. (2016) Large-scale functional connectivity networks in the rodent brain. *Neuroimage*, **127**, 496–509.

Graham, D., Avena-Koenigsberger, A., & Mišić, B. (2020) Editorial: Network Communication in the Brain. *Netw. Neurosci.*, **4**, 976–979.

Grandjean, J., Canella, C., Anckaerts, C., Ayrancı, G., Bougacha, S., Bienert, T., Buehlmann, D., Coletta, L., Gallino, D., Gass, N., Garin, C.M., Nadkarni, N.A., Hübner, N.S., Karatas, M., Komaki, Y., Kreitz, S., Mandino, F., Mechling, A.E., Sato, C., Sauer, K., Shah, D., Strobelt, S., Takata, N., Wank, I., Wu, T., Yahata, N., Yeow, L.Y., Yee, Y., Aoki, I., Chakravarty, M.M., Chang, W.-T., Dhenain, M., von Elverfeldt, D., Harsan, L.-A., Hess, A., Jiang, T., Keliris, G.A., Lerch, J.P., Meyer-Lindenberg, A., Okano, H., Rudin, M., Sartorius, A., Van der Linden, A., Verhoye, M., Weber-Fahr, W., Wenderoth, N., Zerbi, V., & Gozzi, A. (2020) Common functional networks in the mouse brain revealed by multi-centre resting-state fMRI analysis. *Neuroimage*, **205**.

Grandjean, J., Zerbi, V., Balsters, J.H., Wenderoth, N., & Rudin, M. (2017) Structural Basis of Large-Scale Functional

Connectivity in the Mouse. *J. Neurosci.*, **37**, 8092–8101.

Gratton, C., Sun, H., & Petersen, S.E. (2018) Control networks and hubs. *Psychophysiology*, **55**, 1–18.

Grayson, D.S., Bliss-Moreau, E., Machado, C.J., Bennett, J., Shen, K., Grant, K.A., Fair, D.A., & Amaral, D.G. (2016) The Rhesus Monkey Connectome Predicts Disrupted Functional Networks Resulting from Pharmacogenetic Inactivation of the Amygdala. *Neuron*, **91**, 453–466.

Griffa, A., Baumann, P.S., Thiran, J.-P., & Hagmann, P. (2013) Structural connectomics in brain diseases. *Neuroimage*, **80**, 515–526.

Guimerà, R. & Nunes Amaral, L.A. (2005) Functional cartography of complex metabolic networks. *Nature*, **433**, 895–900.

Gutierrez-Barragan, D., Basson, M.A., Panzeri, S., & Gozzi, A. (2019) Infraslow State Fluctuations Govern Spontaneous fMRI Network Dynamics. *Curr. Biol.*, **29**, 2295–2306.

Hallquist, M.N. & Hillary, F.G. (2018) Graph theory approaches to functional network organization in brain disorders: A critique for a brave new small-world. *Netw. Neurosci.*, **3**, 1–26.

Harris, J.A., Mihalas, S., Hirokawa, K.E., Whitesell, J.D., Choi, H., Bernard, A., Bohn, P., Caldejon, S., Casal, L., Cho, A., Feiner, A., Feng, D., Gaudreault, N., Gerfen, C.R., Graddis, N., Groblewski, P.A., Henry, A.M., Ho, A., Howard, R., Knox, J.E., Kuan, L., Kuang, X., Lecoq, J., Lesnar, P., Li, Y., Luviano, J., McConoughey, S., Mortrud, M.T., Naeemi, M., Ng, L., Oh, S.W., Ouellette, B., Shen, E., Sorensen, S.A., Wakeman, W., Wang, Q., Wang, Y., Williford, A., Phillips, J.W., Jones, A.R., Koch, C., & Zeng, H. (2019) Hierarchical organization of cortical and thalamic connectivity. *Nature*, **575**, 195–202.

Henriksen, S., Pang, R., & Wronkiewicz, M. (2016) A simple generative model of the mouse mesoscale connectome. *Elife*, **5**, 1–19.

Hildebrand, D.G.C., Cicconet, M., Torres, R.M., Choi, W., Quan, T.M., Moon, J., Wetzel, A.W., Scott Champion, A., Graham, B.J., Randlett, O., Plummer, G.S., Portugues, R., Bianco, I.H., Saalfeld, S., Baden, A.D., Lillaney, K., Burns, R., Vogelstein, J.T., Schier, A.F., Lee, W.C.A., Jeong, W.K., Lichtman, J.W., & Engert, F. (2017) Whole-brain serial-section electron microscopy in larval zebrafish. *Nature*, **545**, 345–349.

Hilgetag, C.C. & Goulas, A. (2020) 'Hierarchy' in the organization of brain networks. *Philos. Trans. R. Soc. B Biol. Sci.*,

375.

Hong, S.J., de Wael, R.V., Bethlehem, R.A.I., Lariviere, S., Paquola, C., Valk, S.L., Milham, M.P., Di Martino, A., Margulies, D.S., Smallwood, J., & Bernhardt, B.C. (2019) Atypical functional connectome hierarchy in autism. *Nat. Commun.*, **10**, 1–13.

Hori, Y., Schaeffer, D.J., Gilbert, K.M., Hayrynen, L.K., Cléry, J.C., Gati, J.S., Menon, R.S., & Everling, S. (2020) Comparison of resting-state functional connectivity in marmosets with tracer-based cellular connectivity. *Neuroimage*, **204**, 116241.

Huang, Z., Zhang, J., Wu, J., Mashour, G.A., & Hudetz, A.G. (2020) Temporal circuit of macroscale dynamic brain activity supports human consciousness. *Sci. Adv.*, **6**, 1–15.

Huntenburg, J.M., Bazin, P.L., & Margulies, D.S. (2018) Large-Scale Gradients in Human Cortical Organization. *Trends Cogn. Sci.*, **22**, 21–31.

Iurilli, G., Ghezzi, D., Olcese, U., Lassi, G., Nazzaro, C., Tonini, R., Tucci, V., Benfenati, F., & Medini, P. (2012) Sound-Driven Synaptic Inhibition in Primary Visual Cortex. *Neuron*, **73**, 814–828.

Jeurissen, B., Descoteaux, M., Mori, S., & Leemans, A. (2019) Diffusion MRI fiber tractography of the brain. *NMR Biomed.*, **32**, e3785.

Kale, P., Zalesky, A., & Gollo, L.L. (2018) Estimating the impact of structural directionality: How reliable are undirected connectomes? *Netw. Neurosci.*, **2**, 259–284.

Khambhati, A.N., Sizemore, A.E., Betzel, R.F., & Bassett, D.S. (2018) Modeling and interpreting mesoscale network dynamics. *Neuroimage*, **180**, 337–349.

Knox, J.E., Harris, K.D., Graddis, N., Whitesell, J.D., Zeng, H., Harris, J.A., Shea-Brown, E., & Mihalas, S. (2019) High-resolution data-driven model of the mouse connectome. *Netw. Neurosci.*, **3**, 217–236.

Kunst, M., Laurell, E., Mokayes, N., Kramer, A., Kubo, F., Fernandes, A.M., Förster, D., Dal Maschio, M., & Baier, H. (2019) A Cellular-Resolution Atlas of the Larval Zebrafish Brain. *Neuron*, **103**, 21–38.

Lake, E.M.R., Ge, X., Shen, X., Herman, P., Hyder, F., Cardin, J.A., Higley, M.J., Scheinost, D., Papademetris, X., Crair, M.C., & Constable, R.T. (2020) Simultaneous cortex-wide fluorescence Ca2+ imaging and whole-brain fMRI. *Nat. Methods*, **17**, 1262–1271.

Lancichinetti, A. & Fortunato, S. (2012) Consensus clustering in complex networks. *Sci. Rep.*, **2**, 1–7.

Larivière, S., Vos de Wael, R., Hong, S.-J., Paquola, C., Tavakol, S., Lowe, A.J., Schrader, D. V, & Bernhardt, B.C. (2019) Multiscale Structure–Function Gradients in the Neonatal Connectome. *Cereb. Cortex*, 1–12.

Lim, S., Radicchi, F., van den Heuvel, M.P., & Sporns, O. (2019) Discordant attributes of structural and functional brain connectivity in a two-layer multiplex network. *Sci. Rep.*, **9**, 1–13.

Lin, M.K., Takahashi, Y.S., Huo, B.X., Hanada, M., Nagashima, J., Hata, J., Tolpygo, A.S., Ram, K., Lee, B.C., Miller, M.I., Rosa, M.G., Sasaki, E., Iriki, A., Okano, H., & Mitra, P. (2019) A high-throughput neurohistological pipeline for brain-wide mesoscale connectivity mapping of the common marmoset. *Elife*, **8**, 1–36.

Liska, A., Galbusera, A., Schwarz, A.J., & Gozzi, A. (2015) Functional connectivity hubs of the mouse brain. *Neuroimage*, **115**, 281–291.

Lu, H., Zou, Q., Gu, H., Raichle, M.E., Stein, E.A., & Yang, Y. (2012) Rat brains also have a default mode network. *Proc. Natl. Acad. Sci.*, **109**, 3979 LP – 3984.

Maier-Hein, K.H., Neher, P.F., Houde, J.C., Côté, M.A., Garyfallidis, E., Zhong, J., Chamberland, M., Yeh, F.C., Lin, Y.C., Ji, Q., Reddick, W.E., Glass, J.O., Chen, D.Q., Feng, Y., Gao, C., Wu, Y., Ma, J., Renjie, H., Li, Q., Westin, C.F., Deslauriers-Gauthier, S., González, J.O.O., Paquette, M., St-Jean, S., Girard, G., Rheault, F., Sidhu, J., Tax, C.M.W., Guo, F., Mesri, H.Y., Dávid, S., Froeling, M., Heemskerk, A.M., Leemans, A., Boré, A., Pinsard, B., Bedetti, C., Desrosiers, M., Brambati, S., Doyon, J., Sarica, A., Vasta, R., Cerasa, A., Quattrone, A., Yeatman, J., Khan, A.R., Hodges, W., Alexander, S., Romascano, D., Barakovic, M., Auría, A., Esteban, O., Lemkaddem, A., Thiran, J.P., Cetingul, H.E., Odry, B.L., Mailhe, B., Nadar, M.S., Pizzagalli, F., Prasad, G., Villalon-Reina, J.E., Galvis, J., Thompson, P.M., Requejo, F.D.S., Laguna, P.L., Lacerda, L.M., Barrett, R., Dell'Acqua, F., Catani, M., Petit, L., Caruyer, E., Daducci, A., Dyrby, T.B., Holland-Letz, T., Hilgetag, C.C., Stieltjes, B., & Descoteaux, M. (2017) The challenge of mapping the human connectome based on diffusion tractography. *Nat. Commun.*, **8**, 1–13.

Managò, F. & Papaleo, F. (2017) Schizophrenia: What's arc got to do with it? *Front. Behav. Neurosci.*, **11**, 1–11.

Margulies, D.S., Ghosh, S.S., Goulas, A., Falkiewicz, M., Huntenburg, J.M., Langs, G., Bezgin, G., Eickhoff, S.B., Castellanos, F.X., Petrides, M., Jefferies, E., & Smallwood, J. (2016) Situating the default-mode network along a principal gradient of macroscale cortical organization. *Proc. Natl. Acad. Sci.*, **113**, 12574–12579.

Maslov, S. & Sneppen, K. (2002) Specificity and Stability in Topology of Protein Networks. *Science*, **296**, 910–913.

Meijer, G.T., Mertens, P.E.C., Pennartz, C.M.A., Olcese, U., & Lansink, C.S. (2019) The circuit architecture of cortical multisensory processing: Distinct functions jointly operating within a common anatomical network. *Prog. Neurobiol.*, **174**, 1–15.

Mesulam, M.M. (1998) From sensation to cognition. *Brain*, **121**, 1013–1052.

Meunier, D., Lambiotte, R., & Bullmore, E.T. (2010) Modular and hierarchically modular organization of brain networks. *Front. Neurosci.*, **4**, 1–11.

Milham, M.P., Ai, L., Koo, B., Xu, T., Amiez, C., Balezeau, F., Baxter, M.G., Blezer, E.L.A., Brochier, T., Chen, A., Croxson, P.L., Damatac, C.G., Dehaene, S., Everling, S., Fair, D.A., Fleysher, L., Freiwald, W., Froudist-Walsh, S., Griffiths, T.D., Guedj, C., Hadj-Bouziane, F., Ben Hamed, S., Harel, N., Hiba, B., Jarraya, B., Jung, B., Kastner, S., Klink, P.C., Kwok, S.C., Laland, K.N., Leopold, D.A., Lindenfors, P., Mars, R.B., Menon, R.S., Messinger, A., Meunier, M., Mok, K., Morrison, J.H., Nacef, J., Nagy, J., Rios, M.O., Petkov, C.I., Pinsk, M., Poirier, C., Procyk, E., Rajimehr, R., Reader, S.M., Roelfsema, P.R., Rudko, D.A., Rushworth, M.F.S., Russ, B.E., Sallet, J., Schmid, M.C., Schwiedrzik, C.M., Seidlitz, J., Sein, J., Shmuel, A., Sullivan, E.L., Ungerleider, L., Thiele, A., Todorov, O.S., Tsao, D., Wang, Z., Wilson, C.R.E., Yacoub, E., Ye, F.Q., Zarco, W., Zhou, Y. di, Margulies, D.S., & Schroeder, C.E. (2018) An Open Resource for Non-human Primate Imaging. *Neuron*, **100**, 61–74.

Mišić, B., Betzel, R.F., Nematzadeh, A., Goñi, J., Griffa, A., Hagmann, P., Flammini, A., Ahn, Y.Y., & Sporns, O. (2015) Cooperative and Competitive Spreading Dynamics on the Human Connectome. *Neuron*, **86**, 1518–1529.

Mohanty, R., Sethares, W.A., Nair, V.A., & Prabhakaran, V. (2020) Rethinking Measures of Functional Connectivity via Feature Extraction. *Sci. Rep.*, **10**, 1–17.

Mota, B., Dos Santos, S.E., Ventura-Antunes, L., Jardim-Messeder, D., Neves, K., Kazu, R.S., Noctor, S., Lambert, K., Bertelsen, M.F., Manger, P.R., Sherwood, C.C., Kaas, J.H., & Herculano-Houzel, S. (2019) White matter volume and white/gray matter ratio in mammalian species as a consequence of the universal scaling of cortical folding. *Proc. Natl. Acad. Sci. U. S. A.*, **116**, 15253–15261.

Oh, S.W., Harris, J.A., Ng, L., Winslow, B., Cain, N., Mihalas, S., Wang, Q., Lau, C., Kuan, L., Henry, A.M., Mortrud, M.T., Ouellette, B., Nguyen, T.N., Sorensen, S.A., Slaughterbeck, C.R., Wakeman, W., Li, Y., Feng, D., Ho, A., Nicholas, E., Hirokawa, K.E., Bohn, P., Joines, K.M., Peng, H., Hawrylycz, M.J., Phillips, J.W., Hohmann, J.G.,

Wohnoutka, P., Gerfen, C.R., Koch, C., Bernard, A., Dang, C., Jones, A.R., & Zeng, H. (2014) A mesoscale connectome of the mouse brain. *Nature*, **508**, 207–214.

Oligschläger, S., Xu, T., Baczkowski, B.M., Falkiewicz, M., Falchier, A., Linn, G., & Margulies, D.S. (2019) Gradients of connectivity distance in the cerebral cortex of the macaque monkey. *Brain Struct. Funct.*, **224**, 925–935.

Pagani, M., Bertero, A., Liska, A., Galbusera, A., Sabbioni, M., Barsotti, N., Colenbier, N., Marinazzo, D., Scattoni, M.L., Pasqualetti, M., & Gozzi, A. (2019) Deletion of autism risk gene shank3 disrupts prefrontal connectivity. *J. Neurosci.*, **39**, 5299–5310.

Raichle, M.E., MacLeod, A.M., Snyder, A.Z., Powers, W.J., Gusnard, D.A., & Shulman, G.L. (2001) A default mode of brain function. *Proc. Natl. Acad. Sci.*, **98**, 676–682.

Rocchi, F., Canella, C., Noei, S., Gutierrez, D., Coletta, L., Galbusera, A., Vassanelli, S., Pasqualetti, M., Iurilli, G., Panzeri, S., & Gozzi, A. (2022) Cortical Silencing Results in Paradoxical fMRI Overconnectivity. *SSRN Electron. J.*, 1–45.

Rubinov, M. (2016) Constraints and spandrels of interareal connectomes. *Nat. Commun.*, **7**, 1–11.

Rubinov, M. & Bullmore, E. (2013) Fledgling pathoconnectomics of psychiatric disorders. *Trends Cogn. Sci.*, **17**, 641–647.

Rubinov, M. & Sporns, O. (2010) Complex network measures of brain connectivity: Uses and interpretations. *Neuroimage*, **52**, 1059–1069.

Rubinov, M., Ypma, R.J.F., Watson, C., & Bullmore, E.T. (2015) Wiring cost and topological participation of the mouse brain connectome. *Proc. Natl. Acad. Sci.*, **112**, 10032–10037.

Samu, D., Seth, A.K., & Nowotny, T. (2014) Influence of Wiring Cost on the Large-Scale Architecture of Human Cortical Connectivity. *PLOS Comput. Biol.*, **10**, e1003557.

Seguin, C., Razi, A., & Zalesky, A. (2019) Inferring neural signalling directionality from undirected structural connectomes. *Nat. Commun.*, **10**, 4289.

Seguin, C., Tian, Y., & Zalesky, A. (2020) Network communication models improve the behavioral and functional predictive utility of the human structural connectome. *Netw. Neurosci.*, **4**, 980–1006.

Sethi, S.S., Zerbi, V., Wenderoth, N., Fornito, A., & Fulcher, B.D. (2017) Structural connectome topology relates to regional BOLD signal dynamics in the mouse brain. *Chaos An Interdiscip. J. Nonlinear Sci.*, **27**, 47405.

Sforazzini, F., Schwarz, A.J., Galbusera, A., Bifone, A., & Gozzi, A. (2014) Distributed BOLD and CBV-weighted resting-state networks in the mouse brain. *Neuroimage*, **87**, 403–415.

Shen, K., Goulas, A., Grayson, D.S., Eusebio, J., Gati, J.S., Menon, R.S., McIntosh, A.R., & Everling, S. (2019) Exploring the limits of network topology estimation using diffusion-based tractography and tracer studies in the macaque cortex. *Neuroimage*, **191**, 81–92.

Smith, S.M., Fox, P.T., Miller, K.L., Glahn, D.C., Fox, P.M., Mackay, C.E., Filippini, N., Watkins, K.E., Toro, R., Laird, A.R., & Beckmann, C.F. (2009) Correspondence of the brain's functional architecture during activation and rest. *Proc. Natl. Acad. Sci.*, **106**, 13040–13045.

Sporns, O., Tononi, G., & Kötter, R. (2005) The human connectome: A structural description of the human brain. *PLoS Comput. Biol.*, **1**, 0245–0251.

Stafford, J.M., Jarrett, B.R., Miranda-Dominguez, O., Mills, B.D., Cain, N., Mihalas, S., Lahvis, G.P., Lattal, K.M., Mitchell, S.H., David, S. V., Fryer, J.D., Nigg, J.T., & Fair, D.A. (2014) Large-scale topology and the default mode network in the mouse connectome. *Proc. Natl. Acad. Sci.*, **111**, 18745–18750.

Suárez, L.E., Markello, R.D., Betzel, R.F., & Misic, B. (2020) Linking Structure and Function in Macroscale Brain Networks. *Trends Cogn. Sci.*, **24**, 302–315.

Towlson, E.K., Vértes, P.E., Ahnert, S.E., Schafer, W.R., & Bullmore, E.T. (2013) The rich club of the C. elegans neuronal connectome. *J. Neurosci.*, **33**, 6380–6387.

Tsai, P.-J., Keeley, R.J., Carmack, S.A., Vendruscolo, J.C.M., Lu, H., Gu, H., Vendruscolo, L.F., Koob, G.F., Lin, C.-P., Stein, E.A., & Yang, Y. (2020) Converging Structural and Functional Evidence for a Rat Salience Network. *Biol. Psychiatry*, **88**, 867–878.

van den Brink, R.L., Nieuwenhuis, S., & Donner, T.H. (2018) Amplification and suppression of distinct brainwide activity patterns by catecholamines. *J. Neurosci.*, **38**, 7476–7491.

Van den Brink, R.L., Pfeffer, T., Warren, C.M., Murphy, P.R., Tona, K.D., van der Wee, N.J.A., Giltay, E., Van Noorden, M.S., Rombouts, S.A.R.B., Donner, T.H., & Nieuwenhuis, S. (2016) Catecholaminergic neuromodulation shapes

intrinsic MRI functional connectivity in the human brain. *J. Neurosci.*, **36**, 7865–7876.

van den Heuvel, M.P., Bullmore, E.T., & Sporns, O. (2016) Comparative Connectomics. *Trends Cogn. Sci.*, **20**, 345–361.

van den Heuvel, M.P., de Lange, S.C., Zalesky, A., Seguin, C., Yeo, B.T.T., & Schmidt, R. (2017) Proportional thresholding in resting-state fMRI functional connectivity networks and consequences for patient-control connectome studies: Issues and recommendations. *Neuroimage*, **152**, 437–449.

van den Heuvel, M.P., Kahn, R.S., Goni, J., & Sporns, O. (2012) High-cost, high-capacity backbone for global brain communication. *Proc. Natl. Acad. Sci.*, **109**, 11372–11377.

van den Heuvel, M.P., Scholtens, L.H., & de Reus, M.A. (2016) Topological organization of connectivity strength in the rat connectome. *Brain Struct. Funct.*, **221**, 1719–1736.

van den Heuvel, M.P. & Sporns, O. (2013) Network hubs in the human brain. *Trends Cogn. Sci.*, **17**, 683–696.

van den Heuvel, M.P. & Sporns, O. (2019) A cross-disorder connectome landscape of brain dysconnectivity. *Nat. Rev. Neurosci.*, **20**, 435–446.

Van Essen, D.C., Ugurbil, K., Auerbach, E., Barch, D., Behrens, T.E.J., Bucholz, R., Chang, A., Chen, L., Corbetta, M., Curtiss, S.W., Della Penna, S., Feinberg, D., Glasser, M.F., Harel, N., Heath, A.C., Larson-Prior, L., Marcus, D., Michalareas, G., Moeller, S., Oostenveld, R., Petersen, S.E., Prior, F., Schlaggar, B.L., Smith, S.M., Snyder, A.Z., Xu, J., & Yacoub, E. (2012) The Human Connectome Project: A data acquisition perspective. *Neuroimage*, **62**, 2222–2231.

Vázquez-Rodríguez, B., Suárez, L.E., Markello, R.D., Shafiei, G., Paquola, C., Hagmann, P., Van Den Heuvel, M.P., Bernhardt, B.C., Spreng, R.N., & Misic, B. (2019) Gradients of structure–function tethering across neocortex. *Proc. Natl. Acad. Sci. U. S. A.*, **116**, 21219–21227.

Vertes, R.P. (2004) Differential Projections of the Infralimbic and Prelimbic Cortex in the Rat. *Synapse*, **51**, 32–58.

Vetere, G., Kenney, J.W., Tran, L.M., Xia, F., Steadman, P.E., Parkinson, J., Josselyn, S.A., & Frankland, P.W. (2017) Chemogenetic Interrogation of a Brain-wide Fear Memory Network in Mice. *Neuron*, **94**, 363-374.e4.

Vezoli, J., Vinck, M., Bosman, C.A., Bastos, A.M., Lewis, C.M., Kennedy, H., & Fries, P. (2021) Brain rhythms define distinct interaction networks with differential dependence on anatomy. *Neuron*, **109**, 3862–3878.

Vogt, B.A. & Paxinos, G. (2014) Cytoarchitecture of mouse and rat cingulate cortex with human homologies. *Brain Struct. Funct.*, **219**, 185–192.

Vos de Wael, R., Benkarim, O., Paquola, C., Lariviere, S., Royer, J., Tavakol, S., Xu, T., Hong, S.J., Langs, G., Valk, S., Misic, B., Milham, M., Margulies, D., Smallwood, J., & Bernhardt, B.C. (2020) BrainSpace: a toolbox for the analysis of macroscale gradients in neuroimaging and connectomics datasets. *Commun. Biol.*, **3**, 1–10.

Wang, P., Kong, R., Kong, X., Liégeois, R., Orban, C., Deco, G., van den Heuvel, M.P., & Thomas Yeo, B.T. (2019) Inversion of a large-scale circuit model reveals a cortical hierarchy in the dynamic resting human brain. *Sci. Adv.*, **5**, eaat7854.

Wang, Q., Ding, S.L., Li, Y., Royall, J., Feng, D., Lesnar, P., Graddis, N., Naeemi, M., Facer, B., Ho, A., Dolbeare, T., Blanchard, B., Dee, N., Wakeman, W., Hirokawa, K.E., Szafer, A., Sunkin, S.M., Oh, S.W., Bernard, A., Phillips, J.W., Hawrylycz, M., Koch, C., Zeng, H., Harris, J.A., & Ng, L. (2020) The Allen Mouse Brain Common Coordinate Framework: A 3D Reference Atlas. *Cell*, **181**, 936–953.

Wang, X. & Chen, G. (2003) Small-world, scale-free and beyond. *IEEE Circuit Syst.*, **3**, 6–20.

Wang, X., Lin, Q., Xia, M., & He, Y. (2018) Differentially categorized structural brain hubs are involved in different microstructural, functional, and cognitive characteristics and contribute to individual identification. *Hum. Brain Mapp.*, **39**, 1647–1663.

Wang, X.J. (2020) Macroscopic gradients of synaptic excitation and inhibition in the neocortex. *Nat. Rev. Neurosci.*, **21**, 169–178.

Weinshenker, D. (2018) Long Road to Ruin: Noradrenergic Dysfunction in Neurodegenerative Disease. *Trends Neurosci.*, **41**, 211–223.

Whitesell, J.D., Liska, A., Coletta, L., Hirokawa, K.E., Bohn, P., Williford, A., Groblewski, P.A., Graddis, N., Kuan, L., Knox, J.E., Ho, A., Wakeman, W., Nicovich, P.R., Nguyen, T.N., van Velthoven, C.T.J., Garren, E., Fong, O., Naeemi, M., Henry, A.M., Dee, N., Smith, K.A., Levi, B., Feng, D., Ng, L., Tasic, B., Zeng, H., Mihalas, S., Gozzi, A., & Harris, J.A. (2021) Regional, Layer, and Cell-Type-Specific Connectivity of the Mouse Default Mode Network. *Neuron*, **109**, 545–559.

Yang, X., Li, H., Ge, J., Chao, H., Li, G., Zhou, Z., & Liu, J. (2020) The level of GNE and its relationship with behavioral

phenotypes in children with autism spectrum disorder. *Medicine (Baltimore).*, **99**, e21013.

Yousefi, B., Shin, J., Schumacher, E.H., & Keilholz, S.D. (2018) Quasi-periodic patterns of intrinsic brain activity in individuals and their relationship to global signal. *Neuroimage*, **167**, 297–308.

Zingg, B., Hintiryan, H., Gou, L., Song, M.Y., Bay, M., Bienkowski, M.S., Foster, N.N., Yamashita, S., Bowman, I., Toga, A.W., & Dong, H.W. (2014) Neural networks of the mouse neocortex. *Cell*, **156**, 1096–1111.